POLITECNICO DI TORINO

Corso di Laurea Magistrale in Mechatronic Engineering

Cooling of a controller for an HVAC compressor

Relatori
Prof. Bonfitto Angelo
D.Sc.(Tech.) Fredrik Boxberg

Studente
Amedeo Isoardi
s333158

Anno Accademico 2024/2025

Contents

List of Figures

List of Tables

Abstract

The following paper will face the possible approaches used to cool down the power electronics for HVAC compressor applications. Incorporating evidence from papers, benchmarking and state of the art literature a trend in the industry will be outlined.
Once the fundamental bricks are placed, three different cooling approaches will be analized and compared both on the mechanical/thermal side and the electric one.
As outcome, the system performance, efficiency and size of the 3 different approaches will be provided.

1 Introduction

1.1 Definition and Working Principles of HVAC Systems

Heating, Ventilation, and Air Conditioning (HVAC) is a technology designed to ensure ambient comfort in indoor and automotive environments. HVAC systems help maintain a pleasant climate by regulating temperature levels either heating or cooling ambients in vehicles, homes and commercial/industrial settings. Practical residential air conditioning units began to emerge in the 1930s, but they were still expensive and considered luxury items. While in automotive the first systems were installed during the early 1960s. In both cases, right now they are a standard feature in nearly all modern vehicles and buildings.

The operation of an HVAC unit is based on the principles of **conduction and convection**. In the case of Air conditioning, the heat is transferred from a cooler region (the ambient to be conditioned) to a warmer one thanks to pressure differences, a process known as **refrigeration**. The general scheme of the system is displayed in the following picture. (the following discussion is sourced from [1].

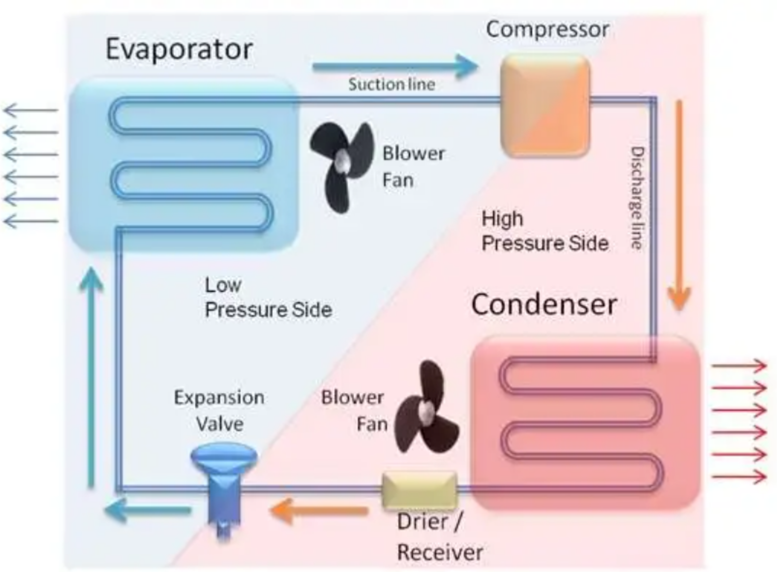

Figure 1.1: Refrigeration cycle diagram [1].

The main components are:

- **Evaporator:** Functions as a heat exchanger in the refrigeration cycle. The low-pressure, low-temperature liquid refrigerant enters the evaporator from the expansion valve. As it flows through the evaporator coils, it absorbs heat from the air blown across the coils, causing the refrigerant to evaporate into a low-pressure vapour.
  The evaporator performs two main tasks:
  - Absorbing heat.
  - Converting refrigerant to vapour.
- **Compressor:** often referred to as the heart of the HVAC system, the compressor draws in vapour refrigerant from the suction line and compresses it into a high-temperature,

high pressure vapour, typically 2.5 times hotter than the outside air.
Key functions of the compressor include:

  - Superheating the refrigerant.
  - Removing latent heat (condensation).
  - Driving refrigerant circulation.

  This temperature difference allows heat to flow out of the system.

- **Condenser:** the high-pressure vapour enters the condenser, another heat exchanger. Flowing from top to bottom, the refrigerant releases heat to the outside air. As it cools, it condenses into a liquid, a process called subcooling. The condenser's external surface becomes hot, and a fan or blower helps expel this heat. For optimal efficiency, the condenser should have maximum exposure to airflow.
- **Receiver/Drier:** located in the high-pressure section, typically between the condenser and expansion valve—the receiver/drier serves three main purposes:
  - Stores excess refrigerant during low cooling demand (receiver function).
  - Filters out contaminants.
  - Absorb moisture introduced during manufacturing or servicing (drier function).
- **Expansion Device:** The expansion device creates the necessary pressure drop for the refrigerant to evaporate. By restricting refrigerant flow, it causes a low-pressure zone on one side of the system known as the suction side or low side.

As a consequence the components can be divided into two pressure zones:

- The high-pressure side includes the condenser and receiver/drier.
- The low-pressure side includes the evaporator. The compressor and expansion valve serve as the transition points between these zones.

A climate control systems maintain the environment temperature and humidity without manual input. Once the desired conditions are set, the system uses sensors to monitor the actual cabin environment.
These sensors feed data to a microcontroller (MCU), which compares it to the user settings and adjusts heating or cooling accordingly. This automation eliminates the need for manual adjustments.

To fully manage the working principle of refrigeration cycle, the argument must be tackled deeper on the thermodynamic point of view. To do so the logarithmic p (pressure) - h (specific enthalpy J/Kg) diagram is introduced. It shows the aggregate state of a substance, depending on pressure and heat. "For refrigeration, the diagram is reduced to the relevant regions of liquid, gaseous and their mixed form" [2].

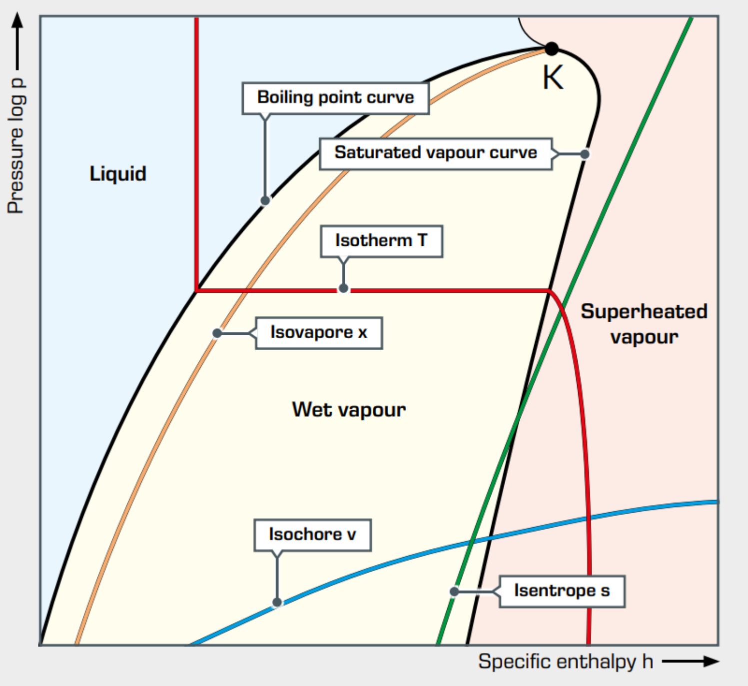

Figure 1.2: Log p-h diagram, general structure [2].

"The vertical axis shows the logarithmic pressure and the horizontal axis shows the specific enthalpy with linear scaling. Accordingly, the isobars are horizontal and the isenthalps are vertical. The logarithmic scaling makes it possible to represent processes with large pressure differences. The saturated vapour curve and the boiling point curve meet at the critical point K" [2].

Every step of the refrigeration cycle can be represented directly on the graph. To a first schematic representation will follow a commented detailed representation.

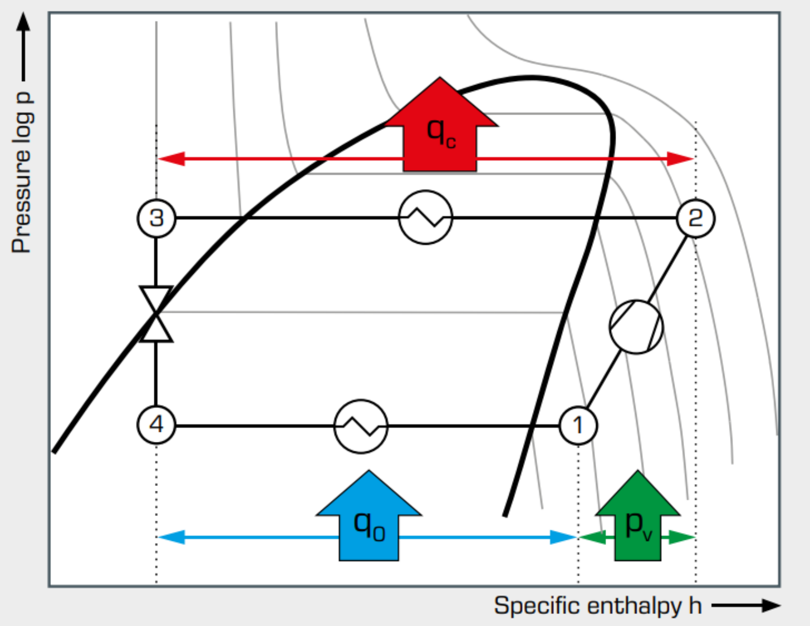

Figure 1.3: Refrigeration cycle, schematic representation on log p-h diagram [2].

Given the mass flow rate of the refrigerant $\dot{m}$, the thermal outputs can be calculated using the specific enthalpies at key state points in the cycle:

- **Refrigeration capacity (Cooling Effect):**

$$Q_0 = \dot{m} \cdot q_0 = \dot{m} \cdot (h_1 - h_4)$$

- **Compressor work (Technical Work Input):**

$$W = \dot{m} \cdot p_v = \dot{m} \cdot (h_2 - h_1)$$

- **Condenser capacity (Heat Rejection):**

$$Q_c = \dot{m} \cdot q_c = \dot{m} \cdot (h_2 - h_3)$$

The COP (coefficient of performance) for a refrigeration cycle is defined as:

$$\mathrm{COP}_{\mathrm{refrigeration}} = \frac{Q_0}{W}$$

A more detailed representation of the cycle is displayed in Figure 1.4.

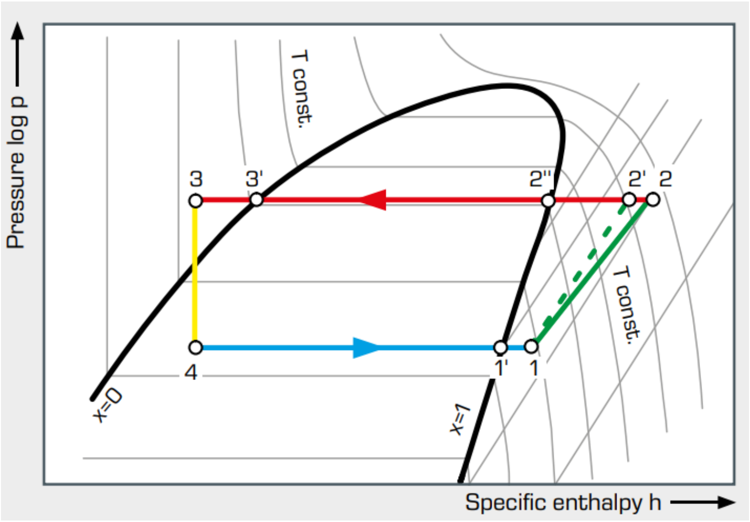

Figure 1.4: Refrigeration cycle, detailed representation on log p-h diagram [2].

- **1 – 2:** Polytropic compression (for comparison: 1 – 2’ isentropic compression).
- **2 – 2”:** Isobaric cooling (deheating) of the superheated vapour.
- **2” – 3’:** Isobaric condensation.
- **3’ – 3:** Isobaric cooling (subcooling) of the liquid.
- **3 – 4:** Isenthalpic expansion to the evaporation pressure.
- **4 – 1’:** Isobaric evaporation.
- **1’ – 1:** Isobaric heating (superheating) of the vapour.

REMARK: For the scope of the thesis, the understanding of the refrigeration cycle could seem marginal. However the cooling choice of the inverter can have great impact on the cycle COP and interesting considerations can be done.

1.2 Inverters

Inverters are used for converting DC voltage into a modulated AC voltage, both in terms of frequency and magnitude. Normally inverters are used to control either speed or torque of AC motors.
Their construction typically makes use of power transistors (MOSFETs) and diodes. These are operated as electronic switches [3]. In the following image a general schematics of an inverter is reported.

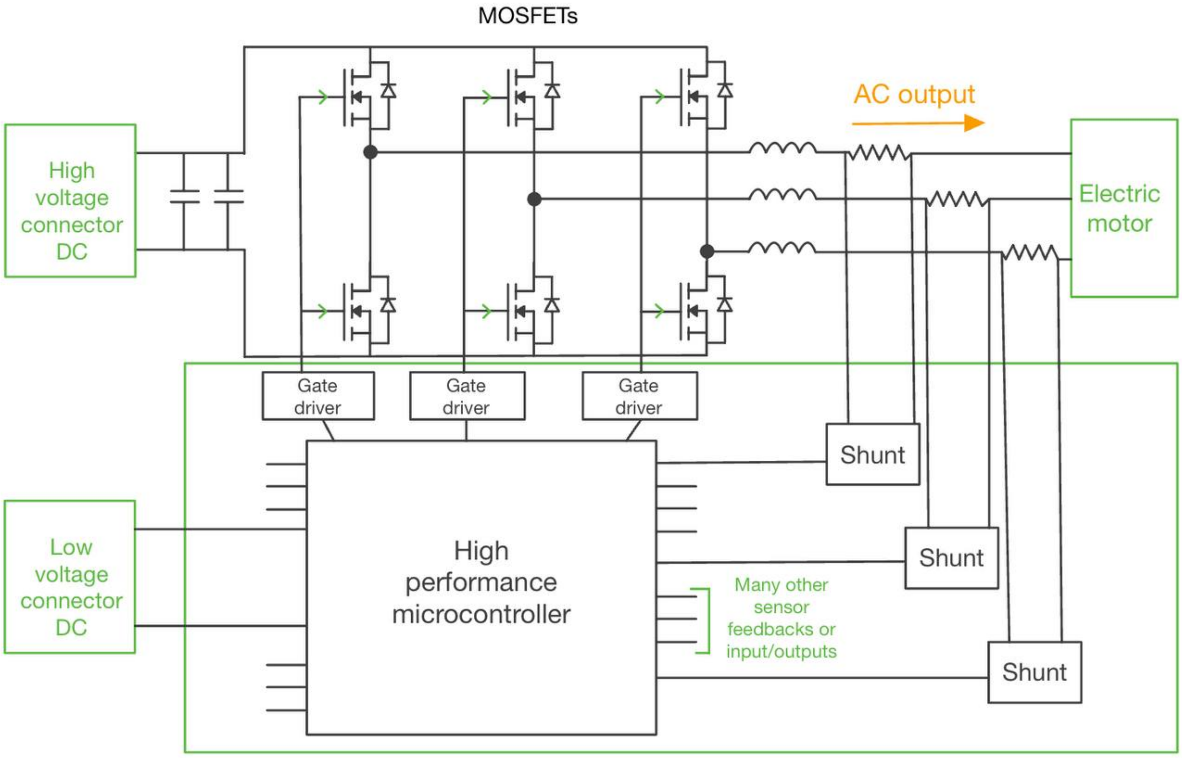

Figure 1.5: Inverter circuit diagram.

Two different parts can be distinguished. The upper part of the inverter is connected to a high voltage DC input that, through the controlled switching MOSFET cascade structure, is converted into AC signal. While the lower part is made up mainly by the microcontroller that, powered by a low DC voltage, controls the upper MOSFETs based sensors and input data.

All the above considerations can be summarized in the concept of PWM (Pulse width modulation). PWM is the heart of the inverter technology and allows to modulate the output frequency and voltage leveraging the transistor technology.

TAKE AWAY CONCEPT: The inverter working principle gives rise to switching losses which, especially for high values of the switching frequency, cause a reduction in their energy conversion efficiency. The energy lost through dissipation manifests as localized heating. For safety reasons, a dissipation system that keeps the MOSFETs T_j (junction temperature) under control must be implemented.

1.3 VFDs

The VFD technology serves the same purpose of generating a modulated AC output for motor control; however, in this case, the input is a high-voltage AC supply. This type of system is typically employed in environments where only AC power is available, common case in industrial and high-power applications.
Because of the high power application and lower output frequencies, in VFDs the MOSFTEs are substituted by IGBTs (Insulated-Gate Bipolar Transistors).

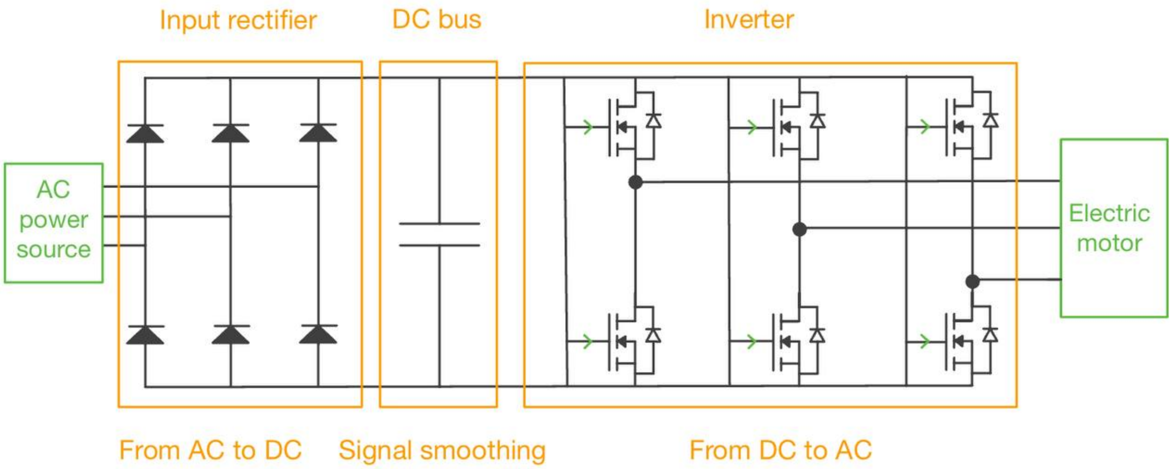

Figure 1.6: VFD circuit diagram.

The working principle is the same of that of the inverter alone, however two additional components for input signal conditioning must be added: an input rectifier and a DC bus. The purpose is rectifying the input AC voltage into a DC voltage in order to be modulated by the inverter.

Specifically the diode input rectifier is the first stage of the VFD and is responsible for converting the incoming AC supply into DC voltage. It typically consists of a six-diode bridge, where each pair of diodes conducts during alternate half-cycles of the input waveform. This kind of rectifier is the simplest type of front-end stage used in a VFD.
While the DC bus, often made up of one or more capacitors (condensers), serves as an energy storage and filtering stage between the rectifier and the inverter. After the AC input is rectified into DC, the DC bus smooths out voltage ripples and maintains a stable DC voltage for the inverter.

As for inverter case, in VFD MOSFETs switching and input signal conditioning create losses that translate into heat to be dissipated and kept under control.

1.4 Thermal management, impact on electronic devices

The cooling or thermal management faces critical challenges with the continuous miniaturization and rapid increase of heat flux of electronic devices. "With the evolution of power semiconductor devices, high operating temperatures and large thermal cycles have become possible, necessitating a significant improvement in thermal system designs" [4].

"Researchers have made significant efforts to develop effective thermal management systems to improve the reliability and lifespan of power electronic converters" [4].

As they provide controllability and flexibility, power electronics is widely used throughout many crucial domains: transportation sector, aerospace industries, and energy sectors. As a consequence the industry must satisfy the following requirements:

- Systems work reliability, looking for an improvement of the mean time between failures (MTBF) lowering e-waste and CO2 emissions.
- A decrease in the overall power consumption, allowing the electronic components to work at well defined project temperatures.
- Minimization of weight and size in the resulting system.

PECs [1] include multiple components. However, power semiconductor devices (PSD) such as IGBTs and MOSFETs constitute the main source of heat and have been identified as having the highest possibility of breakdown (according to a survey conducted in [5]).
The motivations related to the previous statement are multiple, in the following lines the most relevant in terms of safety, heat dissipation and product development will be taken into account.

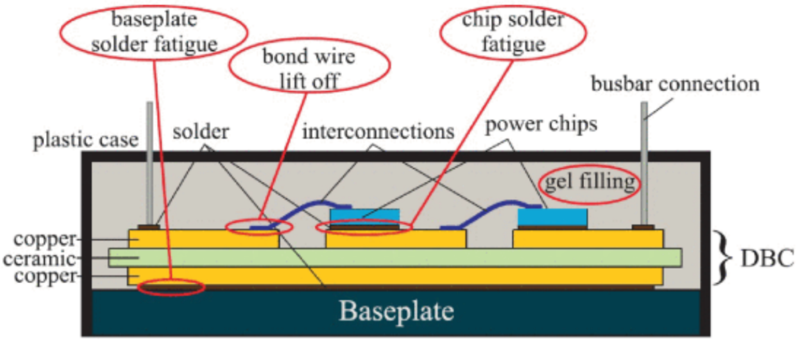

Figure 1.7: Structure of power semiconductor device [4]

First a brief explanation of the structure of power semiconductor device depicted in Figure 1.7 . In light blue are visible the power chips, in blue the connections between them, under them is visible the DCB (Direct Bonded Copper) that works as insulating layer and finally the Baseplate that encloses all this components.
Looking at Figure 1.7, the upcoming considerations can be done.

Generally alluminum bond wires are used for electrical connections between chips and terminals. In particular during operation:

- PSDs are subjected to stress due to alterations in temperature and power. Periodic temperature fluctuations within the PSDs (thermal cycling) induce fatigue phenomenon on the device.

---

[1] PECs = "Power electronic converters"

- The differences in thermal expansion coefficients (CTE) between different material layers (normally copper and ceramic) lead to mechanical stress when temperature changes occur. This effect is more prominent for aluminium bond wire and solder between substrate and baseplate.

Thus, thermal cycles lead to severe fatigue in bond wire and solder joints causing of device ageing and breakdown. The impact of average temperature and thermal cycling on the reliability of PSDs is depicted in Figure 1.8.

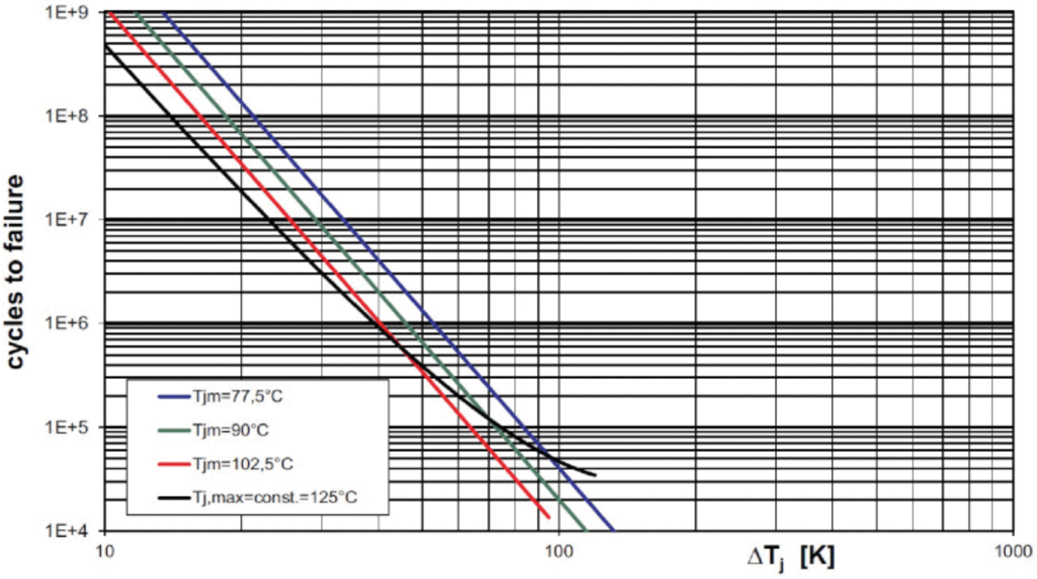

Figure 1.8: Standard IGBT modules Power cycling lifetime as a function of ΔTj and T_j (respectively the variation in junction and average junction temperature [4])

"Moreover, according to US Air Force Avionics Integrity Program research, high temperature is responsible for over 50 % of electronic equipment failures" [4]. The causes of failures identified in this study are presented in Figure 1.9.

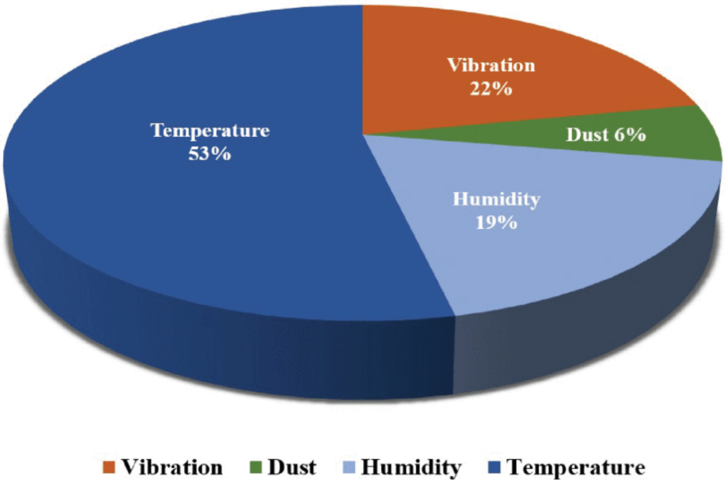

Figure 1.9: Causes of electronic equipment failures [4])

1.5 Chapter Take Away and Key Insights

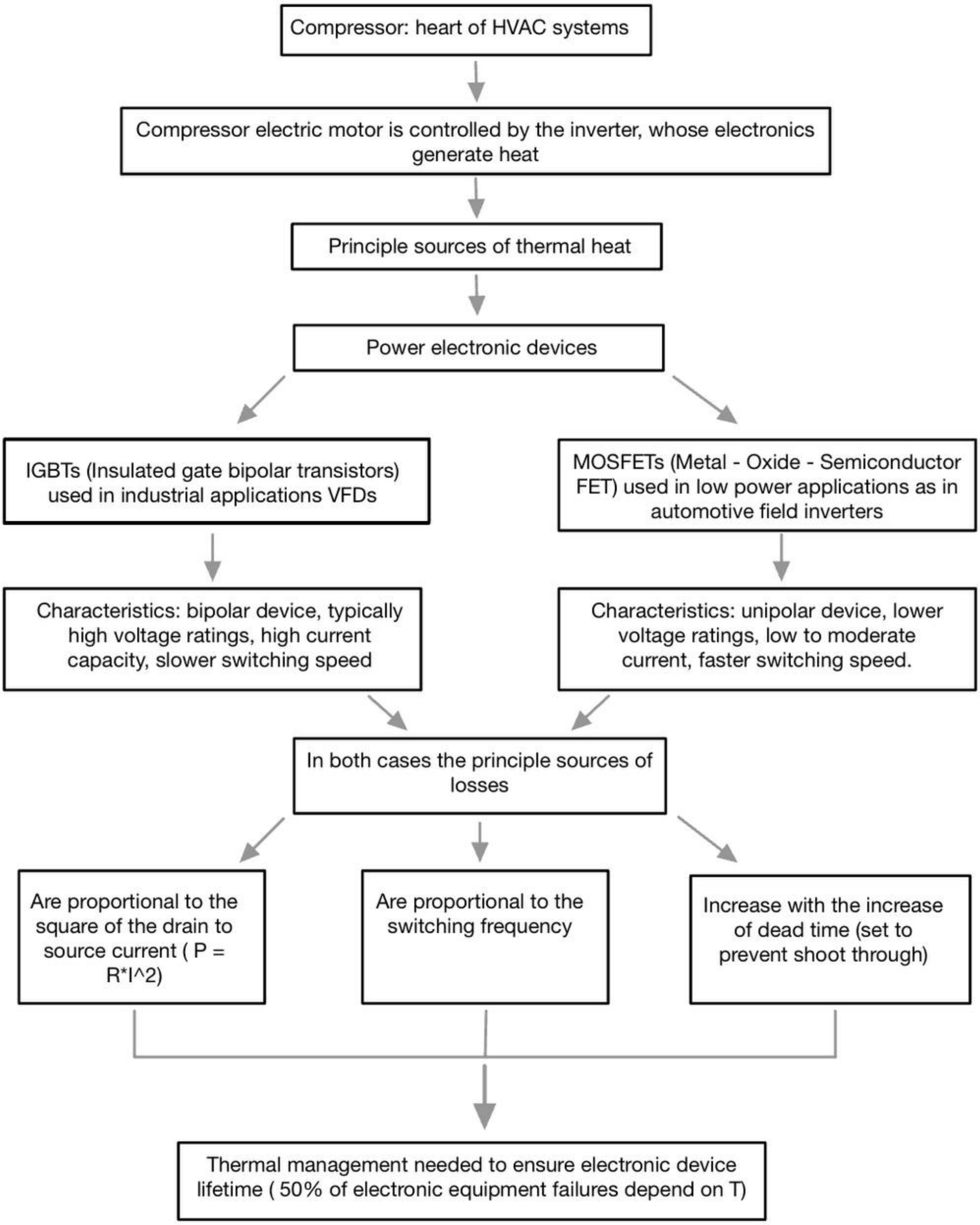

Figure 1.10: Key concept take away tree

2 Heat Transfer Enhancement Devices

2.1 Heat Sinks

"A heat sink is a thermal management component typically used in electronic devices to dissipate heat and prevent overheating. Usually it is made of a metal such as aluminum or copper"[6]. It absorbs and transfers heat from the heat-generating components (such as CPUs or inverter/VFD Mosfets) to the surrounding medium (typically air, forced or not).

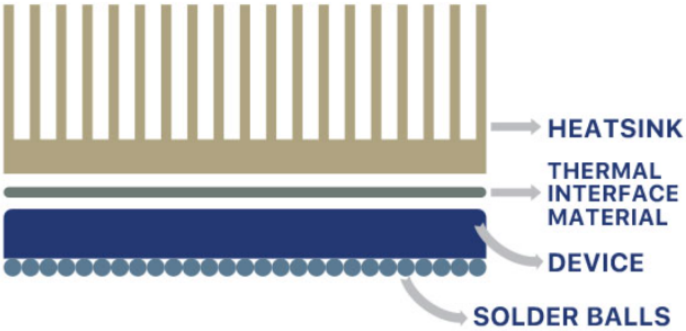

Figure 2.1: General implementation scheme [6].

The key goal of heat sinks is increasing the surface area available for heat transfer. Moreover using fins or other structures, the flow of the medium on the heat sink can be influenced, increasing both the surface area and the convective coefficient. This helps to keep the device operating at a safe temperature and prevent damage from overheating.

The primary mechanism of heat transfer from the heatsink is convection, although radiation also has a minor influence.
There are two distinct types of convection:

- Natural convection: where due to transfer of heat from the surface of the solid to the fluid particles in close proximity, the movement of the fluid particles is caused by the local changes in density.
- Forced convection: where the movement of the fluid particles is forced using a fan or blower.

2.1.1 Working Principle

"A heat sink works by spreading the generated heat over a larger surface area, allowing it to dissipate more efficiently. The heat sink is typically attached to the electronic component using a thermal interface material, such as a thermal paste or pad. This material helps to transfer the heat from the component to the heat sink"[6].
Once the heat is transferred, it dissipates into the surrounding air through convection.
The larger the surface area of the heat sink, the more efficient it is at dissipating heat.

The performance of heat sinks are a consequence of many parameters including:

- Geometry: many designs are available, but they typically comprise a base and a number of protrusions attached to this base. The base is the feature that interfaces with the device to be cooled. Heat is conducted through the base into the protrusions. The protrusions can take several forms.
- Material
- Surface treatment
- Air velocity
- Thermal Interface material (TIM)

The last item is very important. At a microscopic level electronic components surfaces are rough. This results in very few points of contact and many tiny air gaps between the component and its heat sink.

Figure 2.2: Thermal interface role [6].

Because of the air having a low thermal conductivity, it results in a poor conduction of heat from the device to the heatsink. To tackle this problem, a thermal interface material (TIM) can be applied to the base of the heatsink. Basically by doing this the air gaps are filled providing a lower thermal resistance conduction path between device and heat sink.

Thermal interface avoid keeping the heat on the device allowing better control on the junction temperature.

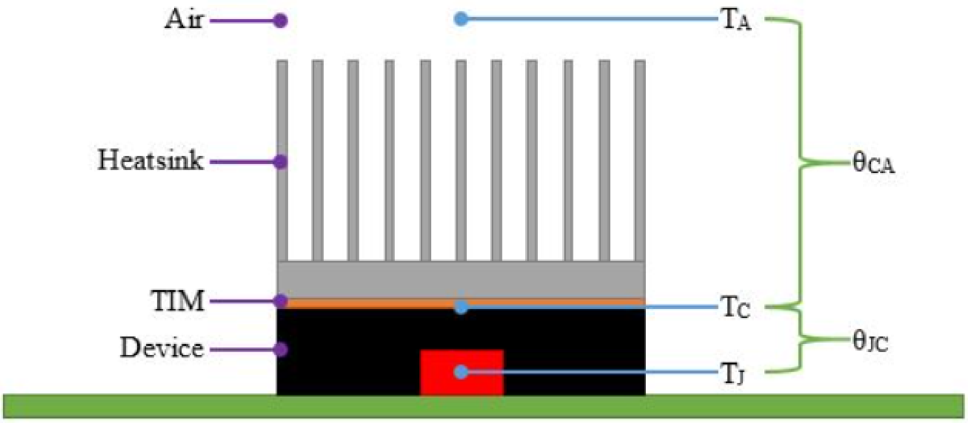

Figure 2.3: Temperatures gaps scheme [6].

The junction temperature (TJ) is the temperature of the hottest part of the device. This is the critical temperature to control for correct operation and normally, when talking about MOSFETs, "it should be kept away from the limit value of 150°C for safety reasons" [7]. Other temperatures of interest are the temperature of the case (T_C in Figure 2.3) and the temperature of the ambient (T_A in Figure 2.3), fundamental to the heat transfer from the heat sink to the air flow.
The higher the T_A, the lower the gap of temperatures between heat sink and the air flow, the lower the amount of heat transferred through convection in the same amount of time.

2.1.2 Commonly used TIMs

A suitable thermal interface material should have the following properties [8]:

- High flexibility
- Good insulation
- High compressibility
- Good heat conduction

For heat sinks applications TIMs normally come into the form of either thermal pads or thermal grease. Both solutions report some interesting features and drawbacks. In this sections the two technologies are briefly analysed.

Thermal pads are solid, compressible sheets made from thermally conductive materials. They normally display a rubbery state and comes in the form of silicon or ceramic filled polymers.

Figure 2.4: Thermal pad example [8].

Thermal pads are typically used in situations where applying thermal grease is not feasible, such as in presence of uneven components. Spreading thermal grease can be challenging, making thermal pads the ideal solution [9]. In the following Table, drawbacks and benefits of pads are briefly discussed.

Thermal Pads TIMs	
Advantages	**Drawbacks**
Easy to cut to the desired size.	Delamination is a possibility.
Various thicknesses available.	Thermal conductivity is lower than thermal grease.
Harsh environments do not affect them.	Less effective at filling surface irregularities.

Table 2.1: Thermal pads, benefits and drawbacks comparison [8].

A brief analysis is now devoted to thermal grease, another commonly used thermal interface material. The following section discusses their characteristics, advantages, and limitations in comparison to thermal pads.

Thermal grease "It is a soft, room-temperature substance used to transfer heat from electronics to a heatsink more efficiently. These products are non-curing and should be applied in thin, even layers to optimize thermal transfer" [8].
Because thermal grease tends to flow easily, it's important to apply it carefully to prevent excess material or contamination of nearby components. However it's flow stands also as its best characteristic, allowing grease to perfectly fill all the air gaps due to surface roughness.

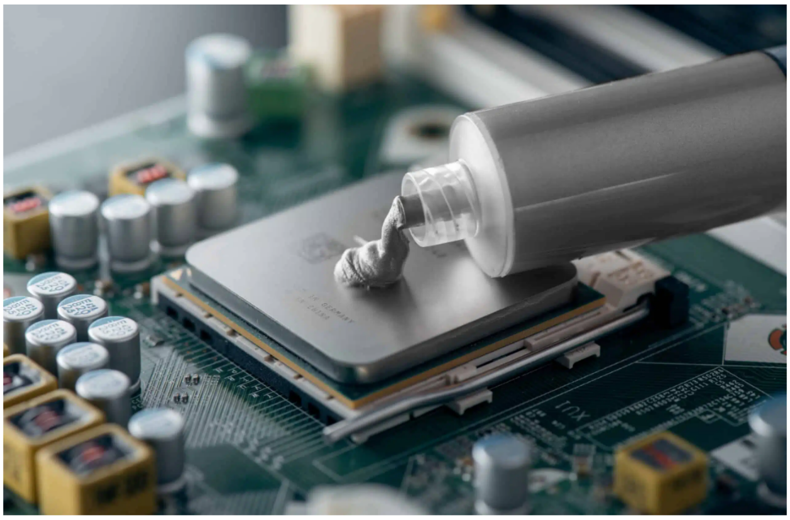

Figure 2.5: Example of thermal grease application process [10].

Different types of thermal grease are available on the market, they can be:

- Ceramic-based
- Metal-based
- Liquid-based

"In general, thermal grease is not electrically conductive, but some types are designed to be so" [8]. Normally this parameter is taken into account when dielectric properties become important and circuit insulation is fundamental.
As in previous case, advantage and disadvantages of this technology are analysed.

Thermal grease TIM	
Advantages	**Drawbacks**
Curing is not necessary	Thickness is difficult to control.
Perfect surface irregularities filling.	The material can dry out over time.
Delamination does not occur.	It can be messy to apply.

Table 2.2: Thermal grease, benefits and drawbacks comparison [8].

Overall, thermal grease provides excellent thermal contact and adaptability, making it well suited for applications requiring high heat transfer efficiency. However, its handling complexity and potential for drying or contamination limit its use in environments demanding long-term stability or clean processing. Therefore, the selection between thermal grease and alternative TIMs should be guided by specific operational requirements, maintenance expectations, and the desired balance between performance and practicality.

2.1.3 Common geometries and materials

Heat sinks come in various shapes and are crafted in a various range of materials. Both parameters are fundamental for thermal performances. However, in selecting the perfect trade-off which provides the best thermal performance, cost factor and manufacturability must be taken into account.

An interesting comparative analysis of heat sink performance using different materials and geometries has been conducted by American Journal of Engineering Research (AJER) in 2022 ([11]). In this section a summary review of this paper is reported.
"CFD software named COMSOL was used to determine heat sink design giving the optimal thermal performance and cost. Four different fin geometries, including rectangular, hexagonal, square, and airfoil, and 13 different materials were used" [11].

(a) Square pin shape (b) Airfoil

Figure 2.7: Comparative geometries used.

Main input parameters on which the analysis is based:

- Temperature of the environment and CPU are respectively 25°C and 80°C.
- The fan forces the air at an average speed of 7.5 m/s.
- Cooling power and pressure loss are selected as performance indicators.

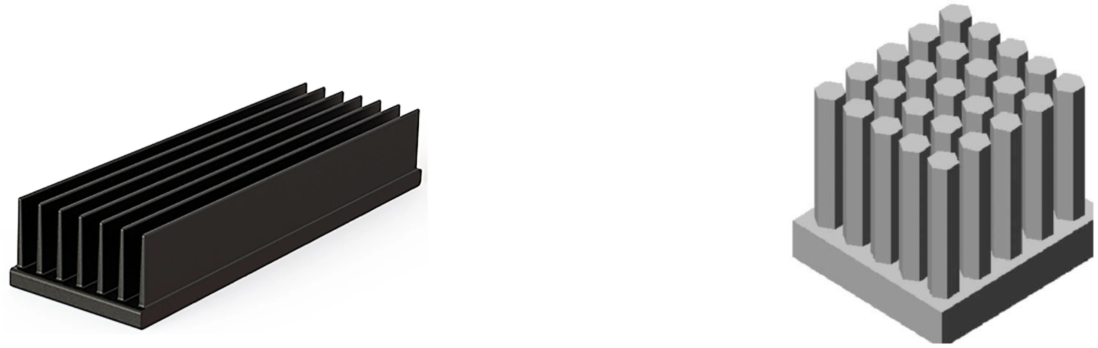

(a) Rectangular shape (b) Hexagonal pin shape

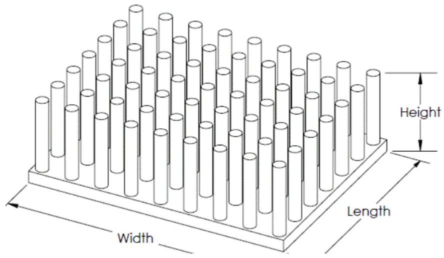

(c) Circular shape

Figure 2.6: Comparative geometries used

<u>REMARK</u>: In order to make a fair comparison between the different geometries, the fin number of each case is determined in such a way that the total volume of the selected fins remains the same.

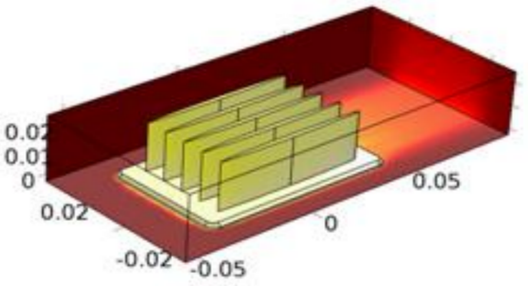

Figure 2.8: Simulation envirronement setup

Once a simulation environment was set as in Figure 2.8 (one for each geometry), with the flow directed from the left to the right, the following results were obtained (Tab 2.3).

Fin Geometry	**Cooling Power (W)**	**Average Pressure Loss (Pa)**
Pin Square	42.16	46.91
Rectangular	39.514	26.152
Airfoil	37.27	18.52
Pin Hexagonal	34.93	40.05
Pin Circular	31.01	35.42

Table 2.3: Cooling power (W) and average pressure loss (Pa) calculations for selected fin geometries.

According to results in Table 2.3, the maximum cooling power is obtained for pin square fin geometry with 42.16 W. However, for this configuration, the average pressure loss is extremely high.
The Airfoil configuration is proposed as the best trade-off. Indeed in terms of cooling power we have a slight decrease of just 11.6% compared to the squared pin, while the benefit on the pressure loss side is great (about 60.5 % reduction). The rectangular configuration could also be a solution, but in terms of pressure loss is still 29.2 % higher compared to the Airfoil one. Higher pressure drop would mean higher cooling fan powers and additional work required.

The next step is a comparison based on different manufacturing materials. Even though copper and aluminium are the most widely spread, it's interesting seeing how the material affects the overall performances. "13 different materials, including ten raw materials, and three aluminum alloys, were used. During the analysis, the fin number of each case is determined in such a way that the total volume of the selected fins remains the same" [11] (for a fair cost factor comparison). Airfoil is the geometry chosen for the analysis.

Table 2.4: Comparative analysis for various materials in terms of cost and performance using airfoil fin arrangement.

Material	Dissipated Power (W)	Pressure Loss (Pa)	Price (USA Dollar)
Silver	37.33	18.52	8.8593
Copper	37.27	18.52	6.46875
Gold	37.03	18.52	1396.875
Aluminum	36.68	18.52	2.3×10^3
7075 Alloy	36.44	18.52	0.021
Beryllium	36.34	18.52	0.564
356 Alloy	36.32	18.52	5.48×10^{-3}
Tungsten	36.15	18.51	1.782
6061 Alloy	36.02	18.51	0.0146
Magnesium	35.98	18.51	3.3711
Nickel	34.60	18.51	15.418
Lithium	34.46	18.51	0.166
Titanium	28.67	18.53	0.28

Thanks to the results in Table 2.4, it can be seen that the pressure loss values are approximately equal (the surface roughness obtained are comparable). While in terms of dissipated heat the best value is obtained for silver. The higher the thermal conductivity value, the better the heat flows through the component and spreads out. However, as the cost factor is taken into account, aluminium and 356 Alloys are preferable to others.

2.1.4 Advanced Designs: Splayed Pin-Fin Heat Sinks

At lower speeds, when air flow is natural or barely forced, the flux can have a hard time properly penetrating the heat sink. This can result in a lower convective heat transfer and reduced cooling capability. To tackle this problem a small modification can be applied to the standard heat sink geometry.
"Unlike standard pin fin heat sinks, which contain an array of vertically oriented pins, splayed pin fins features pins that gradually bend outward. Curving the pins in this way increases the spacing between the pins and allows surrounding air streams to enter and exit the pin array more efficiently without sacrificing surface area" [12].

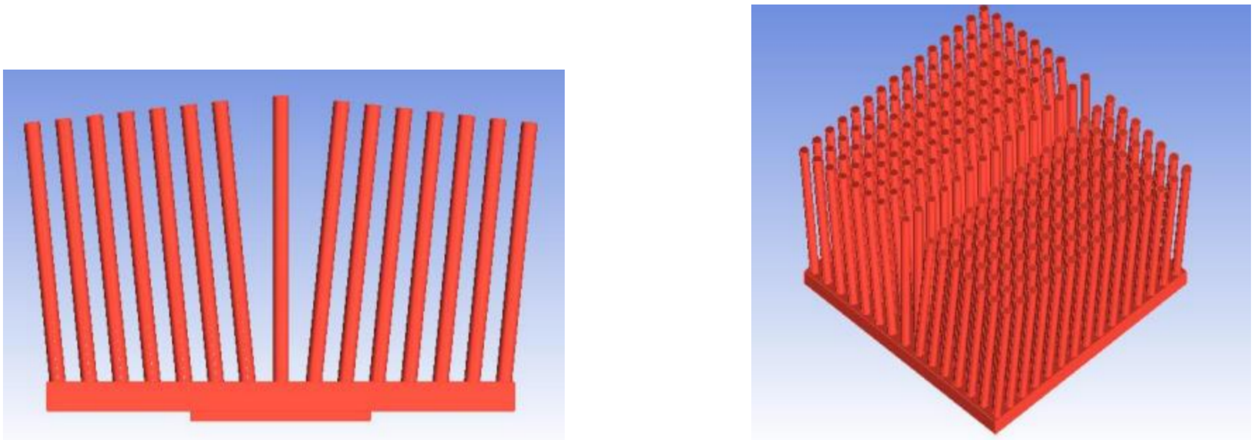

Figure 2.9: Splayed pin fin geometry [12].

As visible in Figure 2.9, adopting an inclined geometry of fins we obtain an increased pin spacing. Thanks to it, less power is needed to penetrate the array of pins and this results on a magnified heat transfer coefficient at lower air speeds.

In order to prove the point, modelling and consequent fluid analysis were carried out using ANSYS 12 software. The constraints adopted were the following: fin adiabatic tip, airflow normal to the fins, steady and laminar 2D flow, negligible radiation heat transfer, homogeneous fin material, constant heat flux through time.
Different slopes of the Pin Fin were analysed, the most important one are visible at Table 2.5. They are useful to set a trend in the performances.

<u>REMARK</u>: The data reported refer to the average temperature of the central line tips in the geometry and the material selected for the heat sink is standard Aluminium.

Cases	**Angle (degrees)**	**Aluminium (K)**
1	Standard	342
2	Splayed 4 degrees	340
3	Splayed 5 degrees	338
4	Splayed 6 degrees	337
5	Splayed 7 degrees	339

Table 2.5: Table of adopted slopes.

As can be easily inferred from the reported data that a benefit on increased heat transfer performances is seen until 6 degrees in slope, then the trend interrupts. To make it clearer a graphical solution is reported down below.

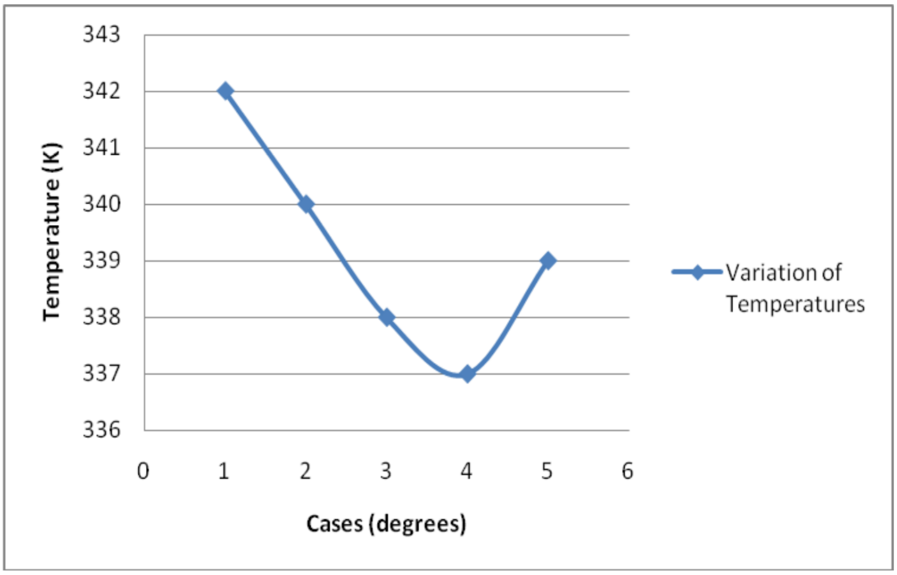

Figure 2.10: T vs case (pin inclination) results graph.

Finally, a further improvement was analysed. Because of its thermal conductivity, the Aluminum, compared to copper, has a reduced capability to spread the heat coming from the baseplate.

Thermal conductivity of solid aluminium	237 W/(m·K)
Thermal conductivity of solid copper	401 W/(m·K)

Table 2.6: Aluminium and copper thermal conductivity.

However copper has two main drawbacks: the cost and the increased weight compared to Aluminium. For this reason an Hybrid solution is proposed, a copper baseplate with

Aluminium pins re-flowed into it. It showed better heat spreading performances resulting in a reduced average temperature of the central line tips in the geometry.

Case	**Aluminium (K)**	**Copper (K)**	**Hybrid (K)**
6 Degrees splayed	336	326	322

Table 2.7: Hybrid solution vs Aluminium heat sink tip temperature.

2.2 Cold plates

Differently from heat sinks, the term "cold plate" is used to indicate a thermally sealed channel with pressurized fluid running through it. The fluid running from the channel is responsible for taking the generated heat away.

"When cooling high power devices (such as IGBT modules and high-powered semiconductors), air cooling is often inadequate and liquid cooling is required. Cold plates are a way to implement localized cooling of power electronics by transferring heat from the device to a liquid that flows to a remote heat exchanger and dissipates into either the ambient or to another liquid in a secondary cooling system [13]".

Figure 2.11: Cold plate, basic geometry [13]

In Figure 2.11 a basic cold plate geometry made up by a copper wavy coil inside a an aluminium base is reported.

Actually all the heat sinks geometries shown in the previous section can be leveraged in the cold plate case too. The different terminology between the two technologies is kept mainly to highlight the differences in architecture and fluid used.
Indeed geometries such as circular/elliptical pins and fins are used in cold plate with same exact goal in air cooling applications: increasing heat transfer coefficients and total heat transfer area to enhance convective heat transfer.
In the following Table, cold plate and heat sink technologies are compared based on thermal performance, noise, complexity and cost.

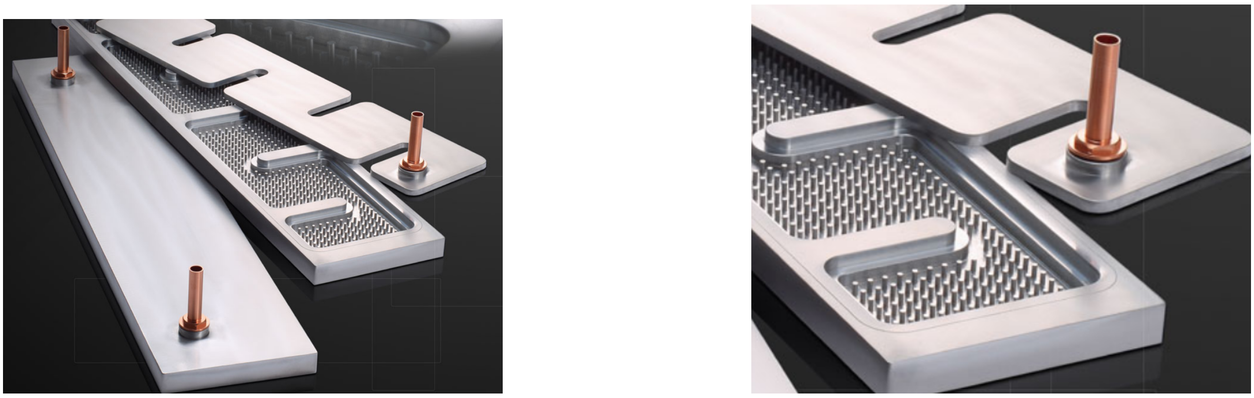

(a) Cold plate with circular pins (b) Zoom on Figure 2.12a

Figure 2.12: Example of cold plate design

Aspect	Cold Plate Cooling	Air Cooling (Heat Sink)
Thermal Performance	Superior thermal performance; suitable for dense, high-power configurations	Suitable for low power density applications; limited by ambient air and airflow capacity
Noise and Reliability	Quiet operation (no fans); reliable if properly maintained	Can be noisy due to fans; fan failure can cause overheating under heavy load
Cost and Complexity	More expensive and complex; requires pumps, reservoirs, and precise installation	Low cost and simple to install; less effective for high thermal demands

Table 2.8: Comparison between Cold Plate Cooling and Air Cooling

2.3 Chapter Take Away and Key Insights

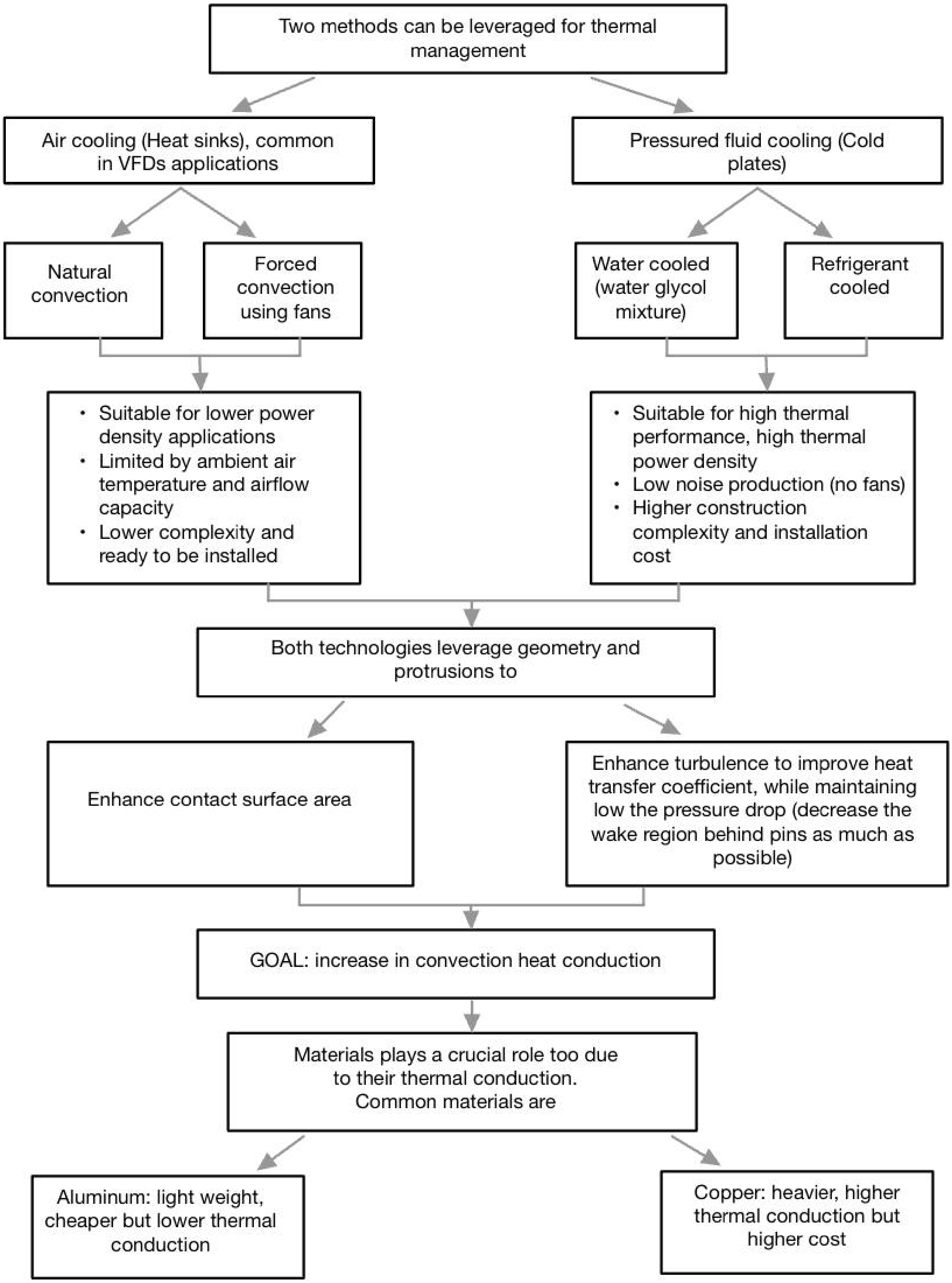

Two methods can be leveraged for thermal management

Air cooling (Heat sinks), common in VFDs applications

Pressured fluid cooling (Cold plates)

Natural convection

Forced convection using fans

Water cooled (water glycol mixture)

Refrigerant cooled

- Suitable for lower power density applications
- Limited by ambient air temperature and airflow capacity
- Lower complexity and ready to be installed

- Suitable for high thermal performance, high thermal power density
- Low noise production (no fans)
- Higher construction complexity and installation cost

Both technologies leverage geometry and protrusions to

Enhance contact surface area

Enhance turbulence to improve heat transfer coefficient, while maintaining low the pressure drop (decrease the wake region behind pins as much as possible)

GOAL: increase in convection heat conduction

Materials plays a crucial role too due to their thermal conduction. Common materials are

Aluminum: light weight, cheaper but lower thermal conduction

Copper: heavier, higher thermal conduction but higher cost

Figure 2.13: Key concept take away tree

Additionally to the above summary, some data must be highlighted.

Description	**Data reference**
Cooling power (W) and average pressure loss (Pa) calculations for selected fin geometries.	Table 2.3
Comparative analysis for various materials in terms of cost and performance using airfoil fin arrangement.	Table 2.4

Table 2.9: Useful data

Table 2.9 reports useful concepts in terms of magnitudes for heatsink/cold plate design. This methodology for identifying and analysing the relevant parameters is applied in greater depth in the next chapter, which focuses on benchmarking VFDs and inverters.

3 VFD and Inverters Benchmarking

Variable Frequency Drives and Inverters have become a cornerstone of modern industrial automation and motor control systems. By modulating the frequency and voltage supplied to the electric motor, VFDs enable precise control over motor speed, torque and energy consumption. As the demand for energy-efficient and high-performance motor control solutions grows, the diversity and complexity of the available VFD models have also increased. This leads to a growing interest in benchmarking, a systematic evaluation and comparison between different available solutions.
Benchmarking serves multiple purposes, the one of main interest are now reported:

- For end-user it offers an objective basis for comparison, a path-line to have a general overview on the product.
- Diving into the technical data, it is possible to infer what is the current status of the technology, what are the development approaches used and range values (Nominal powers, currents, voltages, cooling liquid type and temperature etc..) .
- Outlining the current status and performances values, it is possible to rough out future trends and leverage weak points to develop a better product.

The scope of this study includes three-phase VFDs commonly used in industrial applications and both AC (air conditioning) compressors and traction inverters.

3.1 VFDs

Starting from the analysis of VFDs, the chosen one are the ABB ACS880-107LC. The reason why these VFDs were selected is that in applications where low harmonics, compact integration, high efficiency and precision torque control are critical, the selected product outperforms many general purpose VFDs.

Figure 3.1: ABB VFDs for low and high power applications [14].

Two possible options are available for ACS880-107LC, one working with a 3-phase 380V to 500V input (+10%/-10%) and the other 3-phase 525V to 690V input (+10%/-10%).
They come with air-cooling or liquid-cooling options, depending on the application and performance required. The liquid used to cool down the system is Antifrogen L at a concentration of 25 %, one of the most spread glycol based antifreeze coolant.
The operational areas of the devices are pictured in Figure 3.2.

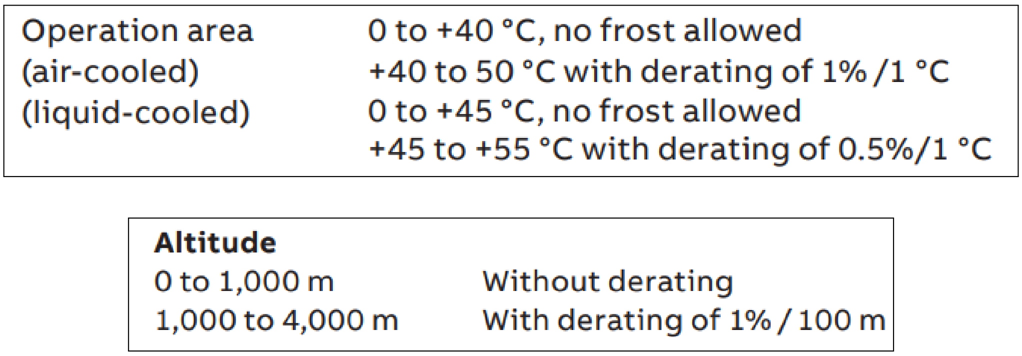

Operation area	0 to +40 °C, no frost allowed
(air-cooled)	+40 to 50 °C with derating of 1% /1 °C
(liquid-cooled)	0 to +45 °C, no frost allowed
	+45 to +55 °C with derating of 0.5%/1 °C

Altitude	
0 to 1,000 m	Without derating
1,000 to 4,000 m	With derating of 1% / 100 m

Figure 3.2: ABB VFDs operations area [14]

The term "derating" refers to the intentional reduction in the VFDs performances to ensure reliable operation of the device when operating out of nominal environmental/internal conditions. Basically when operating out of nominal conditions (for example at altitudes higher than 1000m), a larger VFD will be chosen than the required one to provide the power needed, but in safe conditions.

In the case of 3-phase 380V to 500V input, the liquid cooling option is available only for a range of powers from 55 to 315 kW compared to the air cooling range that reaches values up to 3200 kW. As a consequence the comparison between the two would not be satisfactory from a data/trend point of view.
For this reason the analysis focused on 3-phase input nominal voltage of 690V (range from 525V to 690V) input applications. Data were collected from the catalogue available online [14], transferred to an Excel file and elaborated using Matlab.

The starting point of interest are power losses, from them other parameters such as overall efficiency and cooling flow rates can be analysed.
Power losses are mainly due to the following factors:

- Conduction and switching losses (inside the IGBTs).
- Conduction losses through diodes.
- Conduction losses through DC buses.

Given that the two technologies (air and liquid cooled) share the same bases, in terms of power losses they should be comparable. This assumption is confirmed by the data in Figure 3.3.

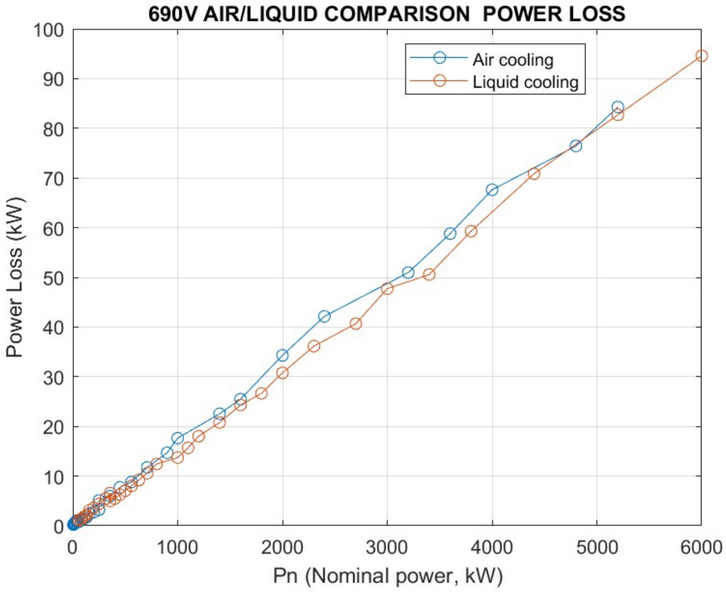

Figure 3.3: Industrial application power loss.

Relating the power losses to their corresponding nominal power, the efficiency factor can be obtained.

$$\eta = \frac{Pn - Ploss}{Pn} * 100$$

The results are shown in Figure 3.4

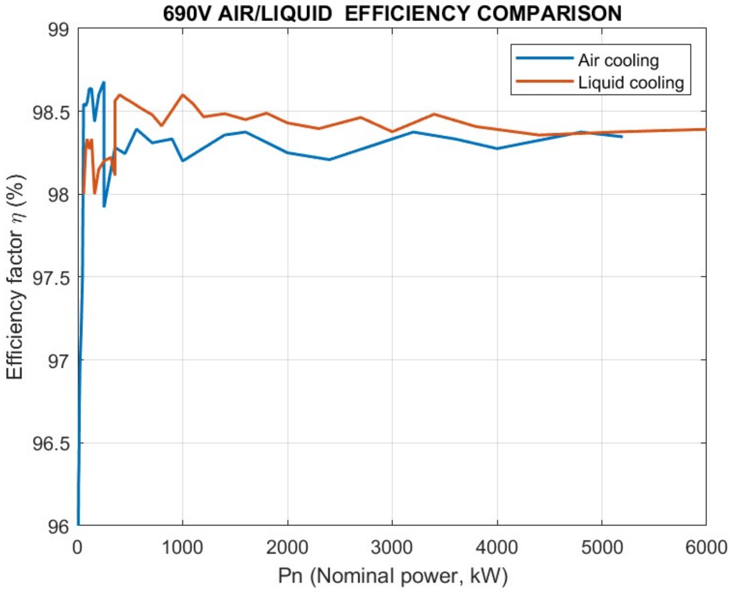

Figure 3.4: Industrial applications efficiency coefficient

The area of interest for the discussion can be limited to the initial transient (range of powers from 5.5kW to 500kW).

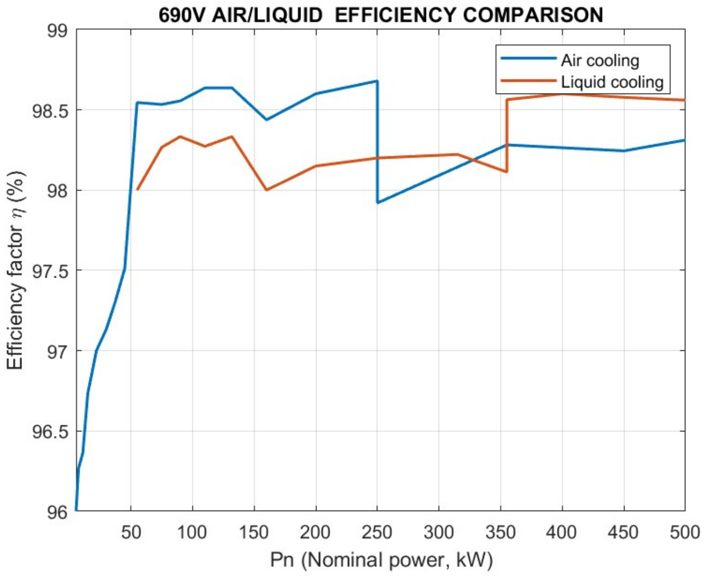

Figure 3.5: Zoom on industrial applications efficiency coefficient (from 5.5kW to 500kW).

As visible from the zoom Figure 3.5, for air cooled low power applications going from 5.5kW to around 55kW the η displays a transient increasing behavior. The reason why low power applications have lower efficiency values is due to the working principle of IGBTs. The IGBTs losses are not just dependent on conduction losses but also on switching losses. Given that at low power we operate at low currents, the conduction losses are limited but the switching losses present high values anyway (making up a high percentage of the total losses). For high voltage applications the switching losses make up a much lower portion of total losses. This, coupled with the fact that normally at higher nominal powers the IGBTs operate at lower frequency, keep the total losses at lower levels compared to the nominal power; leading to better efficiency values.
Efficiency values and power losses are strictly related to flow rates needed to cool down the system. In the following images the flow rates (L/min) are reported.

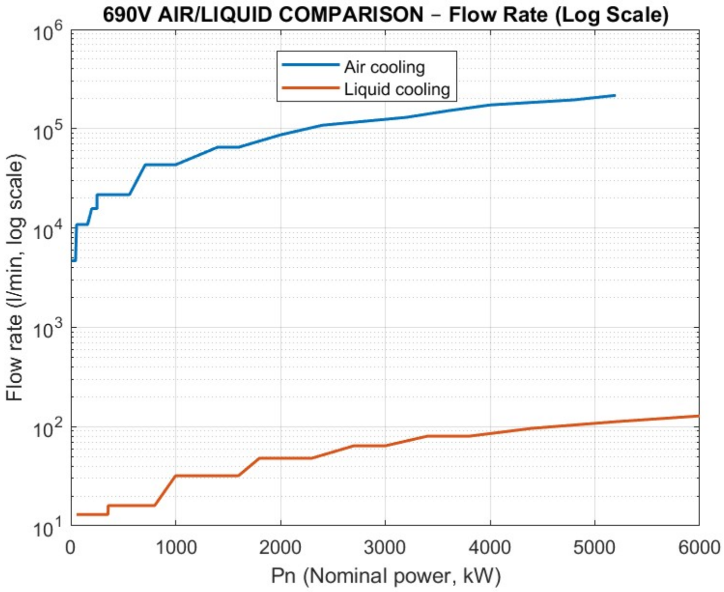

Figure 3.6: Industrial application cooling flow rates.

It's clearly visible how in case of air cooling the flow rates are extremely higher compared to liquid cooling (almost a difference of a 10^3 factor).

The reason is connected to the properties of the fluids.

Substance	ρ **[kg/m³]**	C_P **[kJ/(kg·K)]**
Antifrogen L (25%)	1021 (at 25 °C, liquid phase)	3,6 (at 25 °C)
Air	1,184 (at 25 °C, gaseous phase)	1,005 (at 25 °C)

Table 3.1: Density and specific heat capacity values at 25 °C.

First of all, air is much less dense compared to Antifrogen L 25% that is in liquid form. A difference of a 10^3 factor immediately stands out.
Moreover, air has a much lower C_p coefficient. This means that, given the same mass flow rate, air is able to embrace much less heat compared to Antifrogen L 25%.

Recalling that:

$$Q = m \cdot Cp \cdot \Delta T$$

It can be easily understood that given the same conditions (the same amount of temperature gradient and mass flow rate), the air can dissipate less than a third of the heat dissipated by the coolant liquid.
Different type of cooling requires different type of architecture, affecting the size of the product.

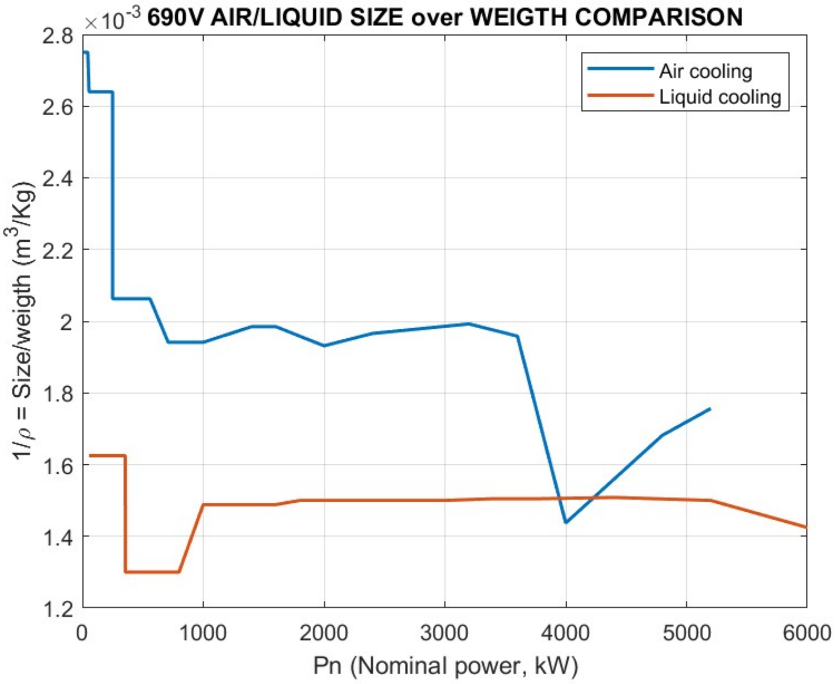

Figure 3.7: Industrial applications size/weight.

As visible air-cooling applications present a higher size/weight factor (a lower density). This comes from the need of including the air fan in the case, occupying more space and leading to a less compact solution.
While liquid cooling applications present almost flat trend, for air cooling it is possible to obtain more compact applications (compared to their power) as the nominal power increases.

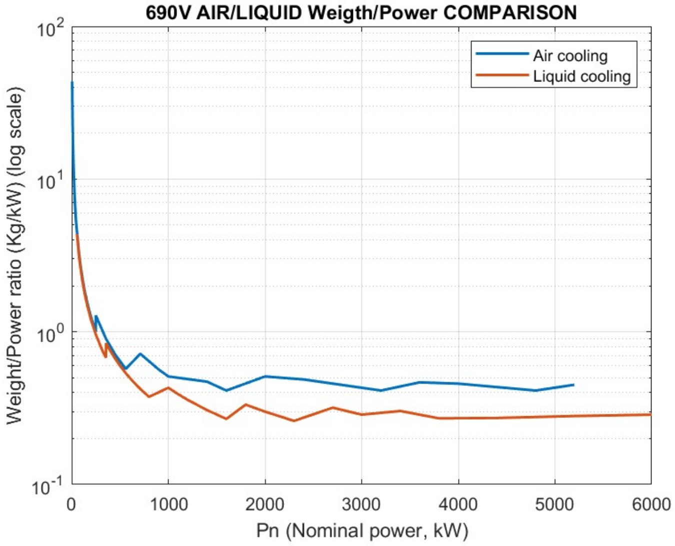

Figure 3.8: Industrial applications weight/power.

In Figure 3.8 the ratio between weight and power is considered.
The trend displayed by industrial applications is almost hyperbolic. The weight compared to power heavily drops when considering applications above 100kW. It goes from an average value of 43 kg/kW at 3.3 kW, to an average value of 2.5 kg/kW for 100 kW applications. Given that for industrial applications the problem of weight and size is not that prominent, there is no big interest in looking for light weight materials and miniaturization in case of low power applications.
All the previously discussed factors come into play when looking at the power density.

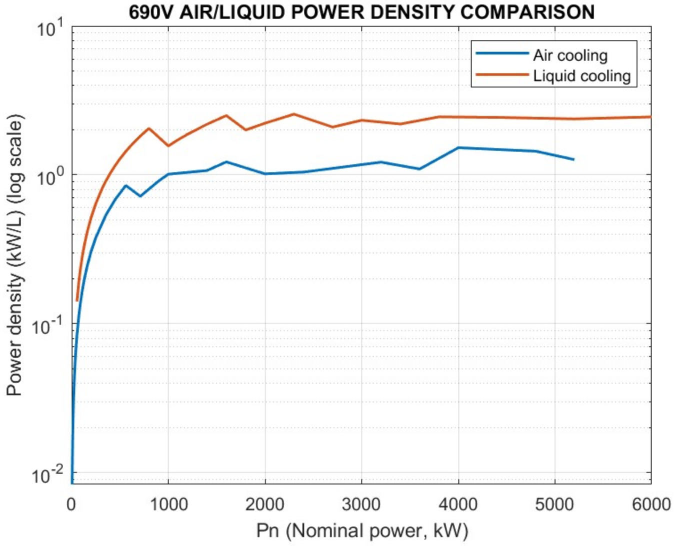

Figure 3.9: Industrial applications power density.

Thanks to higher heat dissipation capacity of liquid cooled systems, it's possible to obtain more compact systems increasing the power density.

3.2 Inverters

Inverters can be divided into two macro groups:

- **AC compression drive inverters**: used to control the speed and torque of electric motors that drive compressors, typically in HVAC systems or small refrigeration units. Their focus is on steady-state operation, energy optimization, and precise process control rather than dynamic performance.
  In automotive application they range from 10 to 100 kW in power.
- **Traction inverters**: are used in electric vehicles (EVs), trains, and other forms of electric transportation to drive traction motors. These inverters convert DC battery power into AC and are optimized for high dynamic performance, fast acceleration and braking, and frequent load variations. They must be compact, efficient, and capable of operating under variable and often harsh conditions.
  In automotive application they range from 100 to 350/450 kW in power.

To outline a general trend, several data should be collected (as it was done for VFD case). However in many cases no satisfactory data-sheets were available online, so the data collected limited to 5 different inverters in power. In particular:

Application	Name on the market	Nominal output power (kVA)	Nominal output current (Arms)
AC compressor drive	ZINSIGHT HS35 [15]	35	60
AC compressor drive	ZINSIGHT HS50 [15]	50	85
Traction inverter	CASCADIA MOTION CM200 DX [16]	255	300
Traction inverter	DANFOSS EC-C1200-450 [17]	300	350
Traction inverter	CASCADIA MOTION CM350SiC [16]	440	500

Table 3.2: Useful data, selected inverters

Through their data it was possible to give an idea of the order of magnitude that comes into play.

Their images are now reported.

Figure 3.10: ZINSIGTH H35 [15]

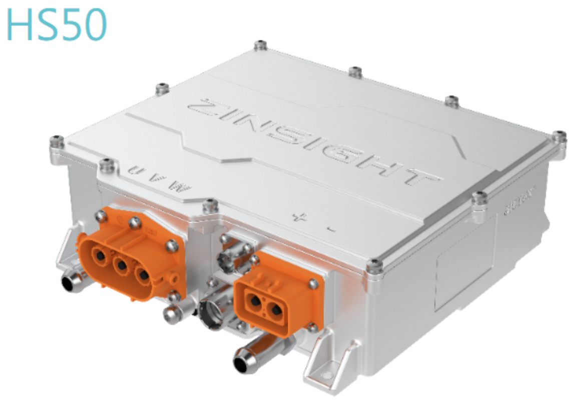

Figure 3.11: ZINSIGTH H50 [15]

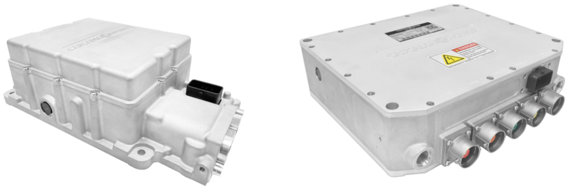

Figure 3.12: CASCADIA MOTION CM200 DX and CASCADIA MOTION CM350SiC [16]

Figure 3.13: DANFOSS EC-C1200-450 [17]

Additional Tables follow at the next page in order to give a proper comparison between the solutions.

Name	Coolant temperature (°C)	Coolant flow rate (L/min)	Coolant type
ZINSIGHT HS35 [15]	25	8	Water Glycol (50:50)
ZINSIGHT HS50 [15]	25	10	Water Glycol (50:50)
CASCADIA MOTION CM200 DX [16]	60	12	Water Glycol (50:50)
DANFOSS EC-C1200-450 [17]	25	10	Water Glycol (50:50)
CASCADIA MOTION CM350SiC [16]	45	24	Water Glycol (50:50)

Table 3.3: Useful data, selected inverters.

Name	Volume size (L)	Weight (Kg)	Pressure drop (kPa)
ZINSIGHT HS35 [15]	3.8	5.2	From 10 to 20
ZINSIGHT HS50 [15]	5	8.1	From 15 to 21
CASCADIA MOTION CM200 DX [16]	6	6.75	30
DANFOSS EC-C1200-450 [17]	12.8	14	10
CASCADIA MOTION CM350SiC [16]	8.2	14.6	55

Table 3.4: Useful data, selected inverters.

The data in Table 3.3 and 3.4 give an overview of the main parameters order of magnitude. Following the line of the previous dissertation, the data were plotted and compared to that of VFDs (inn the power range of inverters, from 35 to 440 kW).

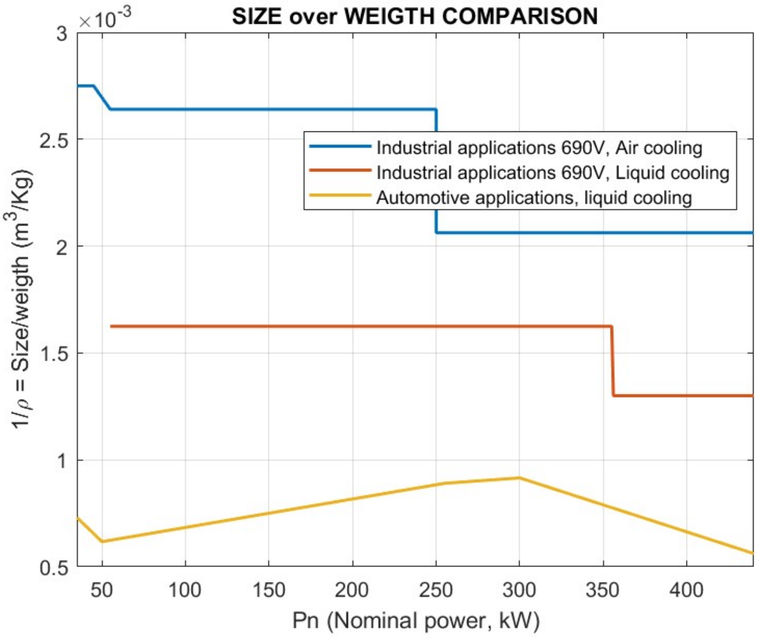

Figure 3.14: VFD vs Inverter size/weight.

It immediately stands out how the size/weight ratio of automotives inverters is lower than industrial supplications. In automotive weight is critical for limiting fuel consumption and low size allows easier integration.

Despite the low size and weight, automotive inverters must express high output powers (especially in the case of traction inverters).

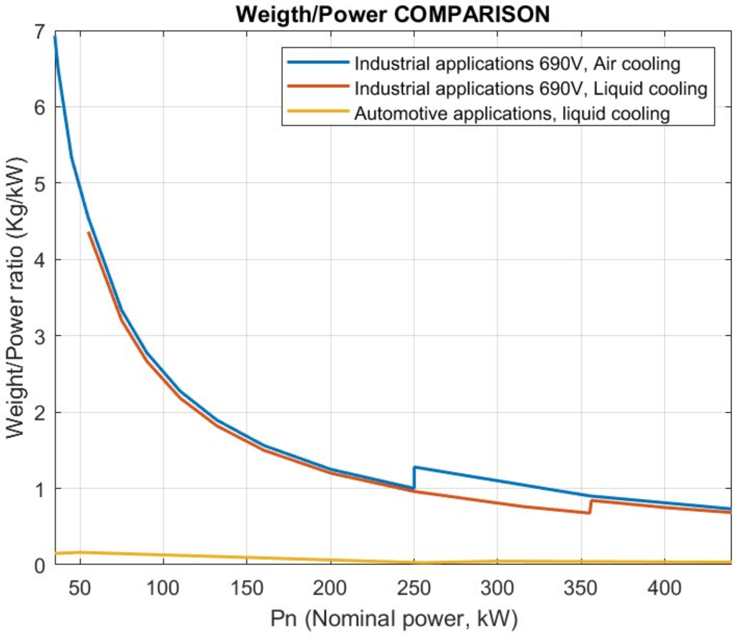

Figure 3.15: VFD vs Inverter weight/power.

This necessity is clearly reflected in the weight/power ratio. Inverters are able to express a remarkably higher power for the same weight unit. This last statement is true for unit size too, as clearly shown in Figure 3.16.

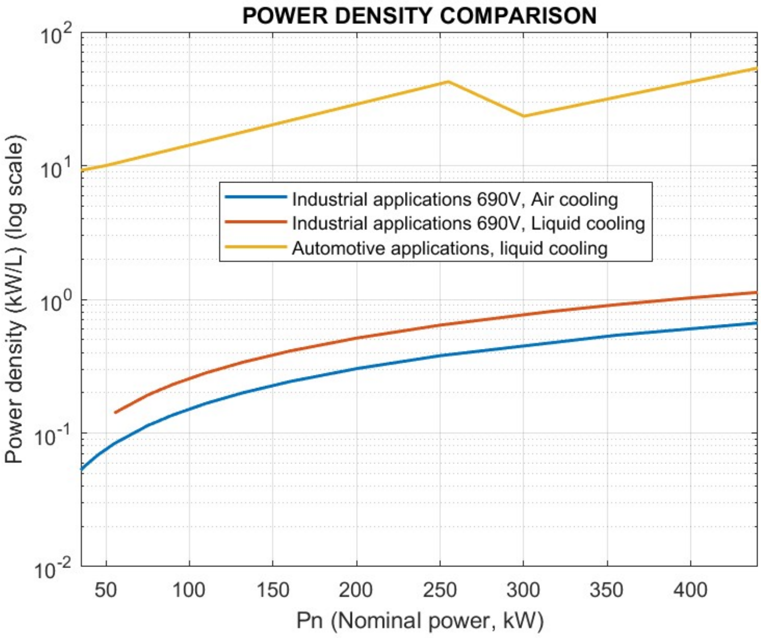

Figure 3.16: VFD vs Inverter power density

Automotive inverters display a power density from 50 to 100 times higher than industrial applications, going from a value of 10 kW/L to a value higher than 50 kW/L (440 kW application). This phenomenon has a great impact of thermal management and its solutions.

4 Inverter Status and Future Trends

Inverters play a central role in today's electrified automotive systems, serving as the backbone for a wide range of applications from controlling HVAC motors to powering high-performance traction drives. As the automotive industry continues its shift toward electrification, the demand for inverters that are not only efficient but also compact, reliable, and cost-effective has grown significantly [18].
Thanks to rapid advancements in power electronics, modern inverters are now capable of delivering high power density and efficiency at lower costs, making them well-suited for widespread use in consumer vehicles. These developments are paving the way for the next generation of electric vehicles.

4.1 Present Scenario

The current status in terms of power density reflects the data collected in section 3.2.
The following image clearly illustrates the historical trend in inverter power density across various hybrid and fully electric vehicle models.

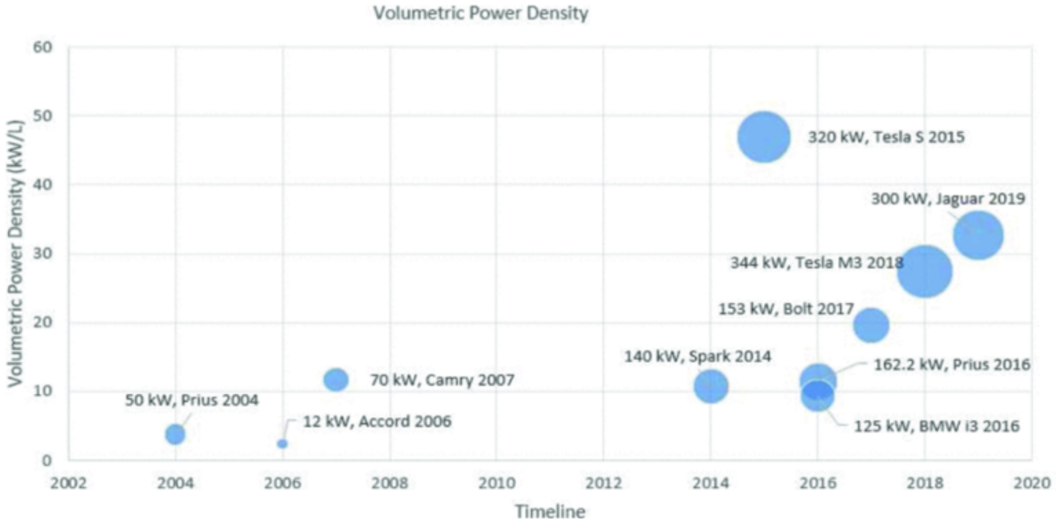

Figure 4.1: Inverter current status, power density trend through the years [18].

Studying the approaches used to reach this kind of performances, it is possible to identify a couple of reasons that drove the evolution. Some of them result to be at a saturation point, while some of them are still in a development stage and outline the future trends of this technology. In particular:

- Packaging strategies: thanks to both electrical and mechanical components size reduction, new stacking strategies could be studied leading to a more efficient space exploitation. (Saturation point almost reached, out of the scope of the thesis).
- Electrical design topologies: new architectures to smooths the ripple current and voltage generated by the switching action of the active devices reducing the high frequency current harmonics (Out of the scope of the thesis).

- Thermal management: cold plates design optimization, new coolant/refrigerant fluids exploitation. (Feasible approaches for **Garret product** will be discussed, outlining the advantages and flaws on the different approaches in terms of size volume and thermal dissipation performances).
- **WBG and UWBG** (wide band gap and ultra wide band gap devices): "WBG devices have demonstrated numerous advantages over Si IGBTs including higher temperature operation, higher breakdown voltages, and higher switching frequencies while reducing both losses and chip size [18]". Thanks to an incredible market growth of the field that exceeds the boundaries of automotive applications, great range of improvement is expected in the next years (Future trend).

These are the key points to keep in mind when looking at future development. They have been identified as potential parameters by DOE (U.S. Department of Energy) towards achieving their 100 kW/L inverter target.

4.2 Emerging Trends and Technological Frontiers

From the above listing it is evident that both thermal management and wide bandgap (WBG) semiconductor devices represent areas with substantial potential for further technological advancement in the coming years. Given that a dedicated solution will be developed for thermal dissipation challenge, the following section will concentrate on the exploration of WBG devices future development.

A closer examination of inverter power electronics reveals that the development trajectory began in the late 1990s with the advent of automotive electrification, marked by the introduction of hybrid vehicles [18]. During the 2010s, the electric vehicle (EV) market experienced significant growth, driven largely by the widespread adoption of hybrid models and an increasing global focus on environmental sustainability.

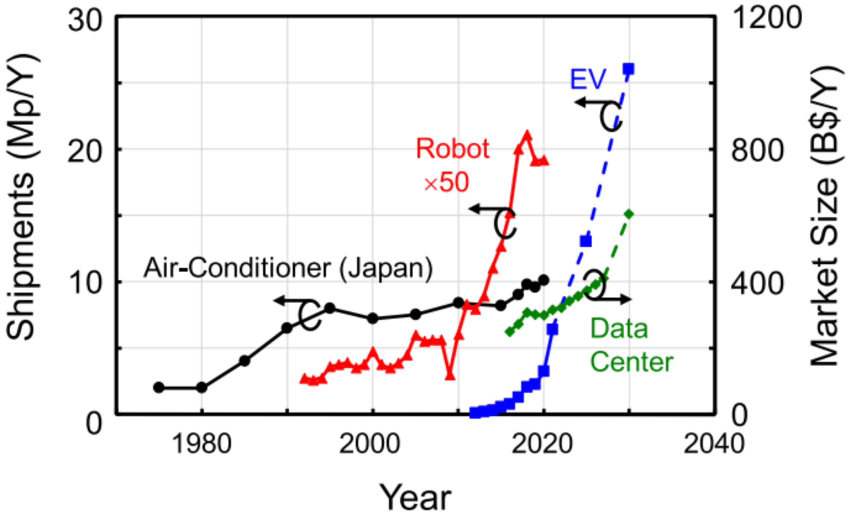

Figure 4.2: Change in driving force in power device business.

"Recently, the evolution of AI technologies opened the door to a new era because big data analysis became a new strong driving force of the semiconductor business, and the directionality of the semiconductor market demands has become clear [19]."

As future technology trends, the semiconductor industry is brimming with vitality affecting all the related fields, inverter power electronics included.

"Ultrawide-bandgap (UWBG) semiconductors, with bandgaps significantly wider than the 3.4 eV of GaN, represent an exciting and challenging new area of research in semiconductor materials, physics, devices, and applications [20]". These include AlGaN/AlN, diamond, Ga_2O_3 and cubic BN.
The interest in these new materials can be easily explained taking as reference the Baliga figure of merit (BFOM).

$$\mathrm{BFOM} = \frac{V_{\mathrm{BR}}^2}{R_{\mathrm{ON,SP}}}$$

where:

- V_{BR} is the **breakdown voltage**, which is the maximum voltage the switch can block when it is off.
- $R_{\mathrm{ON,SP}}$ is the **specific on-resistance**, which is the inverse of the conductance per unit area when the switch is on.

The higher the BFOM, the higher the voltage the device can block when off and/or the lower its resistivity per unit area when on. These two parameters have great effects:

- Higher V_{BR}: A higher breakdown voltage means the MOSFET can withstand greater drain-to-source voltages without entering avalanche breakdown. This is essential in circuits where voltage spikes or transients are common (e.g., motor drives, power supplies). As a consequence reliability and safety are increased.
- Lower $R_{\mathrm{ON,SP}}$: results in lower conduction losses when the power device is on, leading to improved efficiency and reduced heat generation.

The relationship between these two parameters are reported in Figure 4.3.

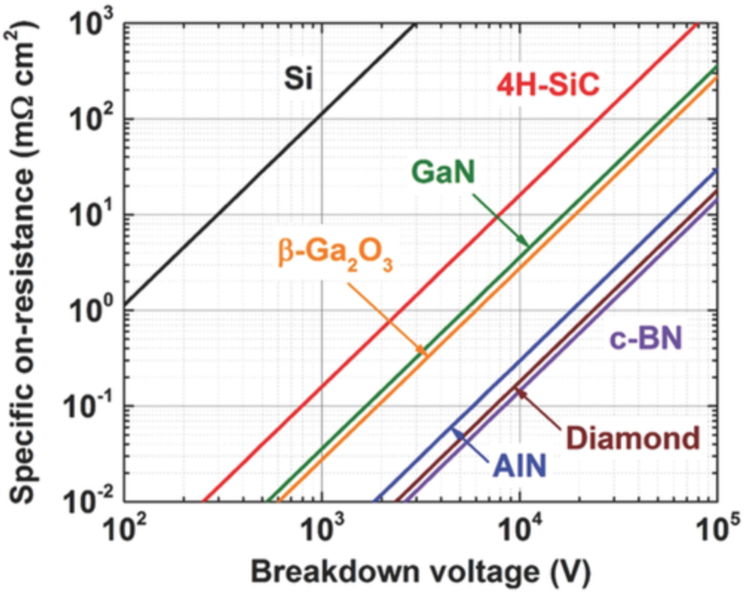

Figure 4.3: Contours of constant Baliga figure-of-merit (BFOM) for various conventional, WBG and UWBG semiconductors, drawn on a log-log scale [20].

The plot shows lines of constant BFOM drawn on a log-log specific on-resistance versus breakdown voltage plot. It's visible how, when taking into considerations UWBG materials, the lines of constant BFOM move towards the right (higher values).
Despite their immense potential to revolutionize device performance, ultra-wide bandgap (UWBG) semiconductors remain in an early stage of development. Although some UWBG materials have been under investigation for one or two decades, practical device demonstrations have only recently emerged. Today, UWBG semiconductors are at a developmental stage comparable to where wide bandgap (WBG) materials like GaN and SiC were in the 1980s: promising but nascent technologies, facing significant research challenges. However, they also offer the possibility of dramatic performance gains not only in existing applications but also in entirely new domains previously thought to be out of reach.

	WBG		**UWBG**		
Material	**GaN**	**4H-SiC**	**AlGaN/AlN**	**β-Ga$_2$O$_3$**	**Diamond**
Bandgap (eV)	3.4	3.3	Up to 6.0	4.9	5.5
Thermal Conductivity ($\mathrm{W\,m^{-1}\,K^{-1}}$)	253	370	253–319	11–27	2290–3450
State-of-the-art substrate quality (dislocations $\cdot$ cm^{-2})	$\approx 10^4$	$\approx 10^2$	$\approx 10^4$	$\approx 10^4$	$\approx 10^5$
State-of-the-art substrate diameter (inches)	8 (on Si)	8	2	4	1
Demonstrated p-type dopability	Good	Good	Poor	No	Good
Demonstrated n-type dopability	Good	Good	Moderate	Good	Moderate

Table 4.1: Comparison of Wide Bandgap (WBG) and Ultra-Wide Bandgap (UWBG) Materials [20].

Each of the three ultra-wide bandgap (UWBG) materials has its own strengths, but also some clear challenges. AlN and β-Ga$_2$O$_3$ really struggle when it comes to p-type doping, which limits their versatility. Diamond, on the other hand, offers great properties but is held back by either small substrate sizes or issues with quality. As a result, ongoing research is actively targeting these issues to drive advancements and enhance the overall performance of these materials.

Currently, the most promising technology is GaN. This technology is already well developed and offers several advantages, including lower production costs and higher efficiency due to reduced switching losses [21]. However the application field of GaN technologies is different from SiC MOSFETs.

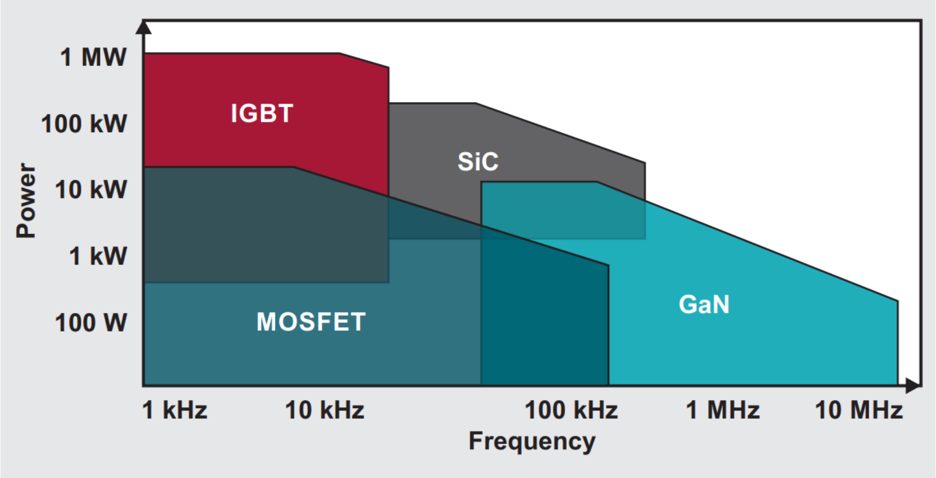

Figure 4.4: High voltage power devices mapping [21].

GaN and SiC serve different power needs in the market. SiC devices offer voltage levels as high as 1,200 V, high current-carrying capabilities and medium switching frequencies. This makes them a good fit for applications such as automotive. GaN FETs, on the other hand, are typically 600-V devices with high switching frequencies. This make them fit for server, telecom and industrial power supplies applications [21].

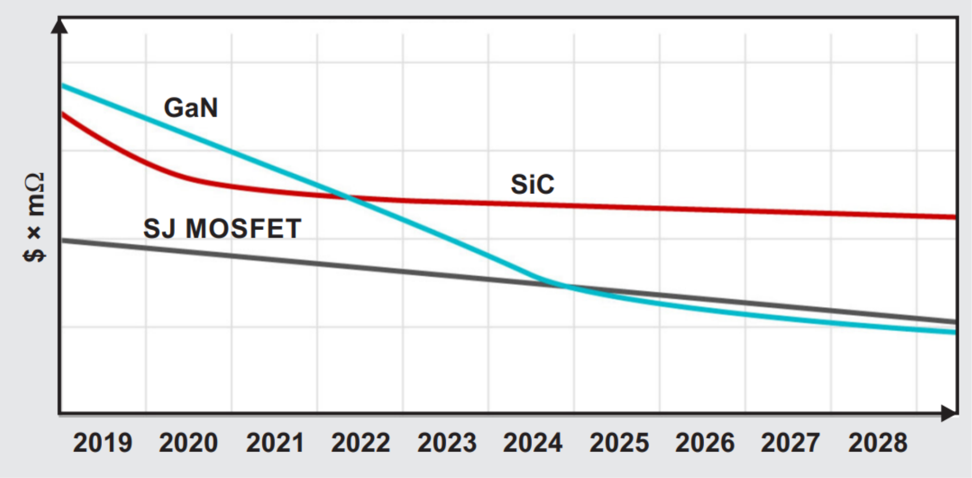

Figure 4.5: Relative cost projection by FET technology [21].

The aim would be to make GaN technologies feasible for automotive applications too. Not only for their excellent technological properties, but also for their lower production cost.

4.3 Chapter take away and useful data

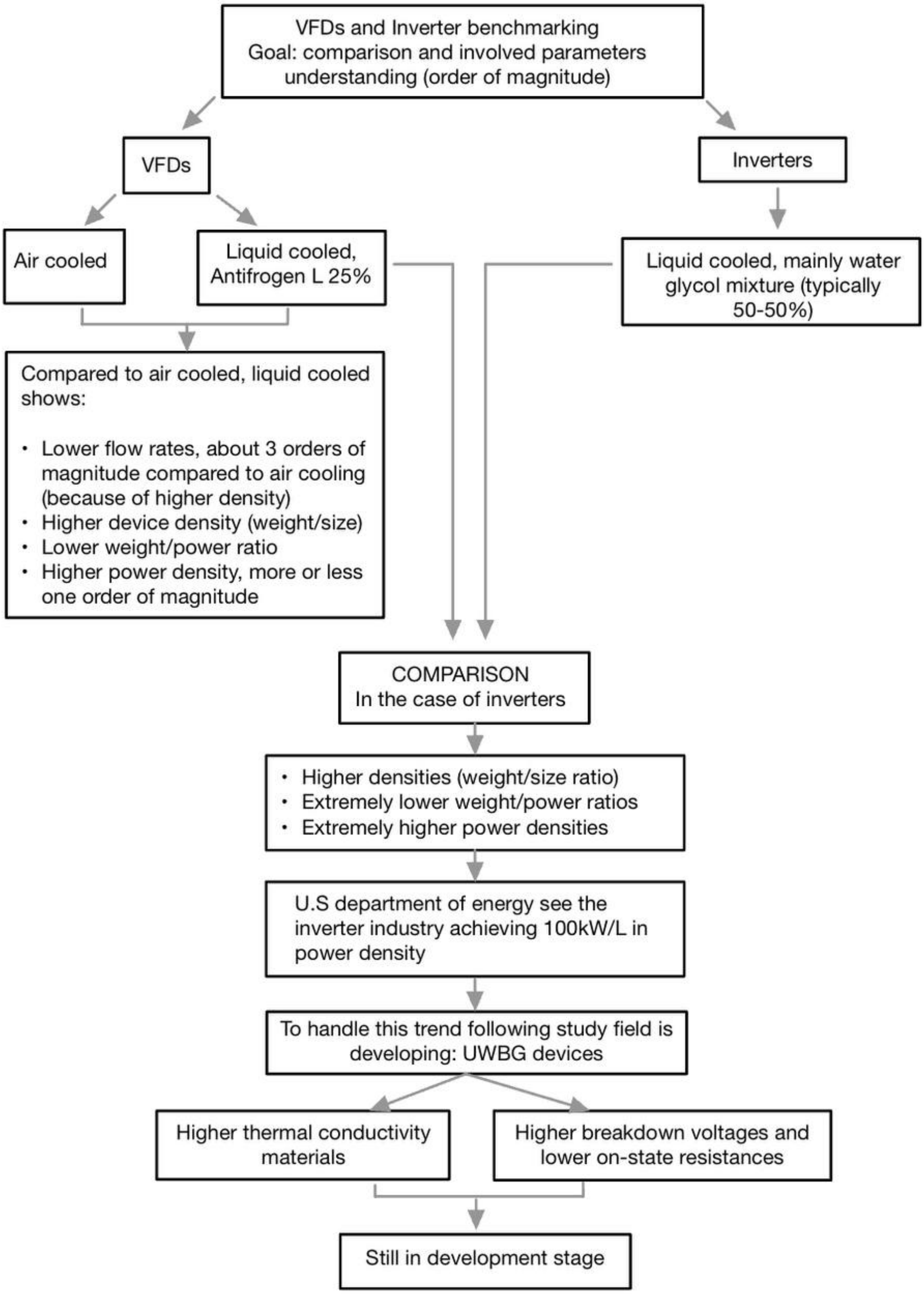

Figure 4.6: Key concept take away tree

5 Compressor architecture

For privacy reason, the actual architecture of the **upcoming Garrett EV cooling compressor cannot be disclosed**. However, given that it has been developed on the line of competitors solutions, a parallel reasoning can be done looking at Danfoss Turbocor.

Turbocor is an oil-free, magnetic bearing compressor technology that eliminates complex oil and refrigerant lubrication management systems. It results in a simplified chiller design, increased reliability and reduced maintenance [22].
It must be outlined that Danfoss Turbocor is meant for high load applications (industrial HVAC). On the contrary, the **Garrett Motion** application is meant for EV cooling (much lower power application). This is not the only difference, the following Table is meant for a quick comparison between the two.

Parameter	Danfoss Turbocor	Garrett compressor
Application	Commercial HVAC systems	Automotive HVAC systems
Power	$\geq$ 200kW	25 kW
Bearing type	Magnetic	Conventional bearings
Lubrication	Absent because not necessary	Oil

Table 5.1: Danfoss Turbocor and Garrett compressor differences.

However the overall components architectures are similar, just scaled to satisfy the different application requirements. The Danfoss Turbocor comes into two different solutions.
The architecture similar to that of Garrett Motion is the double-stage configuration, with one stage positioned on each side of the electric motor.

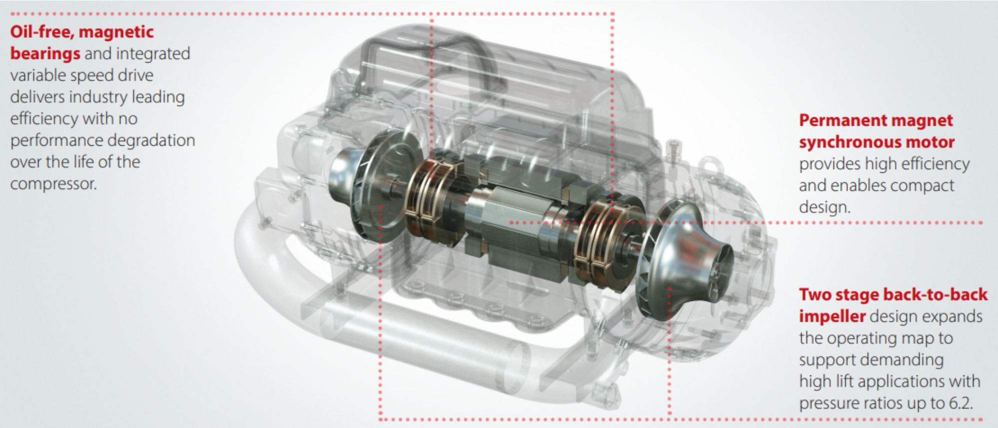

Figure 5.1: Two sides, double stage Danfoss Turbocor compressor [22]

The reason why the general architecture of the compressor is presented is the following: **it deeply affects the positioning and the cooling options adopted to cool down the inverter when in working conditions**.

Based on the architectures shown the only feasible positioning of the inverter is the following: **radial positioning**.

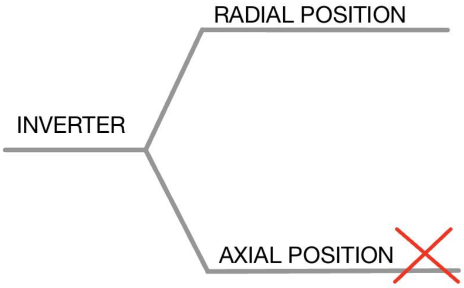

Figure 5.2: Possible inverter positioning.

Radial position: the inverter is placed radially w.r.t the motor case. This choice is purely dictated by necessity (no space axially on the two sides of the electric motor).

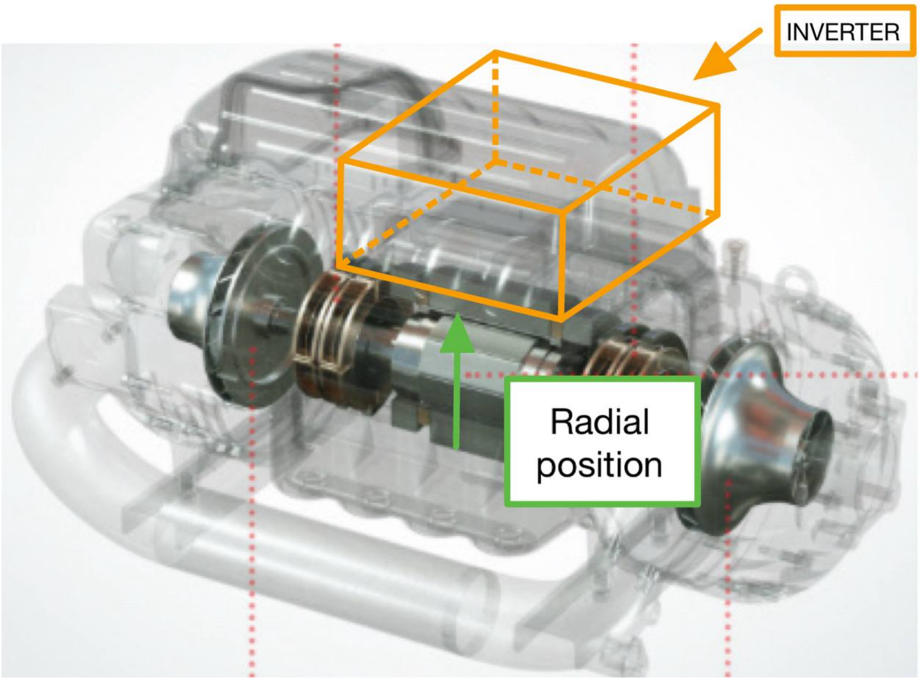

Figure 5.3: Inverter, radial position scheme.

The inverter cooling methods that can be leveraged are two: water (mixture of water and glycol) or refrigerant cooled.

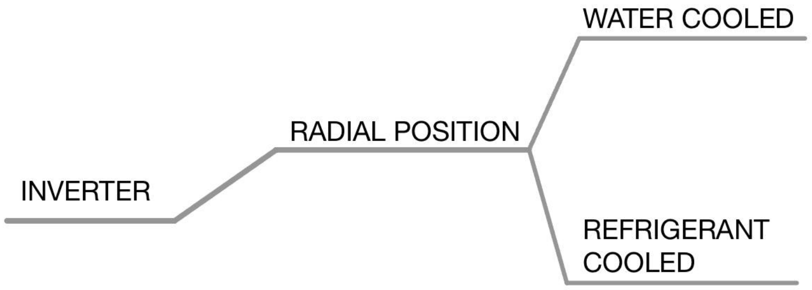

Figure 5.4: Inverter cooling options.

- **Radial water cooling**: water is used to cool down the inverter PCB. It results in a dedicated cooling circuit uncoupled from the refrigerant circuit passing through the compressor.

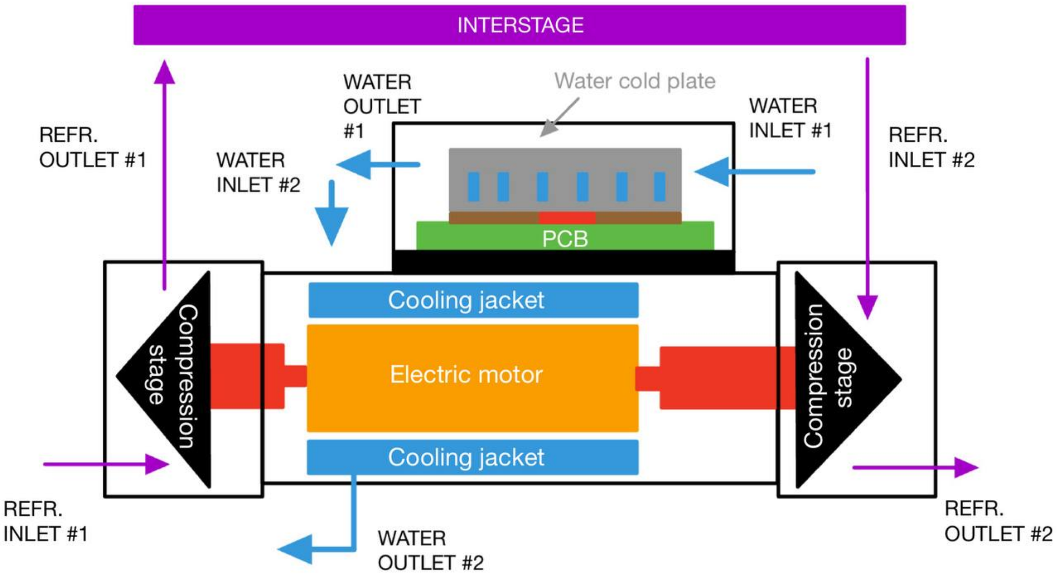

Figure 5.5: Radial and water cooled inverter, double stage compressor.

In Figure 5.5, the electric motor cooling circuit is visible too. It is constituted by a "cooling jacket" that envelopes the motor stator. It shares the same cooling fluid of the inverter, water.

Both the stator of the electric motor and the inverter are water cooled. They share the same fluid and their cooling occurs through the same circuit. While the refrigerant is canalised through the compression stage thanks to a second additional circuit.

- **Radial refrigerant cooling**: Instead of two different coolant we leverage refrigerant as unique cooling fluid for both the inverter and electric motor (before sending it to the compression stage). The refrigerant first goes through the cold plate, then through the motor coolant jacket and finally reaches the compression stage.

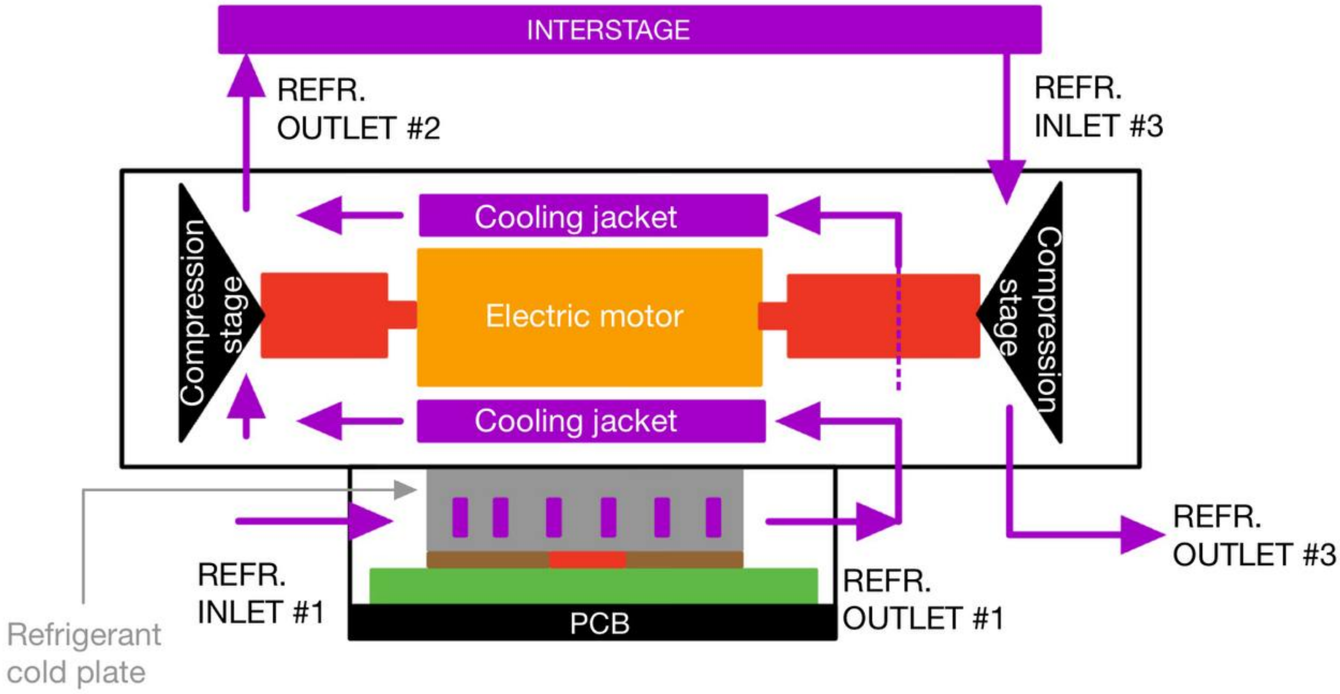

Figure 5.6: Radial and refrigerant cooled inverter, double stage compressor.

Two additional cases can be added to the cooling options tree in Figure 5.4. The inverter can be either integrated into the motor housing or be separate to it. The tree is so updated adding this additional integration choices.

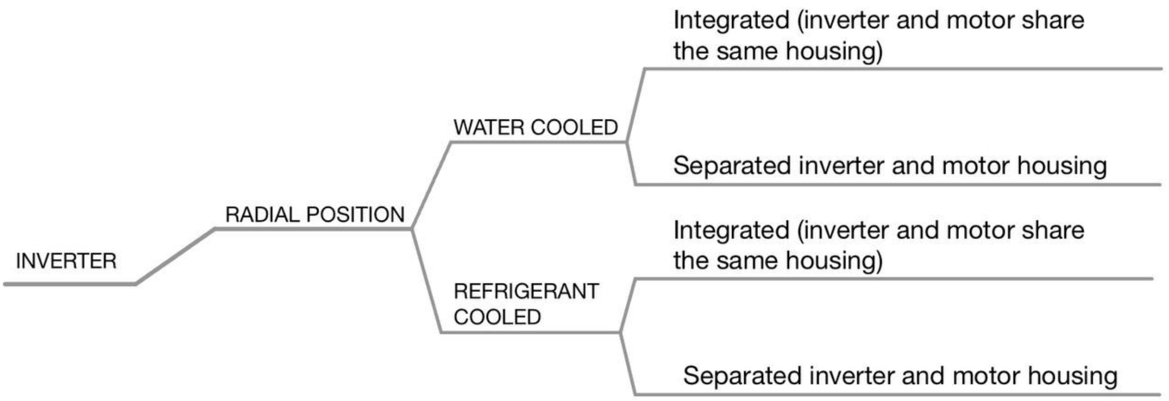

Figure 5.7: Inverter tree options

As it will be discussed, water cooling offers superior thermal performance without compromising the system's compression efficiency. Thanks to water's high specific heat capacity (c_p), relatively high density (ρ), and low dynamic viscosity (μ), it can dissipate significant amounts of heat even at relatively low flow rates. This characteristic results in feasible pressure drops across the cold plate, enhancing cooling efficiency. Additionally, since the inverter cooling circuit is decoupled from the compression circuit, its operation does not interfere with the compressor's performances. However, water cooling requires additional components such as piping, water pump, and heat exchangers, which increase both the system's spatial occupation and cost.

On the other hand, refrigerant cooling enables a more compact and integrated system design. In this configuration, the refrigerant cools the inverter by flowing through the cold plate before entering the compression stage. While this reduces the need for separate cooling circuits and lowers space occupation and costs, it introduces an additional pressure drop (because of high flow rates) in the refrigerant cycle. This drop requires the compressor to consume more energy to achieve the desired pressure level, ultimately reducing the system's overall efficiency.

Inverter position	**Cooling**	**Integration**	**Performance**	**Modularity**	**Cost**
Radial	Water cooled	Integrated with motor housing	✓	●	●
		Separated from motor housing	✓	✓	●
	Refrigerant cooled	Integrated with motor housing	●	●	✓
		Separated from motor housing	●	✓	✓

Table 5.2: Qualitative comparison of inverter cooling configurations.

✓	better
●	worse

Legend of table 5.2

Thanks to the comparative Table 5.2 the best cooling configurations, which correspond to the best solutions, are respectively:

Radial positioning ⇒ Water cooling ⇒ Inverter separated from motor housing.

Radial positioning ⇒ Refrigerant cooling ⇒ Inverter separated from motor housing.

6 Cold plate design

In high-performance thermal management systems, cold plates play a critical role in dissipating heat from electronic components, batteries, or power modules. As power densities increase and component dimensions shrink, traditional air cooling methods often become insufficient. Cold plates offer a highly effective alternative by using liquid cooling to maintain safe operating temperatures, improve reliability, and enhance overall system efficiency.

The following design project focuses on the development of a custom cold plate tailored to specific thermal and mechanical requirements. The objective is to achieve efficient heat removal while minimizing pressure drop and ensuring uniform temperature distribution across the cooling surface.
Key considerations in the design include:

- Material selection
- Channel geometry
- Flow distribution
- Manufacturability

Computational tools and fluid-thermal simulations are used to optimize the performance of the cold plate before physical prototyping. The subject will be tackled step by step.

6.1 System configuration and material stacking

To understand and study thermal conduction and heat dissipation, a discussion on the structure and material used is needed. The study case structure is characterised by top side cooled Mosfets.

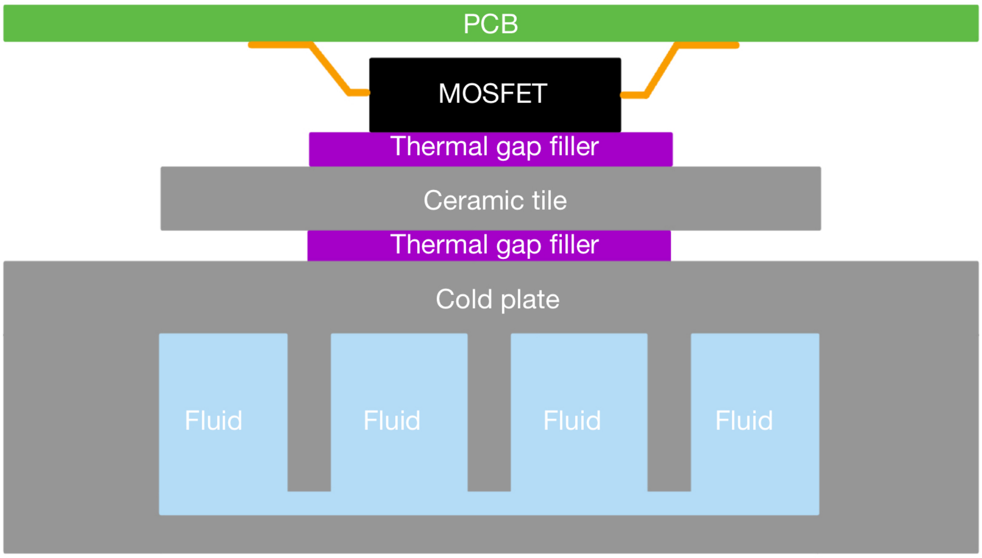

Figure 6.1: Layer structure, top side cooling.

In the developed architecture the layers and materials involved are, starting from the top (visible in Figure 6.1):

- PCB: printed circuit board.
- Mosfet: semiconductor device to be cooled.
- Ceramic tile: ceramic layer used for insulating purposes between the electronics and the cooling fluid.
- Cold plate: heat exchanger used to cool electronic components or systems by transferring heat from the device to a circulating fluid.

6.2 MOSFET device selection and characterization

The selected Mosfet from the Power Engineers team is the **Wolfspeed XE3M0021120U2 1200 V, 21 mΩ Automotive Silicon Carbide MOSFET**.

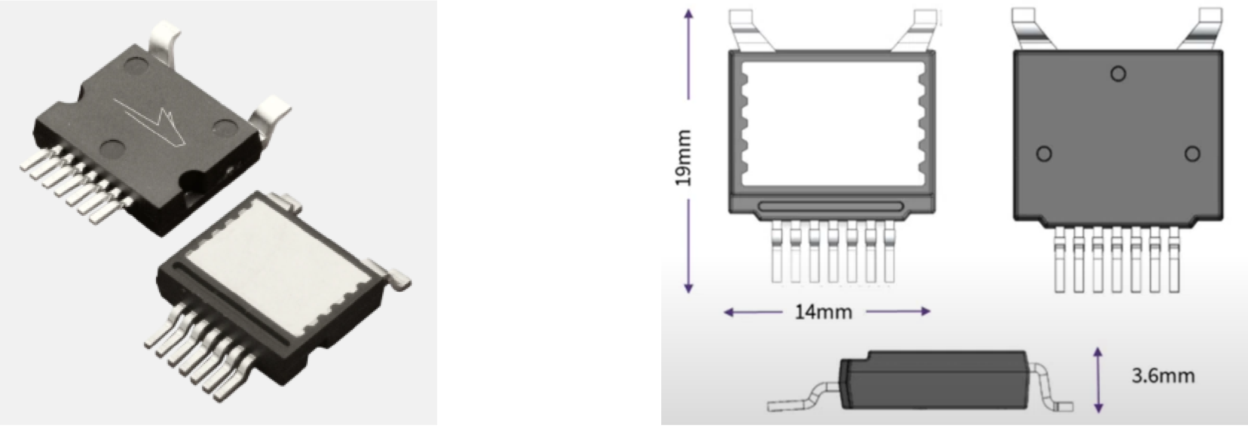

(a) Overlook on the shape [23]

(b) Mosfet dimensions [24].

Figure 6.2: Wolfspeed XE3M0021120U2 1200 V, 21 mΩ.

This product is part of the new Wolfspeed incoming portfolio that expands the offering integrating Top Side Cooled (TSC) package: the U2.
"With options ranging from 650V–1200 V, Wolfspeed's TSC products significantly increase system level power density and efficiency, while improving thermal management and board layout flexibility [25]".

Among the reasons why this Wolfspeed product stands out between its competitors is an **increased package clearance**. Clearance refers to the minimum distance between conductive elements (such as pins). Clearance is crucial for electrical safety preventing short circuits or arcing between conductive parts.

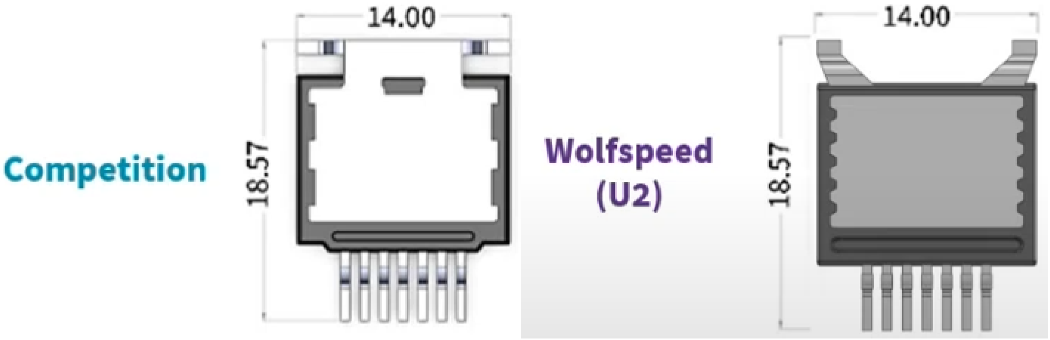

Figure 6.3: Comparison in packages between Wolfspeed products and competitors [24]

Looking at Figure 6.3 it's pretty clear how both the distance between the two upper pins and the distance between top and bottom pins is increased.
For non-disclosure reasons the exact junction to case resistance value cannot be reported, however a plausible value (a conservative one) is used for calculation.

However, the main reason they are particularly well suited for the project is that they are **top-side-cooled MOSFETs**. In this configuration, the MOSFET is mounted beneath the PCB and in direct contact with the heat-dissipating component. This arrangement enables more efficient heat flow, eliminating the thermal resistance associated with the inverter PCB.

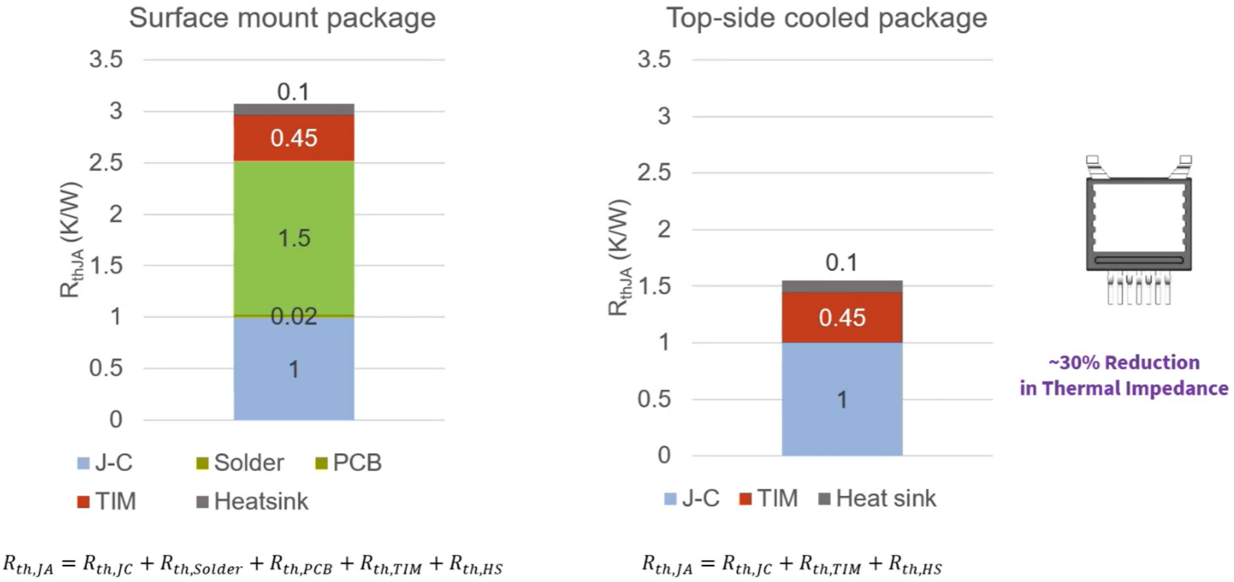

$R_{th,JA} = R_{th,JC} + R_{th,Solder} + R_{th,PCB} + R_{th,TIM} + R_{th,HS}$

$R_{th,JA} = R_{th,JC} + R_{th,TIM} + R_{th,HS}$

Figure 6.4: Top side cooled value proposition [26].

6.3 Theoretical foundation of heat transfer and modelling

From a thermal point of view, every layer can be seen as a flat wall through which heat travels. Each contact surface area will be characterized by a different temperature value due to heat dissipation.

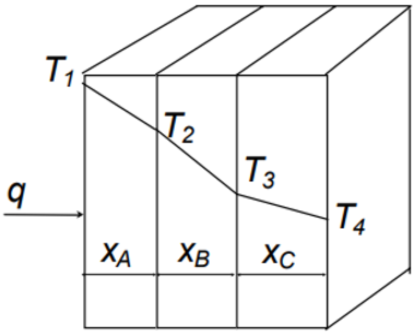

Figure 6.5: Temperature profile through layers [27].

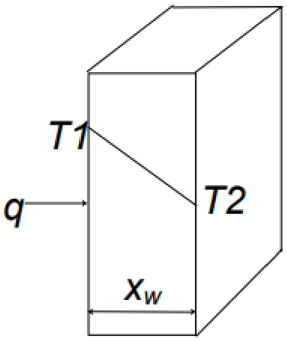

Figure 6.6: Single wall layer example [27].

Consider a flat wall like in Figure 6.6 of thickness Xw, cross-section area A, temperature T1 on one side and T2 on the other with conductivity k (uniform everywhere in the wall).
The letter "q" represents the thermal power travelling through layers measured in (W).
The physical law regulating conduction heat transfer is the Fourier's law:

$$q = -kA\frac{dT}{dx} \tag{6.1}$$

Where:

- q is the thermal power (W),
- k is the material conductivity of the layer (W/(m·K)),
- A is the area of the cross section perpendicular to the direction of q vector (m^2).
- $\frac{dT}{dx}$ is the temperature gradient (K/m).

The formula presented is normally leveraged when studying the problem in **steady state condition**. In physics, a steady state condition refers to a situation in which the macroscopic properties of a system (such as temperature, pressure, velocity, or electric current) do not change with respect to time.
This corresponds exactly to the situation where heat dissipation problems are studied. The interest is not in the transient, but in the maximum temperature values characterizing the system at steady-state.

Steady-state condition brings an important consequence within itself. In case of a multilayer structure it can be stated that, under steady state conditions, each layer is characterized by the same thermal power "q" travelling through it.
This statement is now demonstrated step by step, simplifying the discussion reported in [28].

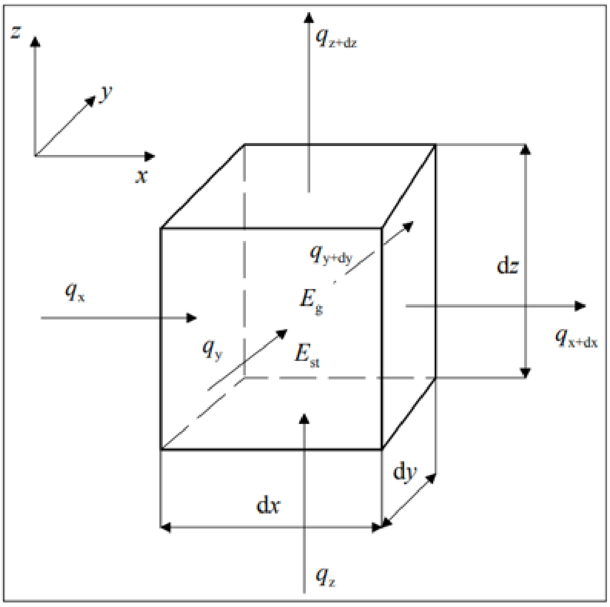

Figure 6.7: infinitesimal volume in 3D space [28].

Keeping in mind that "E" represents energy (J) and its rate w.r.t time $\dot{E}$ represents thermal power (J/s = W), here is the list of terms reported in Figure 6.7 :

- q_x, q_y, and q_z represent the thermal power entering the volume.
- $q(x + \mathrm{d}x)$, $q(y + \mathrm{d}y)$, and $q(z + \mathrm{d}z)$ represent the thermal power exiting the volume.
- $\dot{E}_g$ is the total thermal power generated inside the volume. We will assume that the generation is uniform throughout it.
- $\dot{E}_{\text{in}}$ is the thermal power entering the small volume by conduction. We consider it positive according to the usual thermodynamic conventions.
- $\dot{E}_{\text{out}}$ is the thermal power leaving the small volume by conduction. We consider it negative.
- $\dot{E}_{\text{est}}$ represents the rate of change of the energy in the system.

The energy balance if the infinitesimal volume leads to:

$$\dot{E}_{in} + \dot{E}_{out} + \dot{E}_g = \dot{E}_{st}$$

Considering that:

$$\dot{E}_{in} = q_x + q_y + q_z$$

$$\dot{E}_{out} = -(q_{x+dx} + q_{y+dy} + q_{z+dz})$$

Assuming that heat generation is uniform throughout the volume:

$$\dot{E}_g = q_g dV = q_g dx\, dy\, dz$$

Where q_g represents the thermal power w.r.t volume (W/m^3).

Moreover, assuming that c_v is the thermal capacity at constant volume (J/kg/°C), $\dot{E}_{st}$ has the following shape:

$$\dot{E}_{st} = \rho\, dV\, c_v \frac{\partial T}{\partial t} = \rho\, c_v \frac{\partial T}{\partial t} dx\, dy\, dz$$

The final equation obtained is:

$$q_x + q_y + q_z - (q_{x+dx} + q_{y+dy} + q_{z+dz}) + \dot{q}_g\, dx\, dy\, dz = \rho\, c_v\, \frac{\partial T}{\partial \tau}\, dx\, dy\, dz$$

By definition, at stationary condition no parameters are changing with respect to time, so $\dot{E}_{st}$ is equal to zero. Moreover, if no internal heat is generated $\dot{E}_g$ is zero in value too.
The following is obtained:

$$q_x + q_y + q_z - (q_{x+dx} + q_{y+dy} + q_{z+dz}) = 0$$
$$(q_x + q_y + q_z) = (q_{x+dx} + q_{y+dy} + q_{z+dz})$$

This means that the thermal power entering the volume is equal to thermal power exiting it. As a consequence the statement is demonstrated: "In case of a multilayer structure, it can be stated that, under steady state conditions, each layer is characterized by the same thermal power "q" travelling through it".

This assumption simplifies the calculation of the temperatures at the layers interfaces. Integrating the formula 6.1, we obtain the next equation.

$$q = \frac{T_1 - T_2}{\frac{X_w}{kA}} = \frac{T_1 - T_2}{R} \tag{6.2}$$

Where R= $X_w/(k \cdot A)$ is the resistance of heat transfer of the wall (W/m/k), while (T1-T2) is the temperature difference, the driving force of heat transfer.
Once the thermal power and the maximum temperature at the junction is given as parameters, the temperatures at the interfaces between materials can be calculated and the temperature profile obtained.

6.4 Study case thermal model

Taking a closer look at the problem and adopting the thermal model previously discussed, it is possible to obtain the multi-layer structure in Figure 6.8.

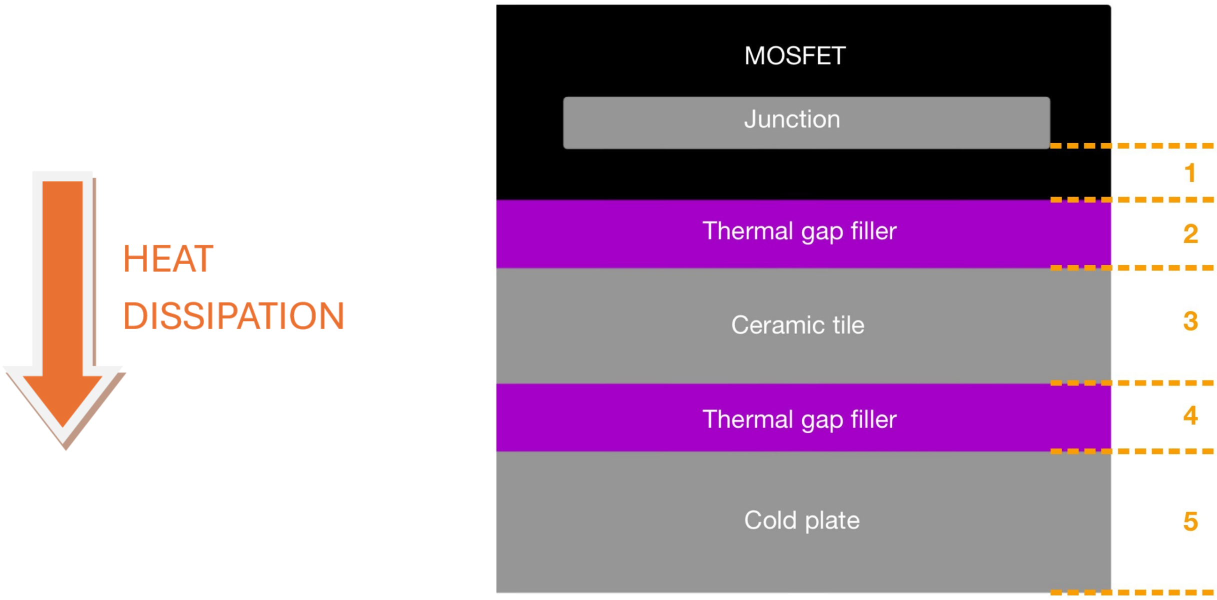

Figure 6.8: Layers structure.

<u>REMARK</u>: When developing the equivalent thermal model, the case of the Mosfet must be considered (layer 1 in Figure 6.8). The heat travels from the Mosfet junction through the case to the other bottom layers.

A first approach to the problem led to the following layer thicknesses.

Layer number	Thickness (mm)
1	Non present on datasheet [29]
2	0.1
3	1
4	0.1
5	To be determined

Table 6.1: Layer thicknesses table.

The ceramic tile thickness is determined to satisfy the insulation requirements (between PCB and fluid) set by electronics engineering team. The value of 1 mm results to be overestimated, but it's assumed as starting point to develop a proper discussion.

While the displayed thermal gap filler thickness is a reasonable value resulting from lab testing. It is low enough to ensure thermal performance while addressing problems such as possible misalignment of the layers while stacking them and enough glueing power.

In further development, these values will be adjusted according to the most suitable and feasible technical solution. Each layer is characterised by its own resistance value (K/W), represented in Figure 6.9 in a graphical approach.

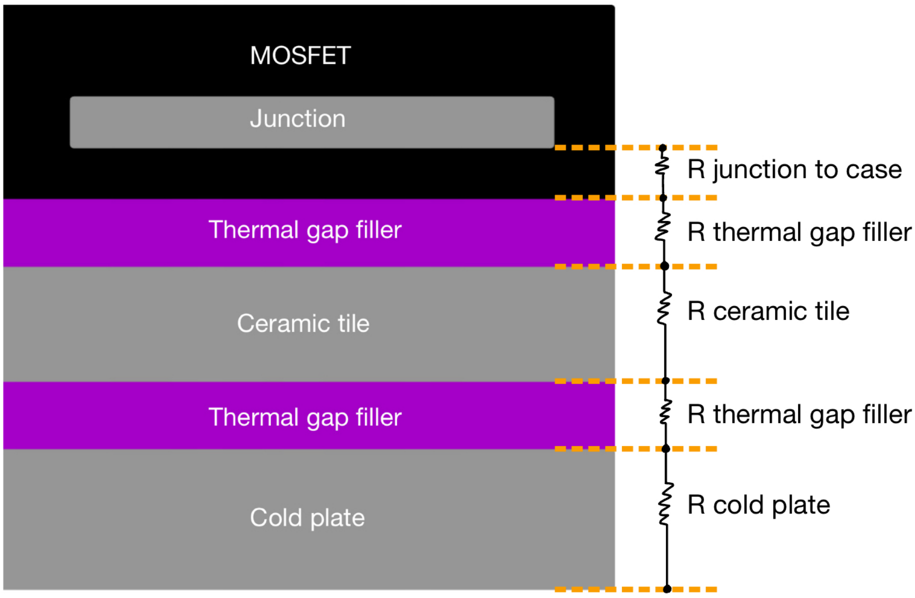

Figure 6.9: Thermal resistances.

The selected materials are described, together with the their thermal properties, in the following Table.

Layer	Material	Thermal conductivity k (W/m/K)	Thermal resistance R (K/W)
Junction to case (n. 1 in Fig. 6.8)	Epoxy resin	Not available in data-sheet	0.3 **(Conservative value for non disclosure reasons)**
Thermal gap filler (n. 2 and 4 in Fig. 6.8)	CoolTherm SC-1600 [30]	3.7	To be calculated
Ceramic tile (n. 3 in Fig. 6.8)	Aluminium nitrite [31]	170	To be calculated
Cold plate (n. 5 in Fig. 6.8)	Aluminum 6061-T6 [32]	167	To be calculated

Table 6.2: Selected materials and their thermal properties.

To complete the table filling the thermal resistances value, the following equation is leveraged:

$$R = \frac{L}{(k \cdot A)}$$

Where:

- k: Thermal conductivity in (W/m/K)
- A: Surface area of heat exchange during conduction.

The only missing data is the surface area of heat exchange. This corresponds to the surface are of heat exchange of the Mosfet. **For non-disclosure reasons the exact value cannot be reported**, however a plausible value (a conservative one) is used for calculation.

$$A = \text{Mosfet heat conduction surface area} = 100\ mm^2$$

Gathering together the data displayed in Table 6.1 and Table 6.3, the following completed Table is obtained (except for the cold plate case).

Layer	Material	Thermal conductivity k (W/m/K)	Thermal resistance R (K/W)
Junction to case (n. 1 in Fig. 6.8)	Epoxy resin	Not available in data-sheet	0.3
Thermal gap filler (n. 2 and 4 in Fig. 6.8)	CoolTherm SC-1600 [30]	3.7	0.27
Ceramic tile (n. 3 in Fig. 6.8)	Aluminium nitrite [31]	170	0.06
Cold plate (n. 5 in Fig. 6.8)	Aluminum 6061-T6 [32]	167	?

Table 6.3: Selected materials and their thermal properties.

The missing cold plate expected resistance can be obtained through some easy steps. At steady state conditions, the following equation applies:

$$P = \frac{T_{\text{junction}} - T_{\text{fluid}}}{2R_{\text{TIM}} + R_{\text{ceramic tile}} + R_{\text{junction-to-case}} + R_{\text{cold plate}}}$$

From which we can obtain the maximum cold plate thermal resistance value:

$$R_{\text{heat sink}} = \frac{T_{\text{junction}} - T_{\text{fluid}}}{P} - (2R_{\text{TIM}} + R_{\text{ceramic tile}} + R_{\text{junction-to-case}})$$

However to proceed some constraints must be applied. They are entirely summarized in Table 6.4.

Project Constraints	
Power to be dissipated (per FET)	100 W
Mosfet heat exchange area	100 mm^2
Maximum junction temperature (from data-sheet [29])	175 °C
Project junction temperature (to enhance lifetime of FET)	150 °C
Temperature of the coolant	40 °C

Table 6.4: Project constraints

Proceeding with the calculations, the following summarizing Table 6.5 is obtained.

Layer	Material	Thickness (mm)	Thermal resistance R (K/W)
Junction to case (n. 1 in Fig. 6.8)	Epoxy resin	Not available in data-sheet. Set to a value equal to 1 mm	0.3
Thermal gap filler (n. 2 and 4 in Fig. 6.8)	CoolTherm SC-1600 [30]	0.1	0.27
Ceramic tile (n. 3 in Fig. 6.8)	Aluminium nitrite [31]	1	0.06
Cold plate (n. 5 in Fig. 6.8)	Aluminum 6061-T6 [32]	3.35	< 0.201

Table 6.5: Project layers properties

Conclusions:

- a) When thermal gap filler and ceramic tile parameters are set, to meet heat dissipation requirements the thermal resistance of the cold plate must be lower than a calculated threshold.
- b) It can be remarked how the the thermal gap filler layers are the one that most affect heat dissipation. Indeed they are the one that, between the layers with "tunable" resistance (that can be affected by project choices), present the highest value. As a consequence it can be stated that the choice of the thermal gap filler has great influence in heat dissipation and its choice should be addressed properly.

Once the resistances are defined the last step is determining the temperature profile across the layers. Through calculation the following plots were obtained.

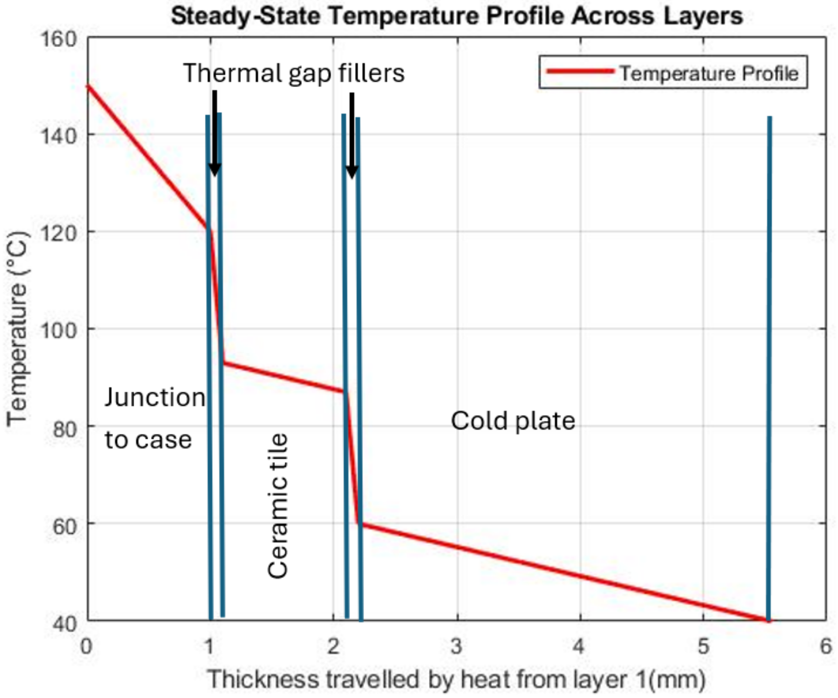

Figure 6.10: Steady-state temperature profile across layers.

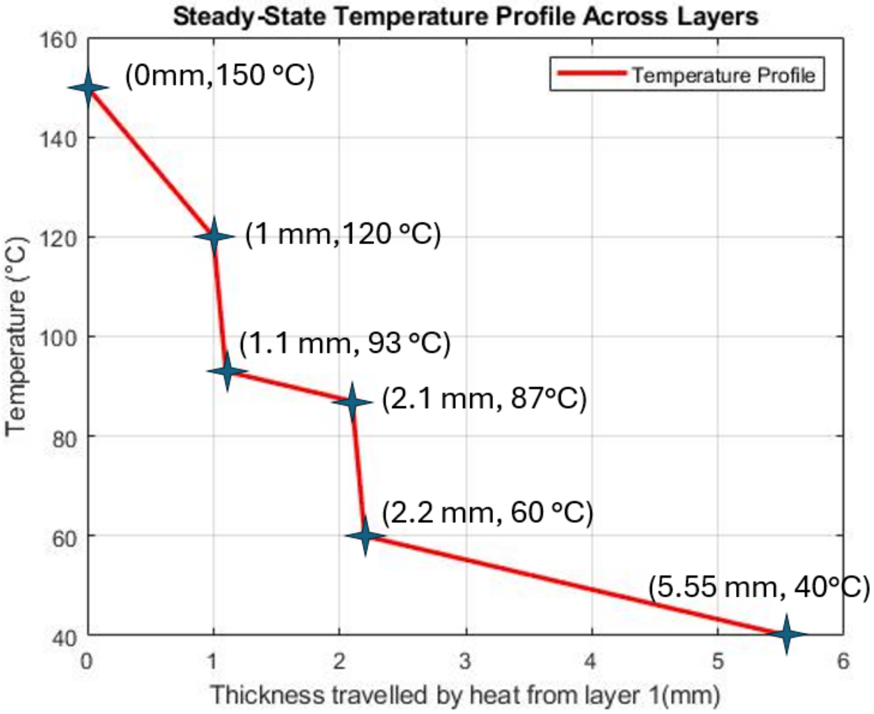

Figure 6.11: Temperatures data at layers interface.

7 Water Glycol cooling 50-50%

In real applications, pure water is never used alone in cooling applications. Water is always mixed with additives to improve the following properties:

- Operating temperature range (freezing prevention and boiling point raise).
- Corrosion power of the fluid.
- System stability over time.

In inverter cooling applications a water glycol mixture 50-50% in volume is used. Here is a properties comparative table.

Parameter at 40°C	Water (Garrett Motion internal data [33])	Water glycol 50-50% in volume (Garrett Motion internal data [33])	Comment
ρ (Kg/m^3)	997,3	1075,4	Density values are comparable.
μ (Pa·s)	$9{,}363 \cdot 10^{-4}$	$2{,}495 \cdot 10^{-3}$	A higher dynamic viscosity affects both turbulence and the fluid - cold plate interaction at the boundary layer.
c_p (J/(Kg·K))	4180	3404,6	Lower specific thermal coefficient, faster heating up of the fluid.
K (W/(m·K))	0,606	0,404	Lower thermal diffusivity α inside the fluid.
ν (m^2/s)	$9{,}338 \cdot 10^{-7}$	$2{,}320 \cdot 10^{-6}$	Same comment as for μ (indeed $\nu = \mu/\rho$).

Table 7.1: Water and water glycol (50-50%) comparison table [33].

Leveraging water-glycol instead of water brings changes in cooling efficiency. Some of them have already been discussed in Table 7.1. Now a proper theoretical discussion is developed (material source: [34]).

To benefit from efficient cooling, the goal is keeping high the convective heat transfer coefficient h (W/(m^2·K)). This parameter depends on Nu number (dimensionless).

$$h = \frac{Nu \cdot K}{D_h}$$

Where:

- K is the thermal conductivity [W/(m·K)].
- D_h is the hydraulic diameter (m). It is defined as $D_h = \frac{4 \cdot A}{P}$, where A is the cross section area and P is the wetted perimeter.

Nu is, in turn, function of other two parameters, *Re* and *Pr* numbers (dimensionless).

$$Nu = f(Re,\ Pr) = X \cdot Re^m \cdot Pr^{1/3}$$

Where X and m are coefficients dependent on the flow conditions. If Pr $>$ 0.6 :

- X = 0.664 and m = 1/2 in case of laminar flow (Re $<$ 4000 for a pipe).
- X = 0.037 and m = 0.8 in case of turbulent flow (Re $>$ 4000 for a pipe)

The *Re* number is a measure of turbulence.

$$Re = \frac{\rho \cdot v \cdot D_h}{\mu}$$

Where:

- ρ is the density of the fluid (Kg/m^3).
- v is the fluid velocity (m/s).
- μ is the dynamic viscosity (Pa · s).

While the *Pr* number compares the rate of momentum diffusion (viscous effects) to the rate of thermal diffusion (heat conduction) in a fluid.

$$\mathrm{Pr} = \frac{\nu}{\alpha}$$

Where:

- ν = kinematic viscosity (m^2/s)
- α = thermal diffusivity (m^2/s)

Alternatively, using more fundamental properties:

$$\mathrm{Pr} = \frac{c_p \mu}{k}$$

Where:

- c_p = specific heat at constant pressure [J/(kg·K)]
- μ = dynamic viscosity (Pa·s) or [kg/(m·s)]
- k = thermal conductivity [W/(m·K)]

The Prandtl number tells us how fast momentum diffuses compared to heat.

So under the same conditions, the following comparative Table can be built.

Parameter	**Water**	**Water-Glycol 50-50% (vol.)**
Reynolds number (Re)	↑	↓↓
Prandtl number (Pr)	↓	↑

Table 7.2: Comparison between water and a 50% water-glycol mixture in terms of Reynolds and Prandtl numbers.

As a consequence in case of turbulent flow, we can expect that the usage of water-glycol as cooling fluid can worsen a bit the performances when compared to pure water. Nevertheless it's employment it's necessary for the reasons stated in the chapter introduction.

Even if $Pr^{1/3} \uparrow$ the $Re^{0.8} \downarrow\downarrow \Rightarrow Nu \downarrow \Rightarrow h \downarrow \Rightarrow$ Lower heat dissipation $\Rightarrow$ Higher T_j. Moreover, in terms of pressure drop a slight increase in pressure drop is expected because of the higher viscosity of the fluid.

The theoretical analysis presented not only serves as an introduction to the topic but also establishes a common foundation for understanding convection heat transfer. This latter point, in particular, will serve as underlying thread throughout the subsequent chapters when exploring the different cooling methods.

The above considerations have been confirmed by simulation results. The specific data are not reported, pure water cooling is not in the focus of this dissertation.

7.1 Initial design, simulation setup

Once the necessary data are obtained from the 1D thermal model, a preliminary 3D model of the cold plate (using Onshape software) can be developed by incorporating relevant constraints. **This initial model is not intended to represent the final geometry** of the cold plate, but rather to provide an estimate of the general scale, including overall volume and channel dimensions. To develop it, besides data from Table 6.5, from the overall **Garret compression stage CAD** the following conclusions were deduced:

- Mosfet PCB positioning.
- Maximum available volume to place the cold plate in the inverter case.
- Overall dimensions distribution.

First an exploded view of the assembly is proposed.

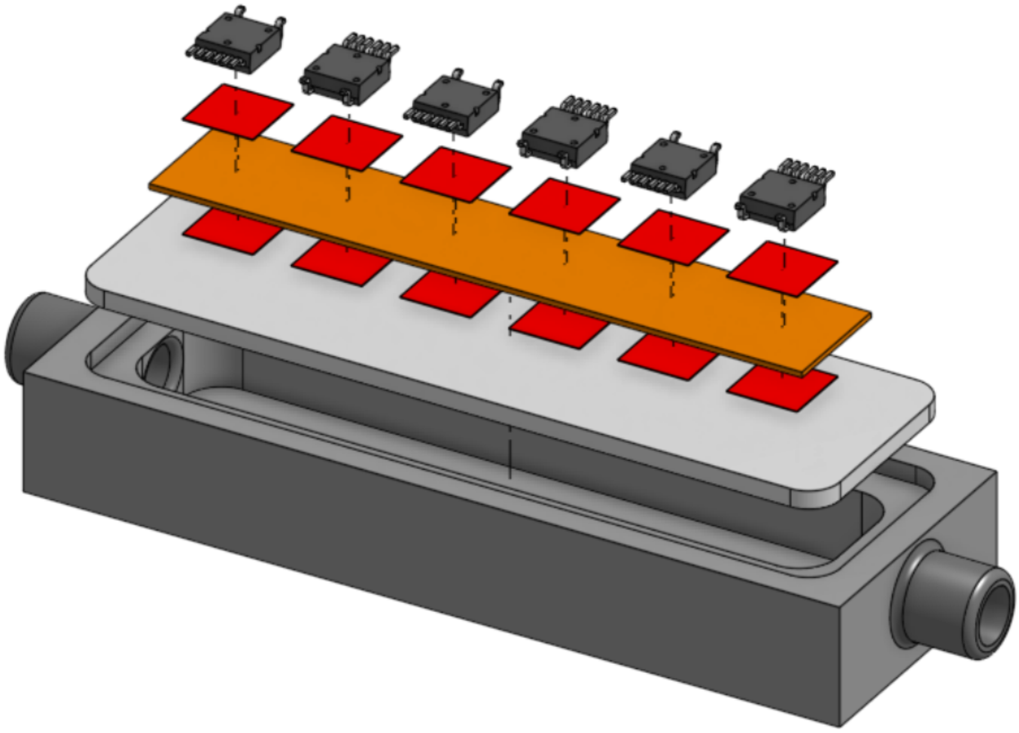

Figure 7.1: Initial simplified model, exploded view.

All the layers are visible: cooling channel (dark grey), cold plate (grey), thermal interface (red squares), ceramic layer (brown) and Mosfets. Their thicknesses and materials are the one specified in Table 6.5.

Now the general dimensions of interest of the model are provided.

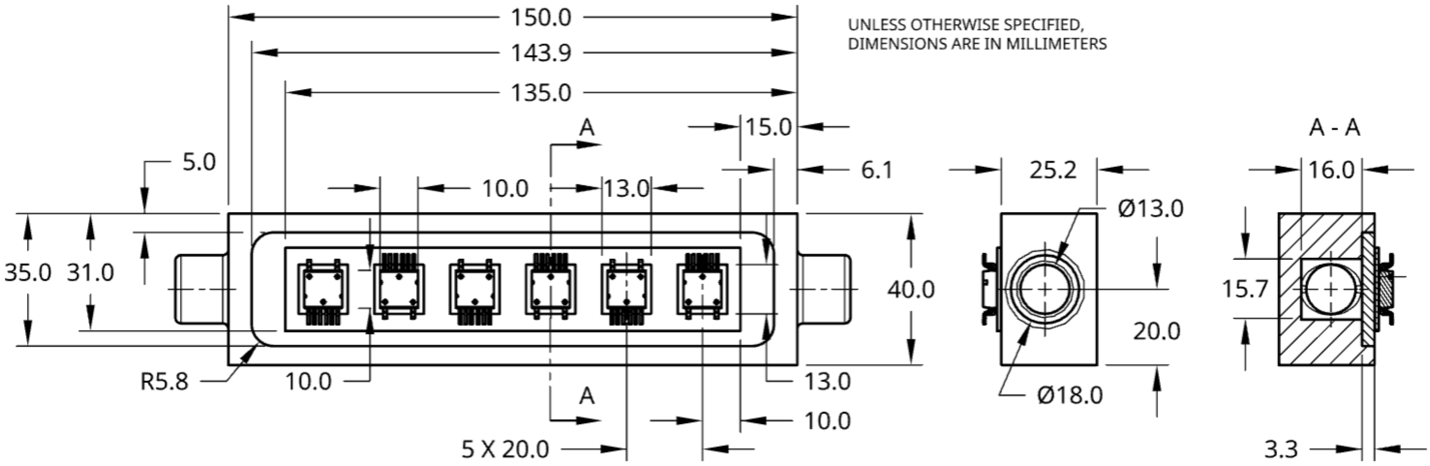

Figure 7.2: Model quotation.

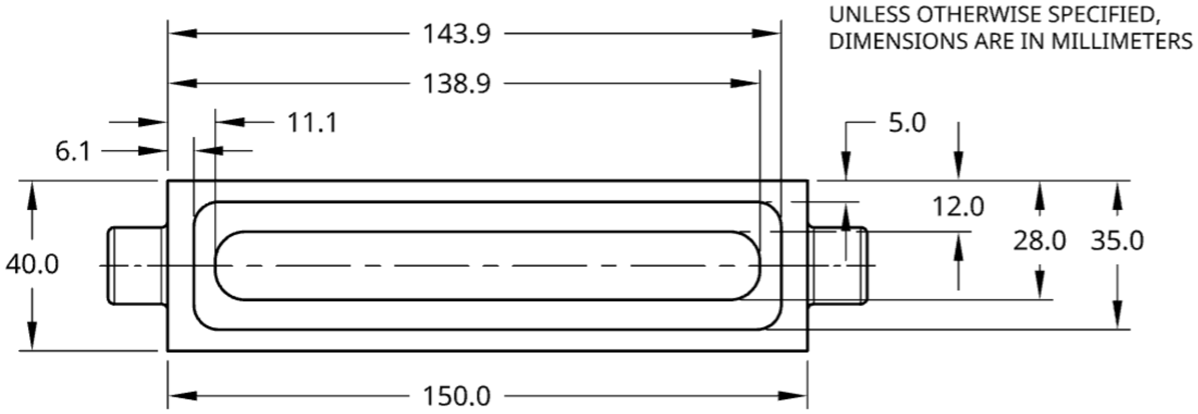

Figure 7.3: Channel quotation.

The following choices were made:

- The heat is mostly concentrated in an area equal to that of the ceramic tile. There is no need of wide channel cross section to spread out the heat in transverse direction.
- Moreover the cross section ratio between inlet/outlet and cooling channel must not be elevated. It leads to a high pressure drop value.

The following magnitudes are obtained.

Cross section inlet/outlet port	Cross section cooling channel	Area ratio ($A_{channel}/A_{inlet}$)
132,7 mm^2	251,2 mm^2	1,89

Being a preliminary 3D model, the channel is modelled as straight neglecting, for the moment, that the cold plate will be mounted radially and the flow will be redirected downwards towards the motor cooling jacket. Moreover the cold plate is just presented as an aluminium sheet placed above the cooling channel.

From the mechanical point of view it lacks several details such as mounting screws, housing for gasket ring etc. However the goal is both to provide a simplified model suitable to be meshed when switching to CFD analysis and to keep the focus on the interaction between fluid and cold plate rather than the structure itself.

When approaching CFD analysis the main objective is to keep unchanged the fundamental geometrical features affecting the simulation results, while simplifying the other features as far as possible.
On the same line the Mosfet geometry must be simplified w.r.t the original one.
Mosfet presents complex shape, corners, curves and several different layers interfaces. This would lead to the need of a really fine mesh that would end up in a bad quality mesh anyway (high skewness and non orthogonality). "A thermal resistance network can be used to approximate the effect of heat sources and heat transfer from that source to the surrounding

domain without explicitly having to resolve the source geometry itself [35]".

Basically, the Mosfet geometry is replaced in the following way, leveraging the **thermal resistance network SimScale command**.

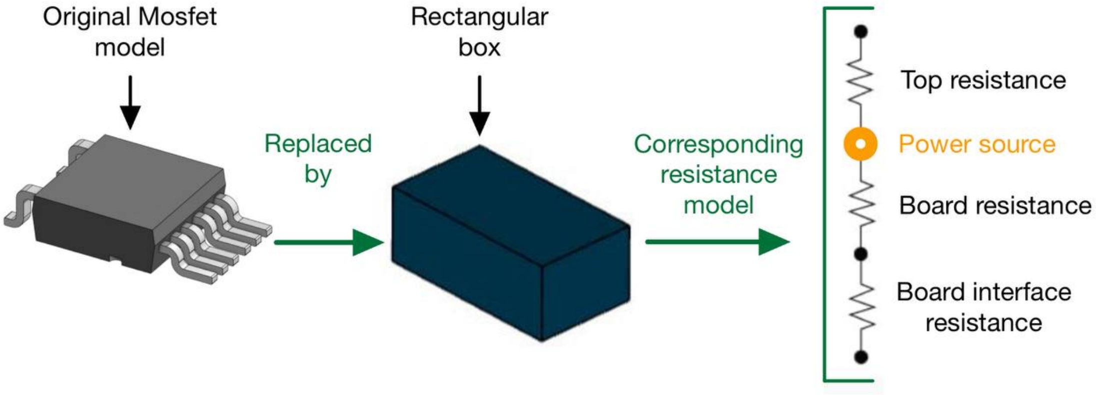

Figure 7.4: Mosfet thermal modelling simplification.

The Mosfet results in a rectangular box with adiabatic walls on the side faces. While the top resistance and board resistance are equal to the junction to case resistance found in Mosfet data sheets.

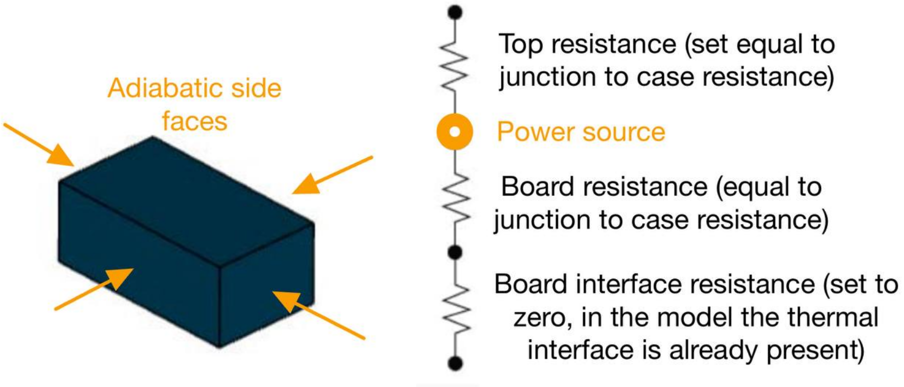

Figure 7.5: Mosfet thermal model, resistance network

Once the 3D model is set, we can move on to the simulation step. The initial design phase conducted in section 6.4, relied on analytical estimations using simplified 1D thermal models. These models are useful for quick assessments and provide a solid starting point for sizing and performance expectations.
However, they inherently overlook important three-dimensional effects such as:

- Uneven heat spreading.
- Local fluid dynamics.
- The influence of geometric constraints that can significantly impact real-world thermal behaviour.

To capture these complexities **Simscale software**, a cloud-based simulation platform, is used to conduct a series of 3D conjugate heat transfer simulations. These simulations offer a more detailed and realistic picture of how heat dissipates through the cold plate and interacts with the fluid flow, revealing key discrepancies between the predictions of the 1D model and the actual thermal performance in three dimensions.

Before moving on to iterative design and optimization, a set of initial exploratory simulations was carried out. This early phase had one main objective: to understand how the assumptions of the 1D model hold up when tested in a more realistic, three-dimensional environment. The insights gained from this preliminary analysis helped inform the next steps of the design process and provided a clearer direction for improving the cold plate's thermal performance.

The following section outlines the setup and results of these initial simulations. In order to run the simulation the following boundary constraints were provided.

Boundary condition	**Value**
Fluid	Water Glycol 50-50%
Inlet volume flow rate	10 L/min
Outlet Gauge pressure	0 Pa
Absolute heat power to be dissipated from the FET	100 W
Air temperature upper convection volume (see Figure 7.6)	100 °C
Flow volume walls	No-slip condition
Remaining walls	Adiabatic
Materials and layers thicknesses	Table 6.5

Table 7.3: Simulation boundary conditions

The upper convection volume constraint results from the inverter PCB to be placed inside a case. In operating conditions, the air trapped inside the case heats up to 100 °C while exchanging the heat generated by the Mosfet. To maintain a constant pressure inside the case a breather hole is present.

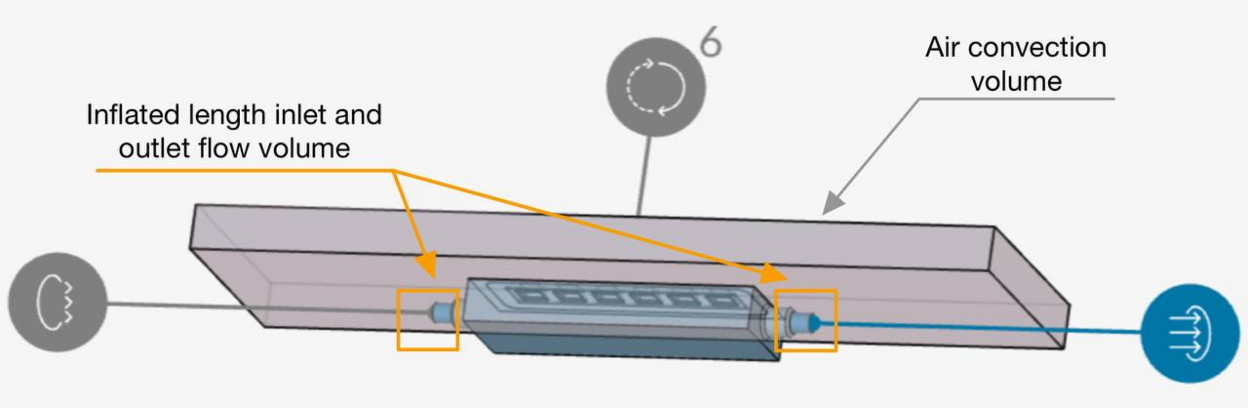

Figure 7.6: Initial model simulation setup.

Moreover the flow volume was lengthened in correspondence of the inlet and outlet port, it provides more stability during simulation preventing from noisy results.

Before getting reliable results in terms of mesh quality, parameters convergence, stability of the results and residuals, several simulations have been run. The setting found to be adequate (even though extremely variable fro case to case) are respectively:

Simulation setting	**Value**
Mesh fineness	6.5/10 ($\approx$ 1.7 Million cells)
Number of iterations	5000

Table 7.4: CFD simulation mesh and iteration settings.

The mesh quality obtained.

Mesh quality, parameter	**Value**
Non orthogonality	$\leq$ 70 (below the threshold of 80)
Skewness	$\leq$ 2.67 (below the threshold of 10)

Table 7.5: Mesh quality metrics.

In terms of parameters residuals (Figure 7.7, the values obtained are satisfactory (around 10^-3 or lower). Moreover all of them show good behaviour in terms of steadiness and convergence.

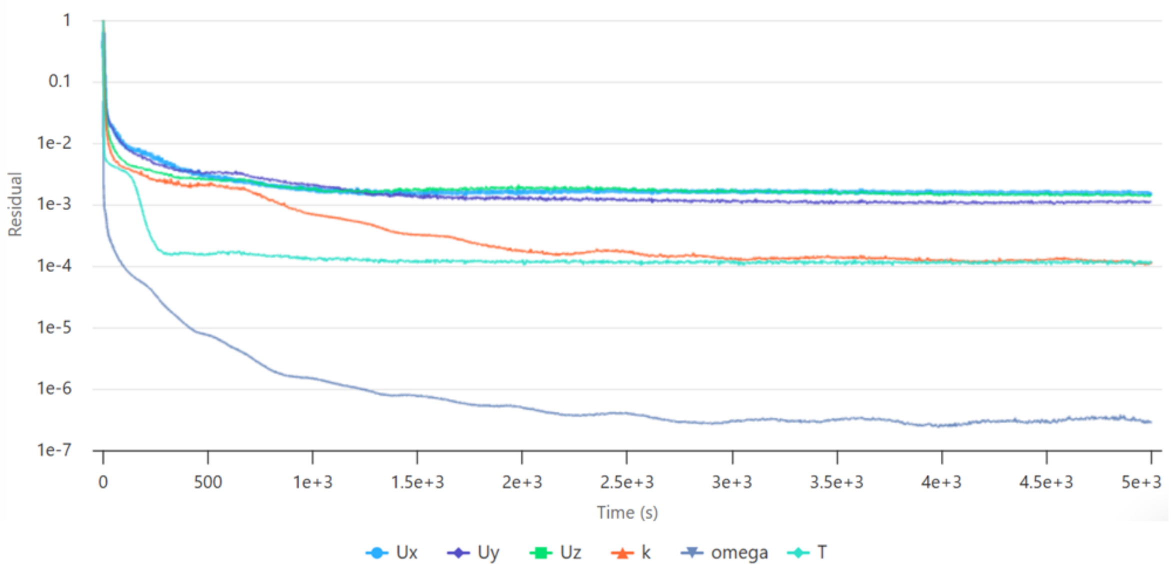

Figure 7.7: Initial model, simulation residuals.

The first result we are interested in are junction temperatures.
From the 1D model the expected maximum Tj was equal to 150°C. From simulation the obtained temperatures distance themselves from this value up to 39°C in value.

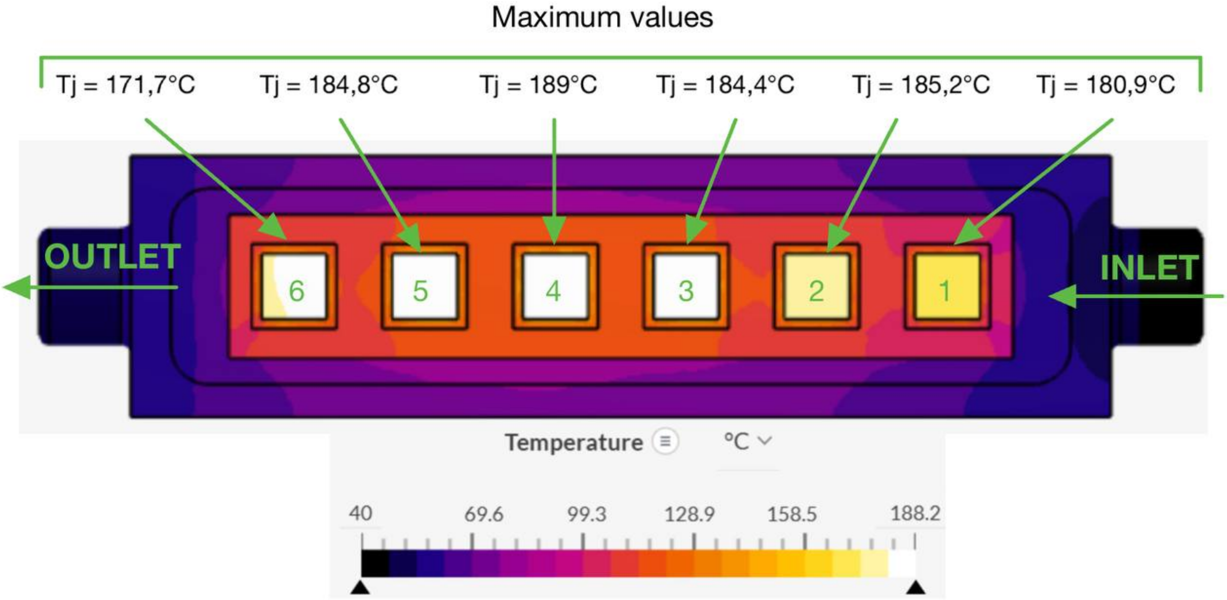

Figure 7.8: Maximum junction temperatures.

A T_j peak of 189°C is reached.
Looking at velocities, the fluid flow is pretty uniform throughout the channel apart from inlet and outlet ports. In these two regions turbulence rises because of the cross section change.

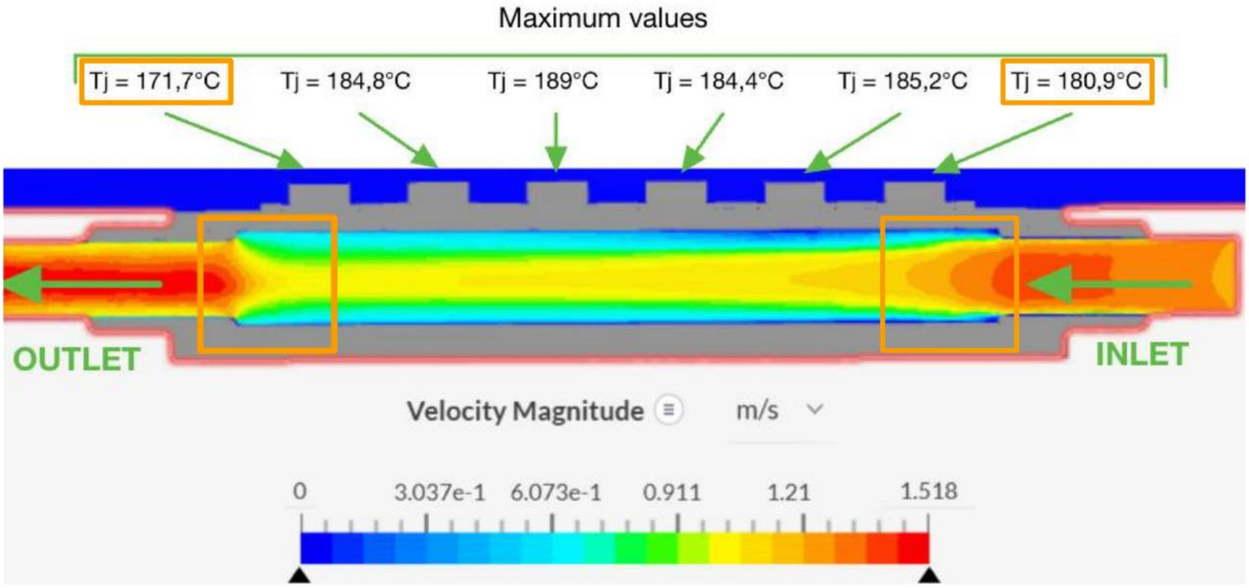

Figure 7.9: Fluid velocity magnitude.

The increased turbulence is reflected on T_j of MOSFETs positioned in correspondence of inlet/outlet port. The display lower temperatures compared to other MOSFETs in line.

In terms of pressure drop the data obtained are summarized in the following table.

Inlet relative pressure	Outlet relative pressure	Final ΔP
1066,9 Pa	389,3 Pa	677,6 Pa

REMARK: The temperature values obtained through simulation remarkably distance themselves from the temperature profile obtained from the 1D thermal model. The reasons for this can be found in the following factors:

- Finally some additional degrees result from an uneven spreading of the heat. The heat tends to be more concentrated at the centre of Mosfet surface, the temperature gradient inside the material volume is lower compared to the one at the edges.

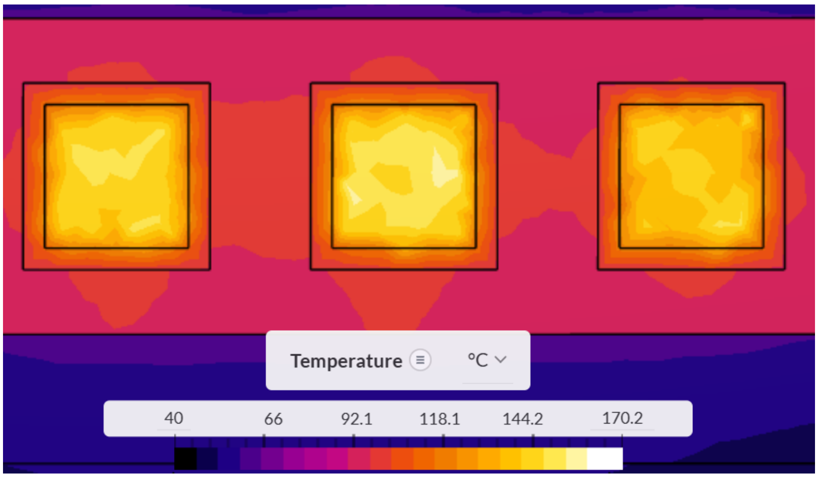

Figure 7.10: View of heat distribution under Mosfets.

This results in a pick junction temperature at the central point of the MOSFET.

- The 1D thermal model did not account for the additional convective thermal resistance between the fluid and the cold plate. Part of the observed temperature increase can be attributed to this effect.

The discussion didn't take into account the temperature variation of the fluid because negligible.

Average inlet fluid T	Average outlet fluid T	Comment
40°C	40.9°C	The low ΔT is justified from the high water c_p value. $c_p = 4189$ J/(Kg*K) at ambient temperature.

The sudden change in cross section affects the fluid velocity profile and, as a consequence, pressure values.

7.2 Pins cold plate geometries

Based on previous results it's clear how, in order to reach the target T_j, it's necessary to enhance convection heat transfer. To enhance flow turbulence, pins must be integrated in the cold plate geometry.

The analysis focused exclusively on:

- Circular pins.
- Elliptical pins

This choice was driven by the company's established expertise with these geometries, as well as by specific design guidelines intended to ensure compliance with internal standards and ease integration into existing manufacturing processes.

Instead of directly analysing the fluid behaviour through the lens of simulation, a graphical approach is leveraged. Thanks to physical laws of fluid dynamics and critical thinking, a qualitative comparison between the two geometries is obtained.

- Inline circular: it features an array of vertically oriented, circular cross-section pins arranged in a regular grid within the flow channel. Coolant flows over pins in a direction aligned with the inlet and outlet.

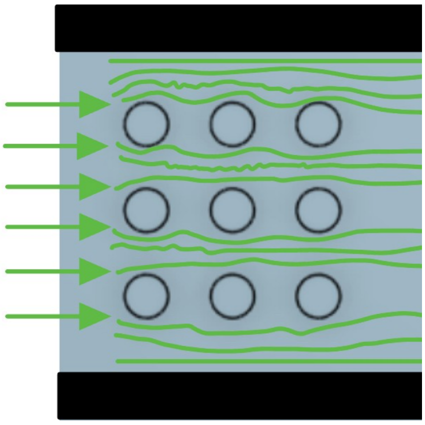

Figure 7.11: Inline circular cold plate pins, graphical approach. On the left the inlet port of the fluid.

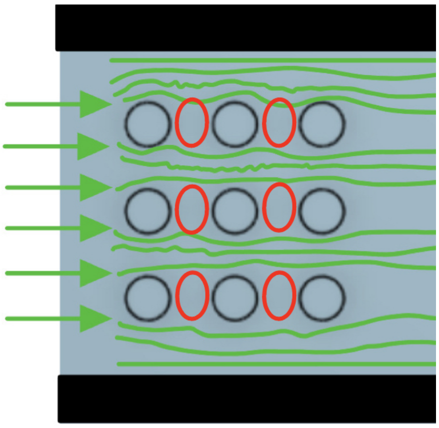

Figure 7.12: Inline circular cold plate pins, graphical approach. Circled in red the regions lacking fluid touch.

In Figures 7.11 and 7.12, where the green arrows indicate the direction of the fluid, it is possible to see how the fluid skims the lateral regions of pins but leaves the back areas of the pins untouched (red ellipses in Figure 7.12). This leads to a reduction of the contact surface area between fluid and plate, reducing the capability of heat transfer. On the other side circular pins allow to obtain turbulence without diverging to much the direction of the fluid, limiting pressure drop.

- Staggered circular pins: To allow the fluid penetrate more easily the pin patterns, staggered configuration is the answer.

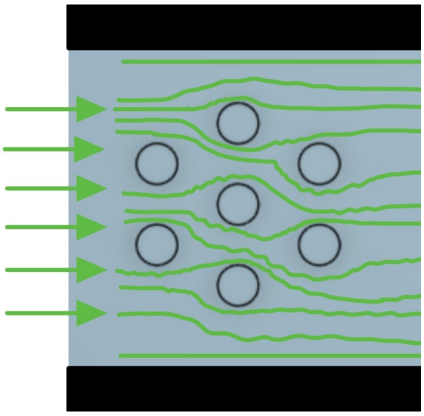

Figure 7.13: Staggered circular pin, graphical approach

Staggered pin-fin are arranged so each row is offset, placing the pins in the gaps between the pins of the previous row. This layout forces the coolant to move around the pins in a zigzag path, which increases turbulence and mixing in the flow. This extra movement helps to break up the thermal boundary layer, leading to a higher heat transfer rate. Because of this, staggered pin-fin designs can remove heat more effectively than inline arrangements. However, the increased flow resistance also causes a higher pressure drop compared to inline configuration.

- Staggered elliptic pins and elliptic fins: In case of pins, to further increase the contact surface area elliptic shape can be leveraged.

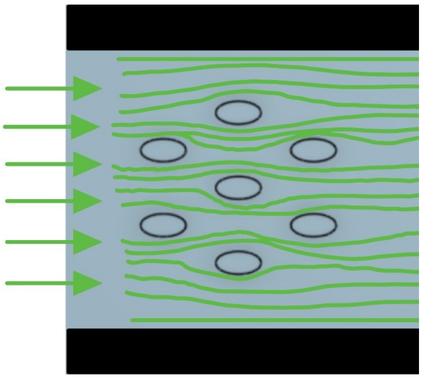

Figure 7.14: Staggered elliptic pins, graphical approach.

Because of its more aerodynamic shape (compared to the circular one), the fluid flow exhibits improved adherence along the surface, resulting in greater surface coverage and smaller wake region (pressure drop). This enhances convective heat transfer efficiency by maximizing the interaction between the flow and the solid boundary. The effect is clearly illustrated in the figure 7.14.

Based on the considerations done, the following comparison table is drafted.

Geometry type	dP (pressure drop)	Re (reynold number)	Mass flow rate (Kg/s)
Inline circular	🔴	🔴	🟢
Staggered circular	🟠	🔴	🟠
Staggered elliptical	🟢	🟠	🔴

Table 7.6: Qualitative, pin geometry comparison based on strategic parameters.

🔴	Higher
🟠	Medium
🟢	Lower

Legend of Table 7.6

The results displayed are backed and validated by **Garrett Motion experience** in the field.

7.3 Elliptical pins cold plate

Since the thesis focuses on comparing liquid cooling with refrigerant-based (gaseous) cooling, the design of the cold plate pins must be suitable for both approaches. Adopting the same pin geometry for each configuration ensures a fair and consistent comparison between the different cooling solutions, effectively eliminating the influence of cold plate pin design as a variable in the analysis. **The chosen pin geometry is staggered elliptical pins.**

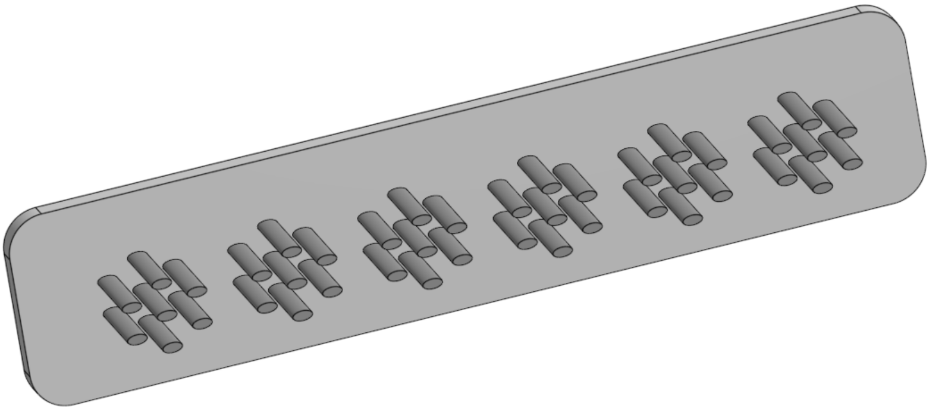

Figure 7.15: Staggered elliptical pin cold plate.

Indeed gases, due to their significantly lower density, more readily transition to turbulent flow. Consequently, a smoother pin geometry such as elliptical is more suitable and feasible for both cooling approaches.

The overall channel geometry is identical to that shown in Figure 7.3 and will therefore not be repeated here. Instead, a section and an exploded view of the new configuration are provided first. The focus will then shift to the elliptical pins, with details on their dimensions and placement.

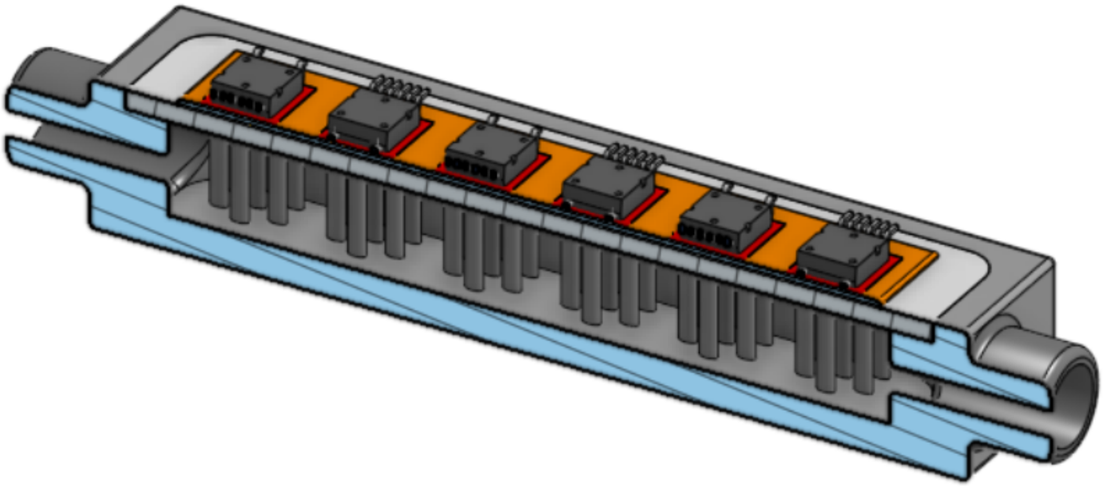

Figure 7.16: Section view, elliptical pins.

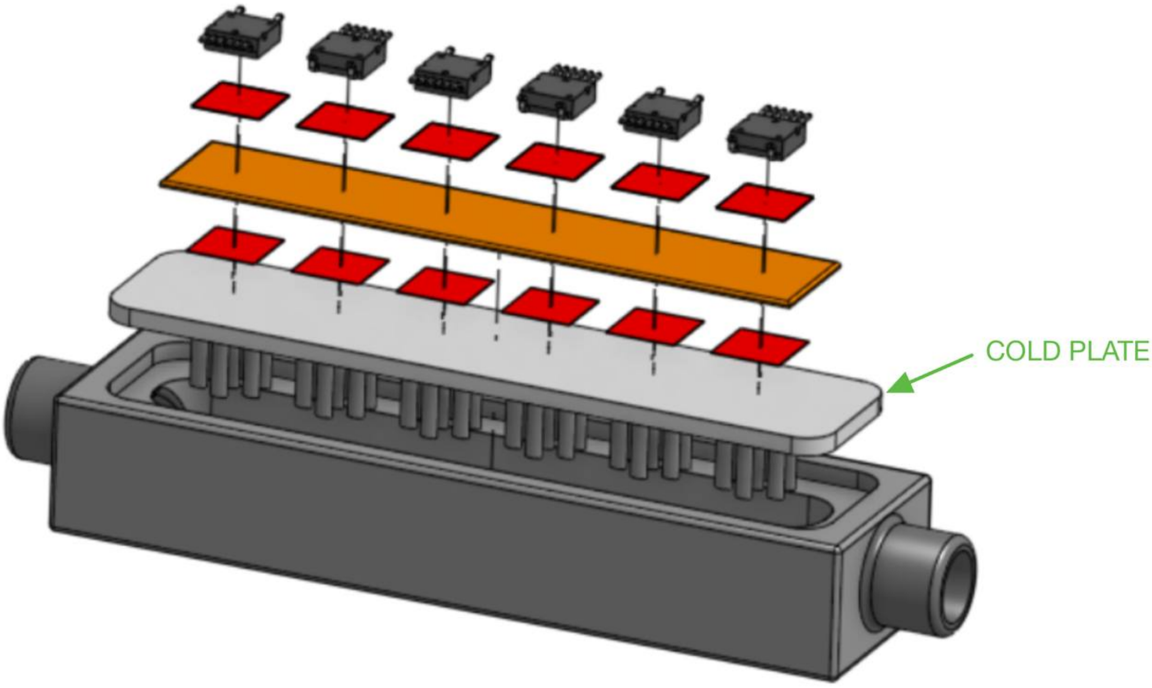

Figure 7.17: Exploded view, elliptical pins

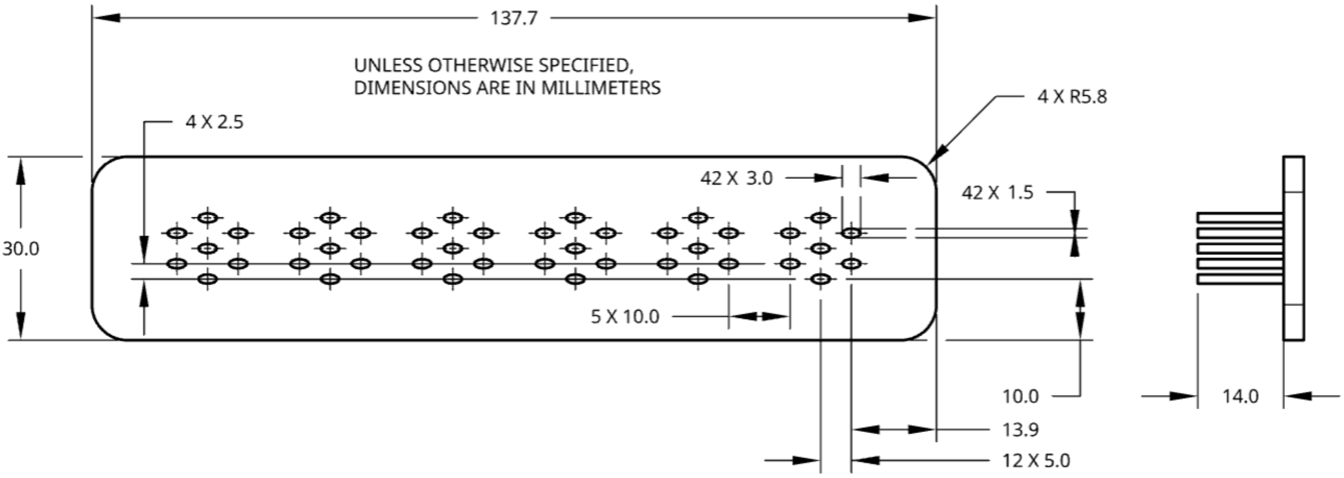

Figure 7.18: Cold plate pins quotation

Due to the increased complexity of the geometry, the meshing process presented some challenges, requiring parameter adjustments to ensure an adequate mesh quality. The primary issue was the presence of high non-orthogonality values near the pins and in the air gaps between the ceramic tile and the cold plate (which are separated by a 0.1 mm layer of thermal grease). The following adjustments were made to address these issues.

Simulation setting	**Value**	**Comment**
Overall mesh fineness, unless otherwise specified	5/10	Decreased from 6.5 → 5 to allow higher finesse in other specified regions.
Flow regions (both the air and fluid volume) mesh finesse	7/10	Increased mesh finesse to obtain proper residuals convergence and detailed fluid behaviour representation.
Inflated boundary layers in fluid regions	6 layers with smooth growth rate equal to 1.2	To better capture the interaction between fluid and solid walls.
Gap growth rate	From 0,05 → 0.2	It ensures lower flattening of cells, preventing from too high non orthogonality values.
Mesh cells number	13.5 Million	From 1.7 Million of previous meshing, increased of 8 times. Much higher computational time required.

Table 7.7: CFD simulation mesh settings changes.

Mesh quality, parameter	**Value**	**Comment**
Non orthogonality	Below the threshold of 80	Just a couple of cells exceed this value reaching 84. However they are not placed in strategic regions, ensuring proper results.
Skewness	$\leq$ 3.2 (below the threshold of 10)	The increase is so little that has non influence.

Table 7.8: Mesh quality metrics.

Parameter	**Value**	**Comment**
Boundary conditions	Table 7.3	Same boundary conditions were applied

Table 7.9: Boundary conditions

Once the simulation was run the following residuals were obtained. As further proof of good convergence, the residuals of relative pressure are added to the plot.

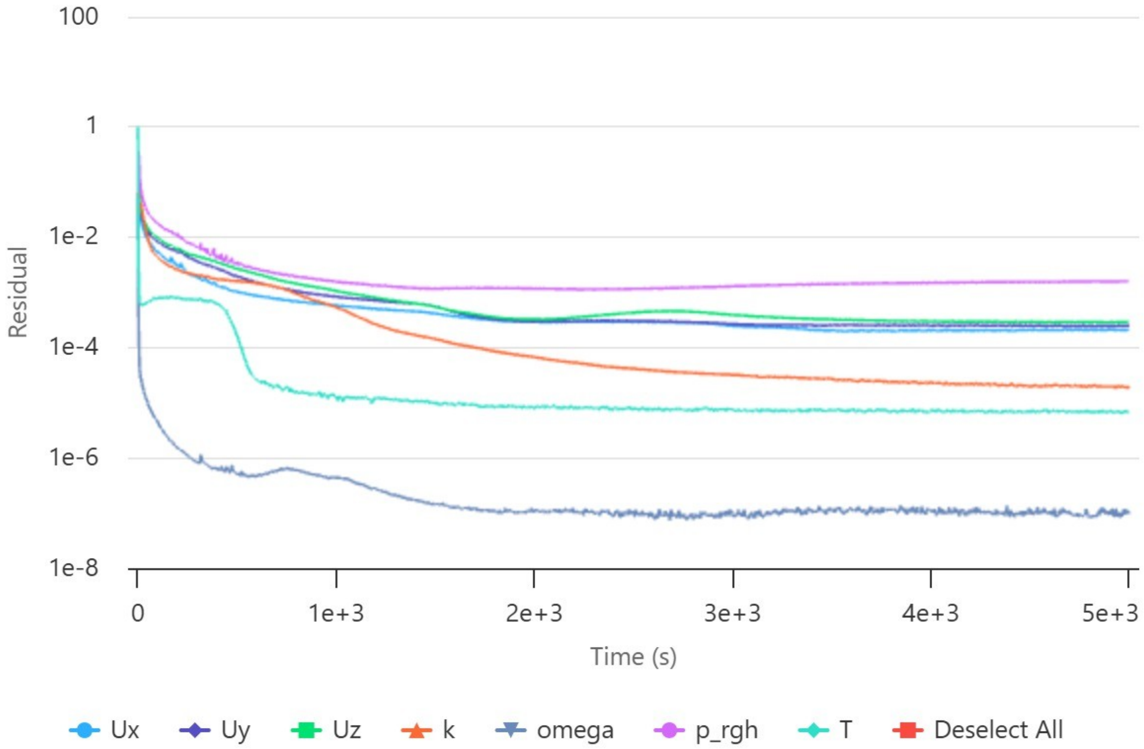

Figure 7.19: Simulation residuals

The highest residual value is equal to $1.59{\cdot}10^{-3}$, still acceptable value.

The addition of pins must serve the purposes cited in previous paragraph: increased turbulence ⇒ higher Nu ⇒ higher h ⇒ lower T_j. The resulting junction temperatures validate the reasoning.

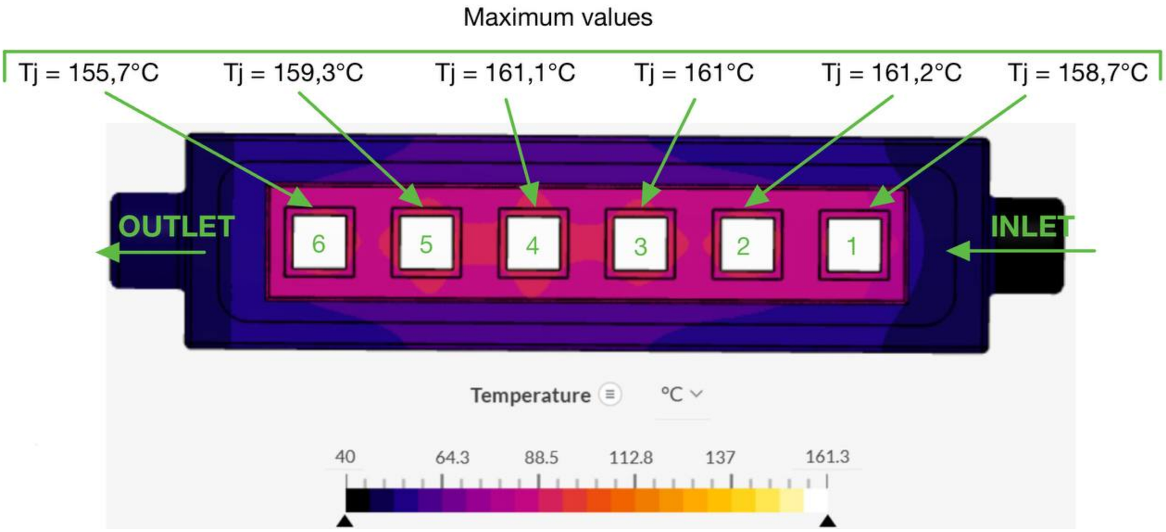

Figure 7.20: Maximum junction temperatures.

Many observations can be done looking at T_j:

- An overall reduction in Mosfet junction temperatures is observed.
  The convection heat transfer is increased at a point that on Mosfet 4 a significant temperature drop is observed (compared to the same cold plate without pins, Figure 7.8).

Mosfet 4 T_j, cold plate without pins	Mosfet 4 T_j, cold plate with elliptical pins	Temperature drop ΔT
189 °C	161,1 °C	27,9 °C

- The T_j display a much more constant behavior through the Mosfets. This results in a better temperature distributions on the different layers with a benefit on mechanical deformations and stresses.
- The maximum T_j is still 11,1°C higher than the project $T_j = 150$°C.

The displayed T values are related to fluid behaviour, the analysis is directly tackled in the next paragraph.

Remarks when analysing fluid velocity magnitudes:

- The pins locally reduce the cross section, leading to a local increase in fluid velocity positively influencing convection and negatively affecting pressure drop.
- The inlet region benefits still from higher velocity because of its proximity with the inlet port.

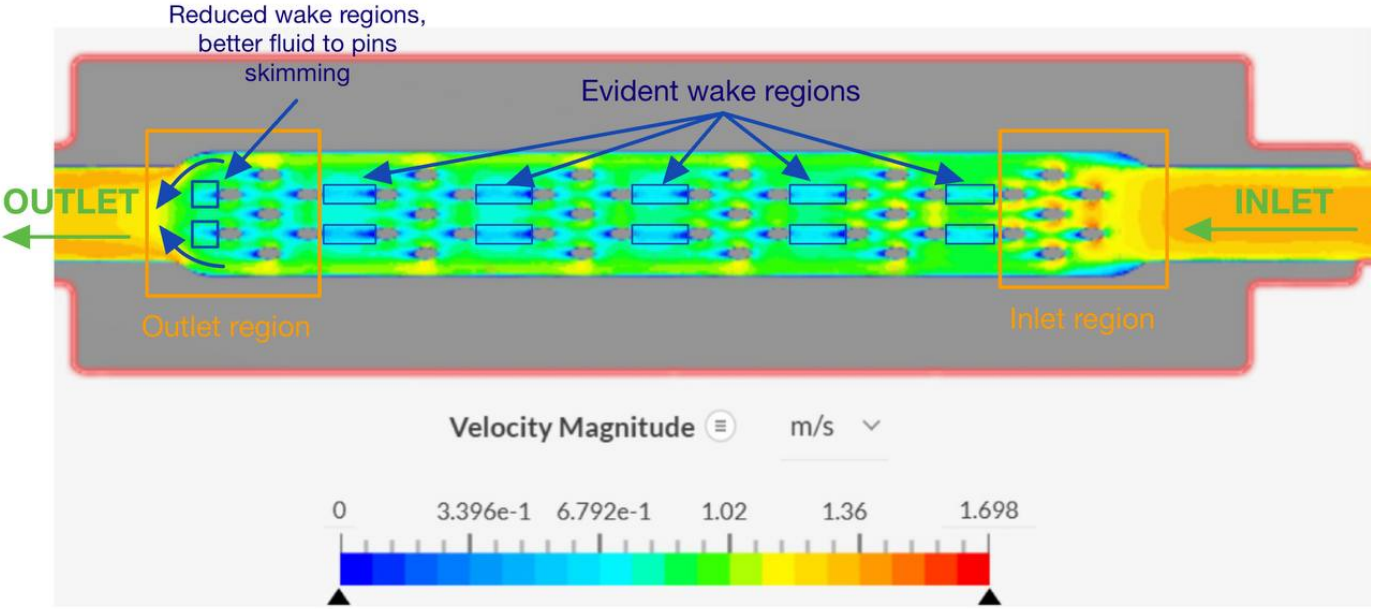

Figure 7.21: Fluid velocity magnitude.

- Evident wake regions are present in correspondence of the last pins rows. It results in less effective heat transfer.

- In the outlet region the fluid is redirected towards the centre when transitioning from the channel to the outlet port. This reduces the wake regions around the last pins → better heat transfer → lower T_j.

However the addition of pins comes with a trade-off in terms of pressure drop. See Figure 7.22.

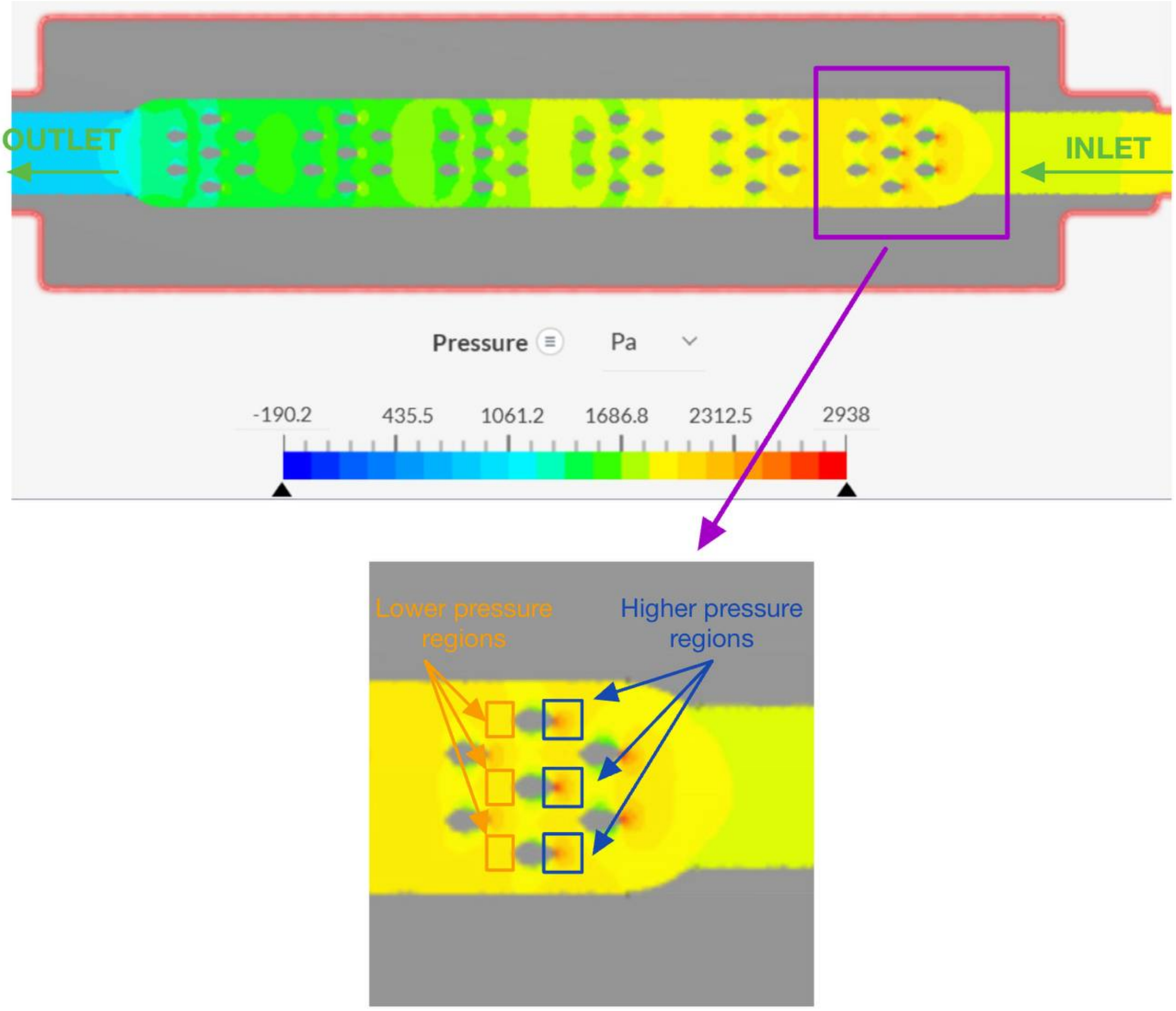

Figure 7.22: Fluid pressure values

When hitting the pins, the fluid exhibits high pressure values that decrease when reaching the back of the pin. This high pressure region in the front and low pressure region in the back comes from the drag force applied by the pins against the fluid flow.

Drag force against the fluid ⇒ kinetic energy loss ⇒ Pressure drop increase.

Inlet relative pressure	Outlet relative pressure	Final ΔP
2096,4 Pa	389,3 Pa	1707,1 Pa

Finally a look at the pin section must be taken. In Figure 7.23, the section of central pins in correspondence of Mosfet 2 is pictured.

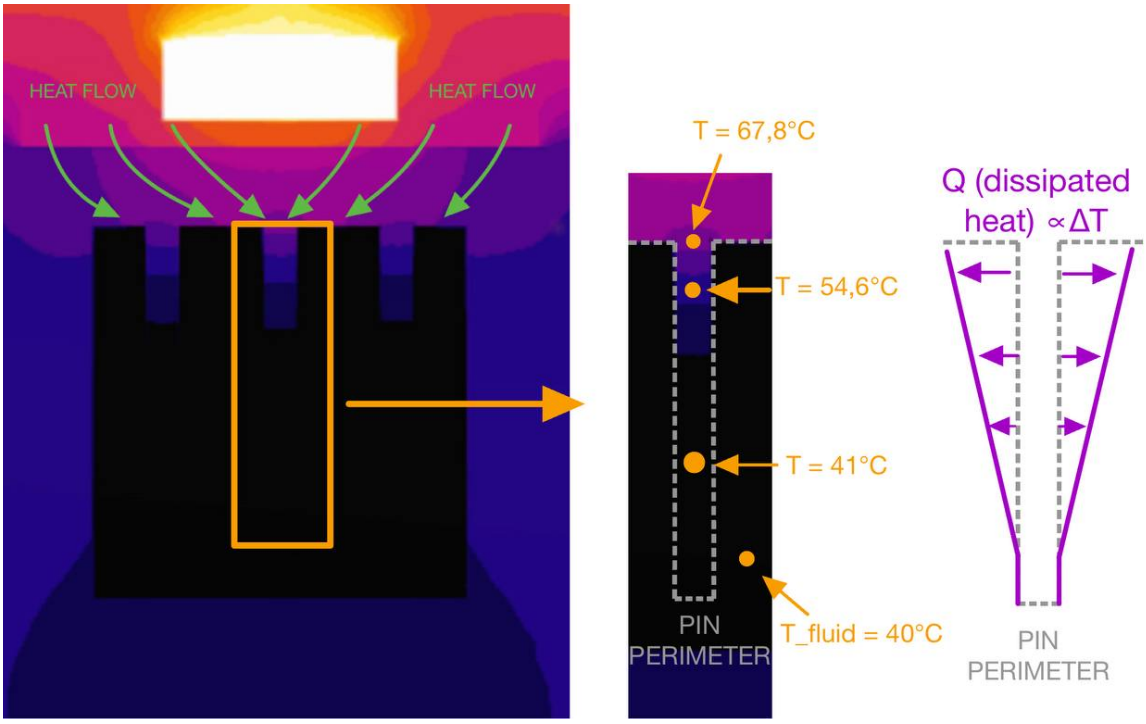

Figure 7.23: Flow region section, central pin temperature profile at Mosfet number 2.

Two remarks can be done:

- The heat flow, as already mentioned, tends to converge towards the centre of the section. Central pins tends to dissipate more heat per unit area.
- The driving force of heat dissipation is the ΔT. However when looking at the temperature profile of the pins, just the higher part exhibits temperature higher than 40 °C (that of the fluid). This means that the bottom part of the pins almost displays no heat exchange Q. The height of the pins could be slightly reduced in order to decrease pressure drop.

The issues to be faced are two: T_j reduction while satisfying feasible pressure drop values. The following approaches could be studied:

- Volume flow rate increase. From both a simulation point of view it's the easiest approach, no change in the geometry.
- Wake regions reduction through channel geometry improvement. In order to ensure a proper velocity profile tighter to the pin.
- If the previous paths are not enough, a pin geometry change or a different arrangement can be taken into consideration.

7.4 Flow rate increase

As suggested in the previous points, the first approach was the analysis of the flow rate increase effect.

The expected benefits are:

- Better heat absorption and removal from the surface. The higher coolant mass per second and steeper velocity profile gradient ensure an improved heat transfer coefficient (on a theoretical level, at least).
- It can help eliminating hot spots ensuring a more uniform temperature distribution.

Whereas when shifting to the flaws:

- A flow rate increase can significantly rise the pressure drop. It is proportional to the square of the flow rate, in the specific for a circular pipe:

  $$\Delta P = f \cdot L \cdot \frac{8\rho Q^2}{\pi^2 D^5} \tag{7.1}$$

  where:

  - ΔP is the pressure drop (Pa),
  - f is the Darcy friction factor (dimensionless),
  - L is the length of the pipe (m),
  - D is the internal diameter of the pipe (m),
  - ρ is the fluid density (kg/m^3),
  - Q is the volumetric flow rate (m^3/s).
- After a certain point the benefit of flow rate increase reaches a ***saturation point***. Beyond a certain value, the thermal benefit is not outweighed anymore by the pressure loss increase.
- High velocity through narrow channels can lead to surface erosion and vibrations.

Case study	Volume flow rate	Maximum T_j reached	Pressure drop dP	Pressure drop increase (w.r.t case 1)	Maximum T_j decrease (w.r.t case 1)
1	10 L/min	161.2°C	1707.1 Pa	—	—
2	11 L/min	155.8°C	2167 Pa	≈ 27.9%	≈ 3.3%
3	12,5 L/min	154.4°C	2672 Pa	≈ 56.5%	≈ 4.2%

Table 7.10: Comparison of case studies based on volume flow rate, maximum junction temperature and pressure drop.

As visible from Table 7.10, the volume flow rate increase doesn't have influence. A considerable pressure drop increase is witnessed, while the Maximum T_j reached is just partially affected. To justify the reasons behind the observed phenomenon, a zoom on the interaction between pins and flow is considered.

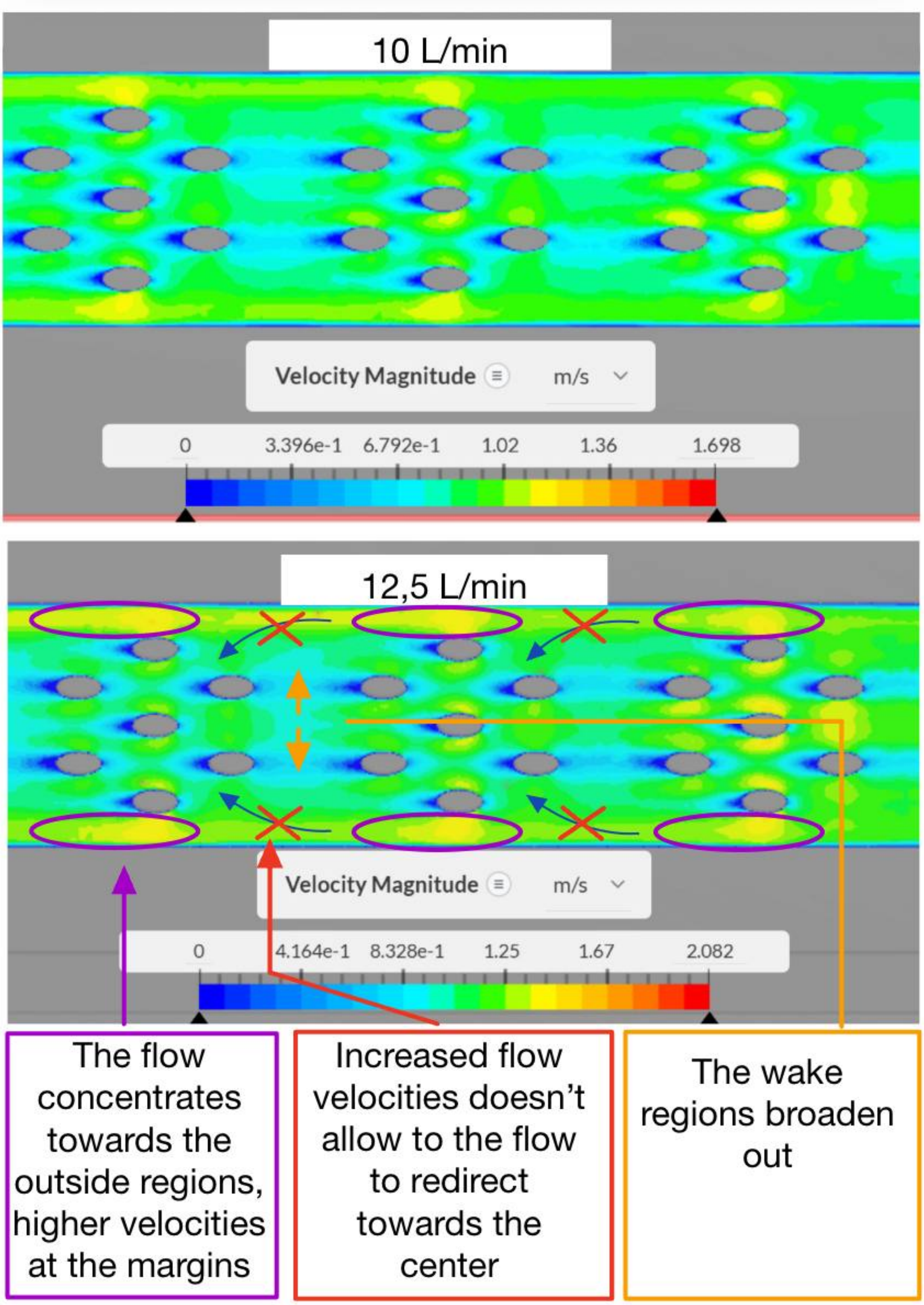

Figure 7.24: Flow rate increase comparison, same geometry.

In Figure 7.24 the considerations are already specified, in the following bulleted list they are discussed in more detail.

- The flow tends to concentrate near the outer regions of the channel, resulting in higher local velocities along the edges. However, since the majority of heat generation is concentrated near the centre of the channel, the increased peripheral velocities do not contribute to overall heat dissipation.
- In addition to the flow shifting towards the channel edges, the elevated velocities promote a straight flow behaviour, causing the fluid to bypass central regions of the channel. This leads to insufficient mass flow in critical heat-loaded areas, further degrading convective heat transfer performance.
- The existing large wake regions between pin fin arrays tend to grow, exacerbating flow stagnation. These stagnant zones are detrimental not only due to their minimal contribution to convective heat transfer but also because they increase pressure losses, thereby reducing the overall thermal-hydraulic efficiency of the system.

7.5 Final design

A key point for the design development is now outlined. At 12,5L/min in volume flow rate the nature of the pressure drop origin is much more evident.

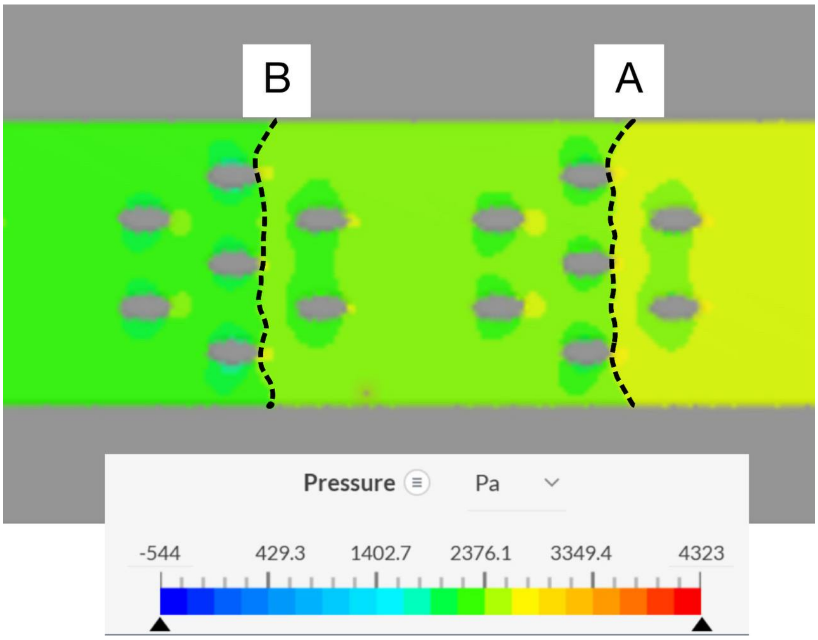

Figure 7.25: Interfaces of main pressure drop.

Taking the central part of the channel as reference, the biggest changes in terms of pressure happen in correspondence of the positions named as "A" and "B". In both of them the fluid experience a cross section change, due to the different number of pins.

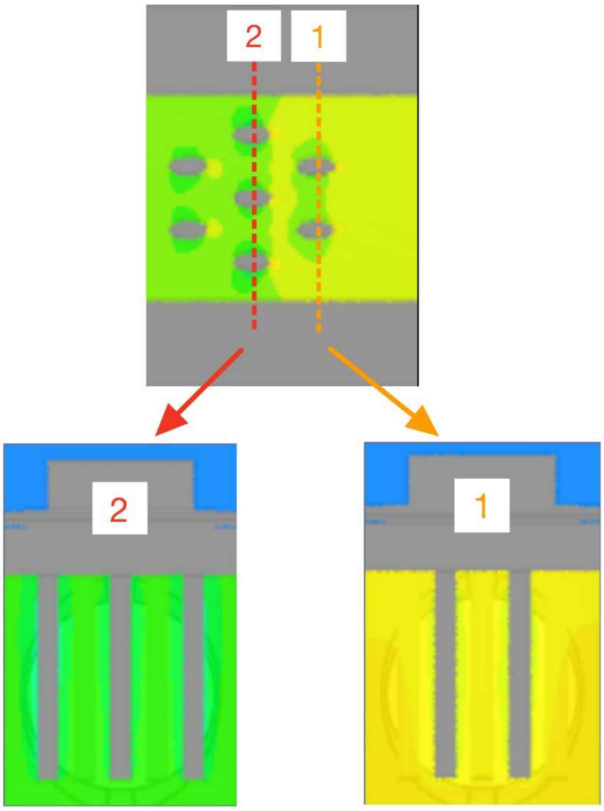

Figure 7.26: Cross section change due to different number of pins.

Indeed it can be stated that:

$$A_1 = A_{\text{channel}} - (2 \cdot A_{\text{pins}})$$

$$A_2 = A_{\text{channel}} - (3 \cdot A_{\text{pins}})$$

The channel wall shape can be modified in order to keep the cross section constant, so that the fluid will not experience abrupt changes lowering pressure drop.

The following design choices were taken.

Parameter	**Value**	**Comment**
Channel cross section	15,5 x 16 mm^2	A small change on the width has been carried on.
Pins dimension	See Figure 7.18	Kept constant, not a parameter of interest at this stage.
$A_{reference}$	185 mm^2	It indicates the goal cross section area value to keep constant throughout the pin pattern.

Table 7.11: New design choices

The value of the $A_{reference}$ was obtained as follows:

$$A_{reference} = A_{\text{channel}} - (3 \cdot A_{\text{pins}}) = 248 - (3 \cdot 14 \cdot 1,5) = 185mm^2$$

The new design idea is to keep this cross section value throughout the pin pattern by modifying the channel wall. The final goal is to prevent the phenomena pictured in Figure 7.25.

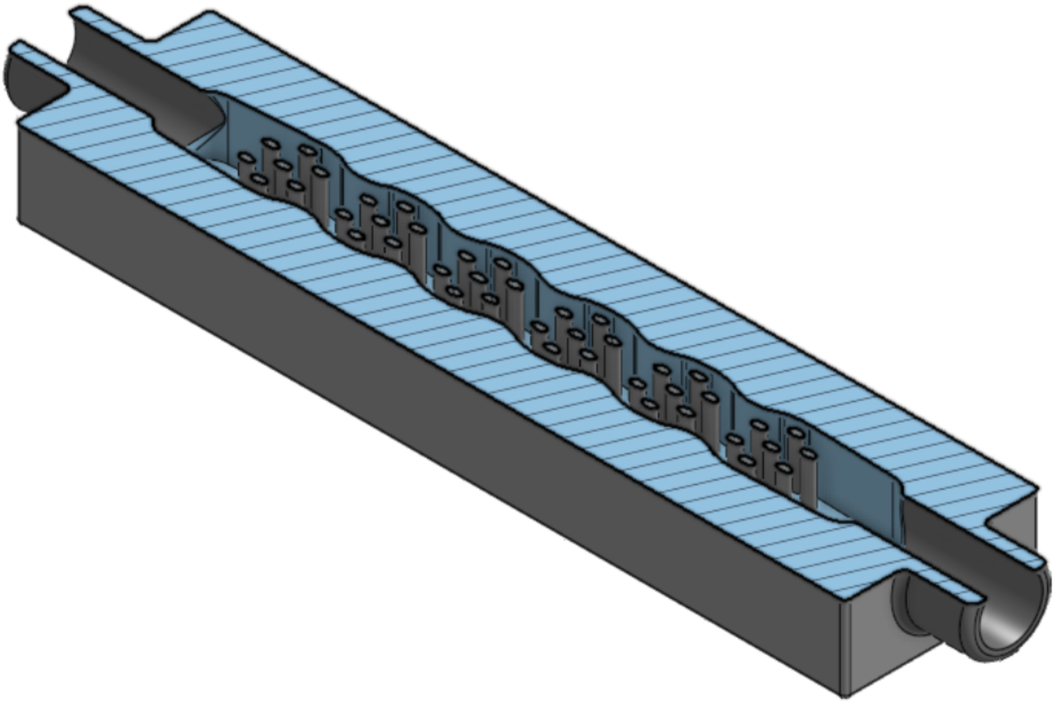

Figure 7.27: Efficient channel design for pressure drop decrease and flow redirection.

The varying wall geometry, well pictured in Figure 7.27, bridges the gaps left by the varying number of pins assuring (almost) constant cross section value throughout the channel.

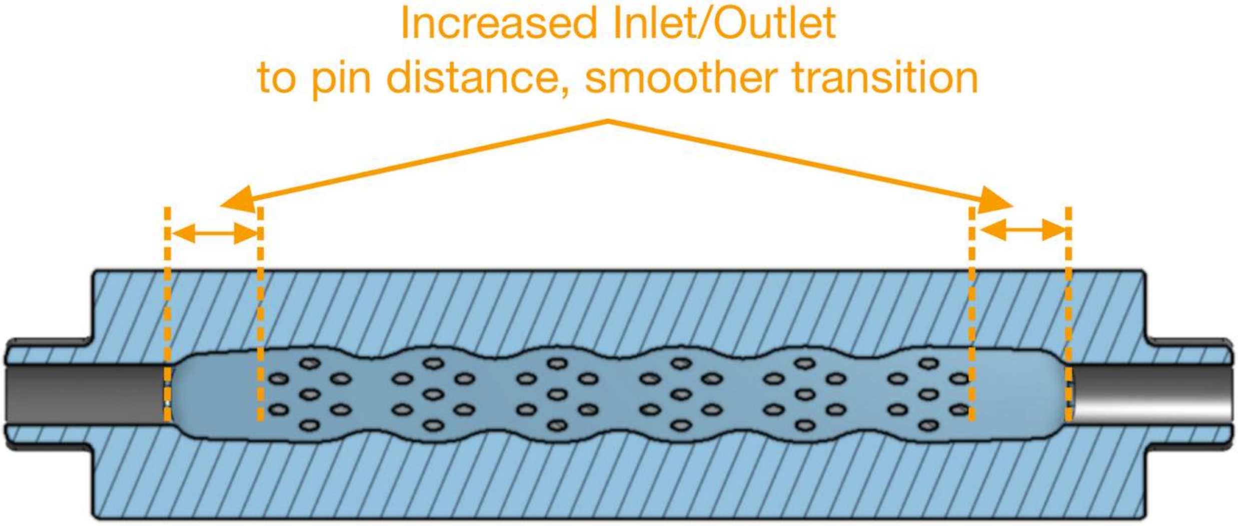

Figure 7.28: Channel cross section. Inlet/Outlet to pin increased distance.

Moreover the Inlet/outlet distance from the pin interface has been increased, to obtain smoother transition and flow uniformity before the contact.

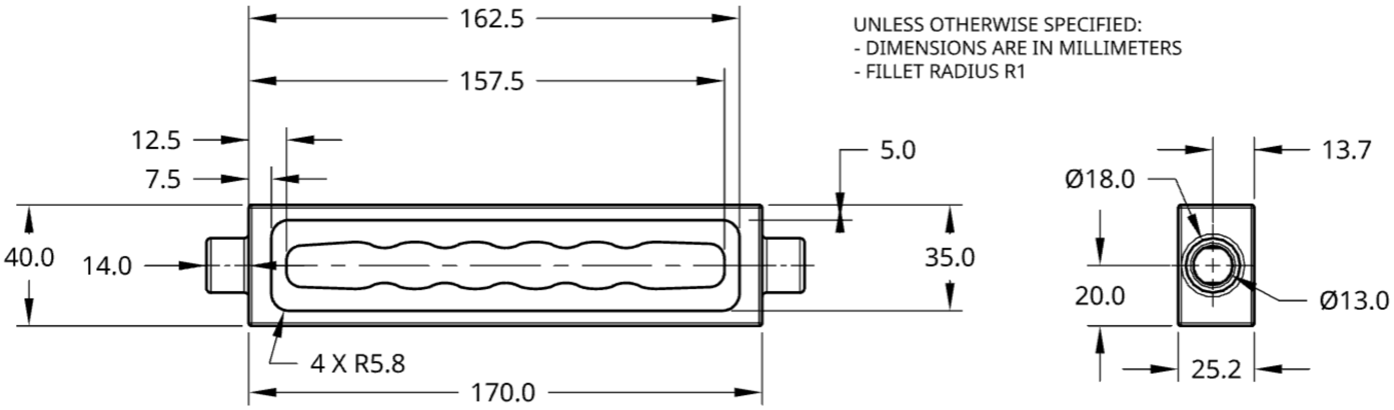

Figure 7.29: Channel quotation.

In the image below, detailed channel dimensions are provided to give the reader a clear reference. However, in real world applications due to the complexity of the geometry only the 3D model is typically supplied. When manufacturing is performed using CNC machining, such detailed dimensional specifications become redundant.

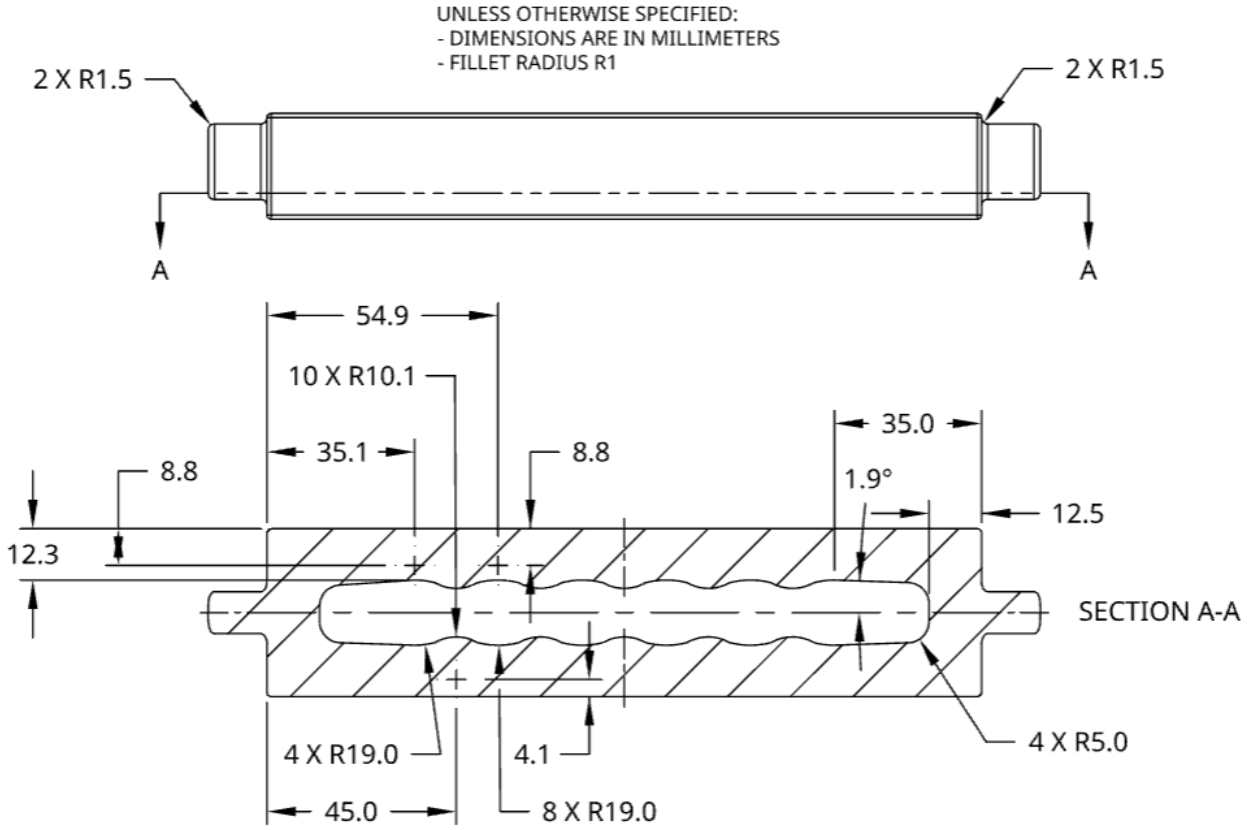

Figure 7.30: Channel quotation.

Once the simulation was run farther adjudgements were taken. Keeping in mind that the final $T_j < 150$ °C, a flow rate of 10L/min allowed for even better performances than the target one. For this reason the flow rate was slightly decreased to 8L/min, value that allowed to hit the target T_j while reducing power consumption and water pump dimension.

Parameter	**Value**	**Comment**
Volume flow rate	8 L/min	Decreased from 10L/min.
Additional boundary conditions	Table 7.3	Except for the flow rate, the boundary conditions are the same as reported in the Table.
Mesh settings	Table 7.7	The same mesh settings were leveraged, proper and uniform mesh obtained.

Table 7.12: Simulation settings

The design is a success under every aspect.

Starting from the T_j. The goal is reached, all Mosfet junction temperatures are kept under the set limit of 150 °C.

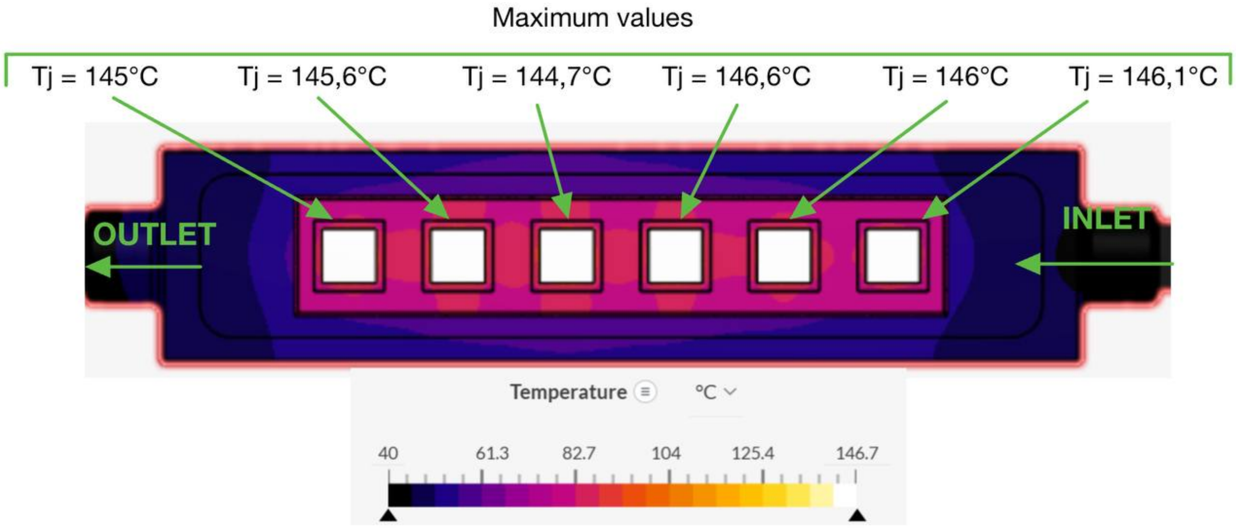

Figure 7.31: Maximum junction temperatures.

Moreover T_j show good uniformity assuring higher uniformity in terms of temperature induced stresses. It's a fundamental topic when brittle materials like the ceramic tile are present in the design.

The reason behind the increased performances lies in the highly efficient behaviour of the flow inside the channel. The new design show fluid velocity uniformity and efficient skimming of pin surfaces.

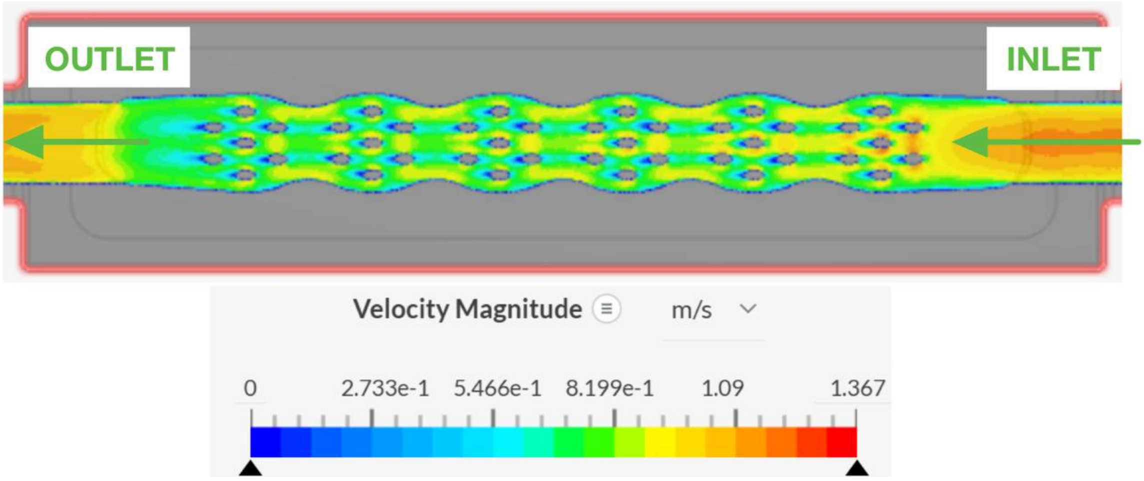

Figure 7.32: Fluid velocity magnitude.

The channel geometry, besides keeping under control pressure drop, redirects the flow towards the central regions.

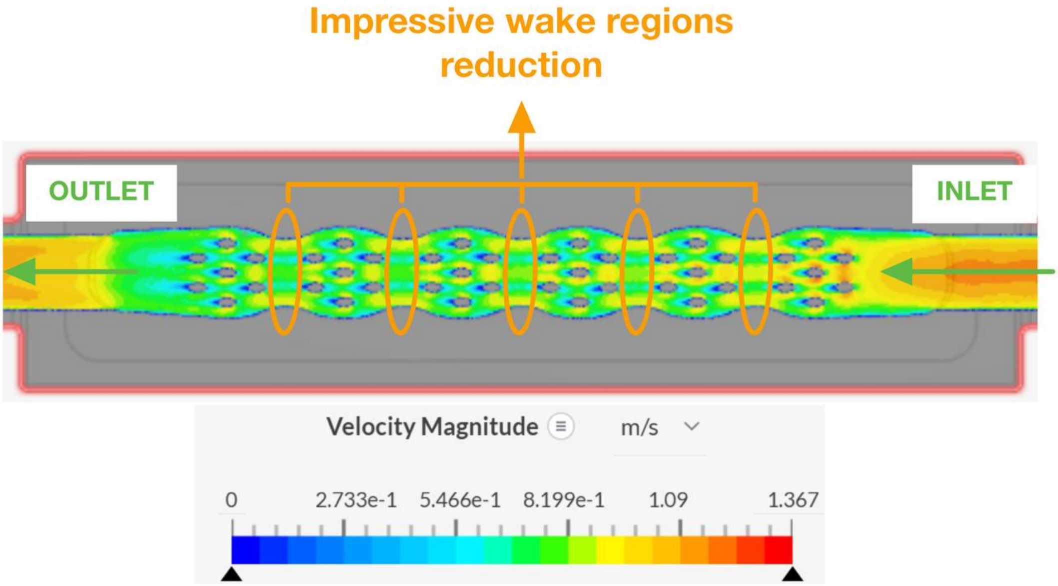

Figure 7.33: Fluid velocity magnitude with highlighted wake regions.

The result shows a remarkable reduction of wake regions, contributing to heat transfer efficiency. Previously the pressure drop was cited, now its entity is reported.

Inlet relative pressure	Outlet relative pressure	Final ΔP
2180,2 Pa	389,3 Pa	1790,3 Pa

Once the design simulation results are provided, an important topic must be recalled. The inverter cold plate is mounted radially w.r.t motor cooling jacket, so a 90 ° bend is expected at the outlet of the channel. The purpose is redirecting the flow towards the electric motor cooling jacket.

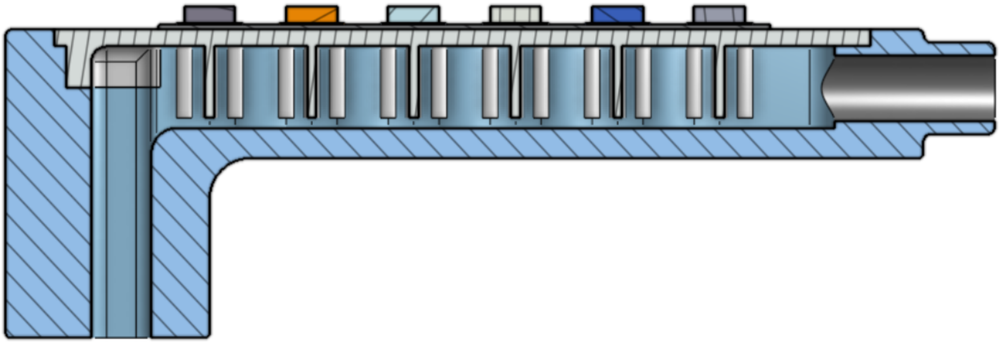

Figure 7.34: Final design lateral cross section. Radial positioning efficient cold plate.

The cross section of the final design is shown in Figures 7.34 and 7.35. The design is now deemed finalized.

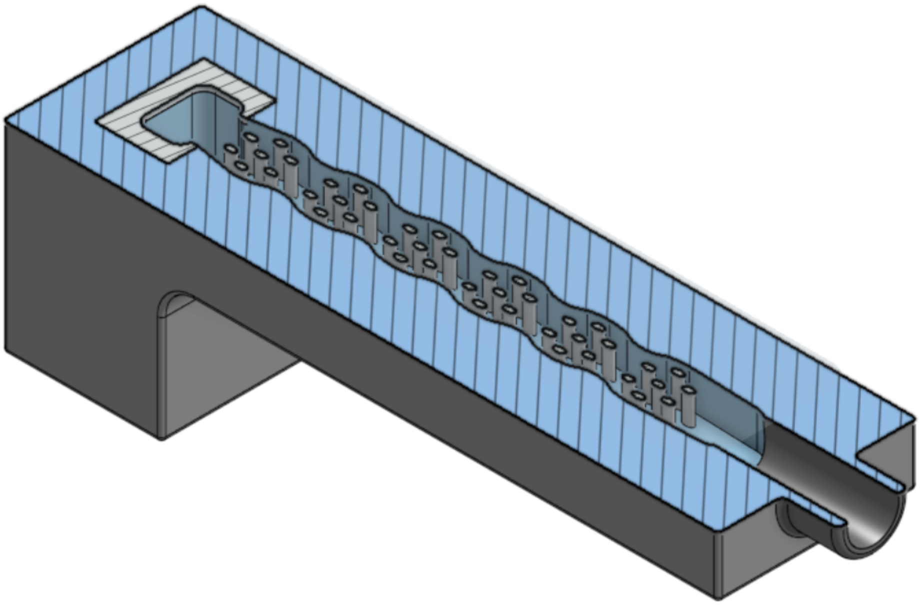

Figure 7.35: Final design cross section. Radial positioning efficient cold plate.

When fluid moves through a curved channel, centrifugal forces push the fluid outward, creating a pressure gradient between the inner and outer walls. This gradient drives secondary flow motion **Dean vortices** which appear as two counter-rotating cells within the cross section. This vortices can become asymmetric and unstable, leading to turbulence.
This can cause additional (unwanted) pressure drop, compared to the one already deriving from the 90° bend.

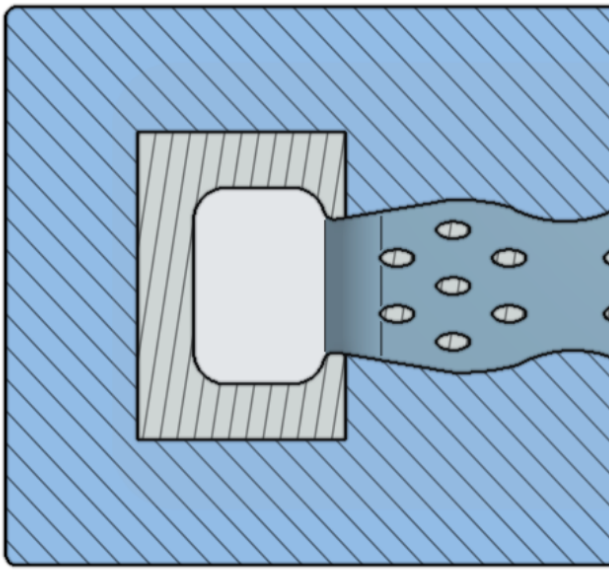

Figure 7.36: Outlet bending, channel section. Shape highlight.

A rectangular cross section with rounded corners as in Figure 7.36 keeps the vortices more localized, promoting more stable vortex centres. Moreover rounded corners softens abrupt geometric transitions, preventing the creation of local recirculation zones and velocity stagnation points. Basically the choice is driven always by the same aim, minimizing the ΔP.

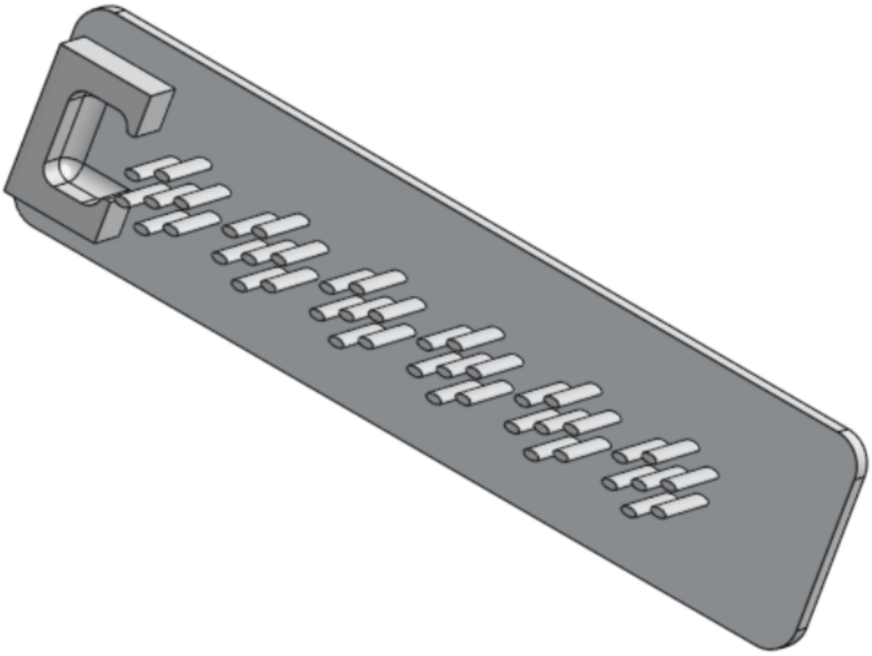

Figure 7.37: Staggered elliptical pin cold plate, final design.

REMARK: Because of non-discolure reasons the simulation results in terms of T_j and pressure drop ΔP cannot be shown.

8 R134a refrigerant cooling

8.1 Introduction

When shifting to refrigerant cooling the cooling design must be completely rethought based on 2 different key parameters:

- Different fluid properties and how they affect heat transfer efficiency.
- Different boundary conditions that, as it will be further highlighted, are dependent on the working conditions of the refrigeration cycle.

Differently from water-glycol cooling where two uncoupled circuits are present (see Figure 5.5), in refrigerant cooling (see Figure 5.6) the inlet boundary conditions of the cold plate are related to refrigeration cycle on the following parameters:

- a) Mass flow rate $\dot{m}$, dependent on the working map of the compressor.
- b) Inlet temperature T_{in}, dependent on the refrigeration cycle parameters.

a) MASS FLOW RATE $\dot{m}$

Every compressor is characterised by a compression map that links together efficiency, mass flow rate $\dot{m}$, pressure ratio and rotating speed.

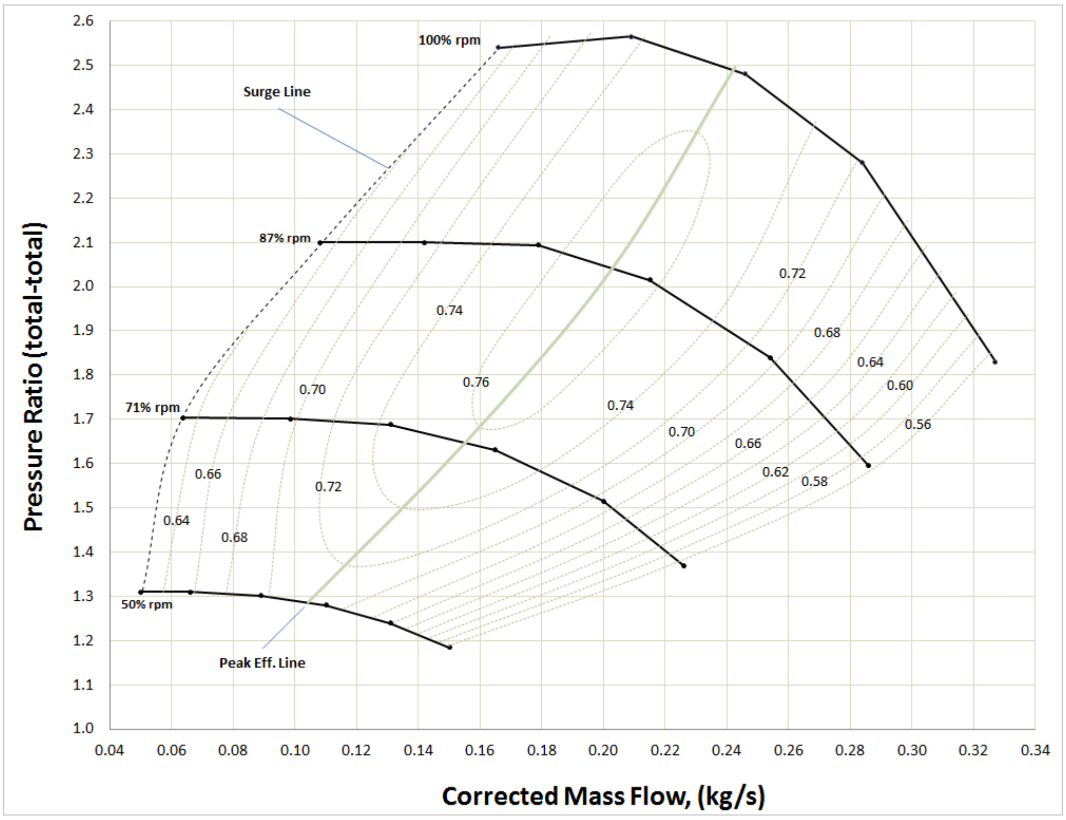

Figure 8.1: Example centrifugal compressor performance map [36].

Based on the compressor working conditions, the value of the mass flow rate through the compression stage varies accordingly. Provided that in a closed system the mass is preserved, the refrigerant circuit will be characterised by the same mass flow rate value flowing through the compressor.
As a consequence the cold plate inlet $\dot{m}$ is not a design degree of freedom anymore. It is dictated by compressor regime.
The cold plate design should guarantee target cooling performance at minimum regime (minimum $\dot{m}$) and feasible pressure drop values at the highest regime (maximum $\dot{m}$).

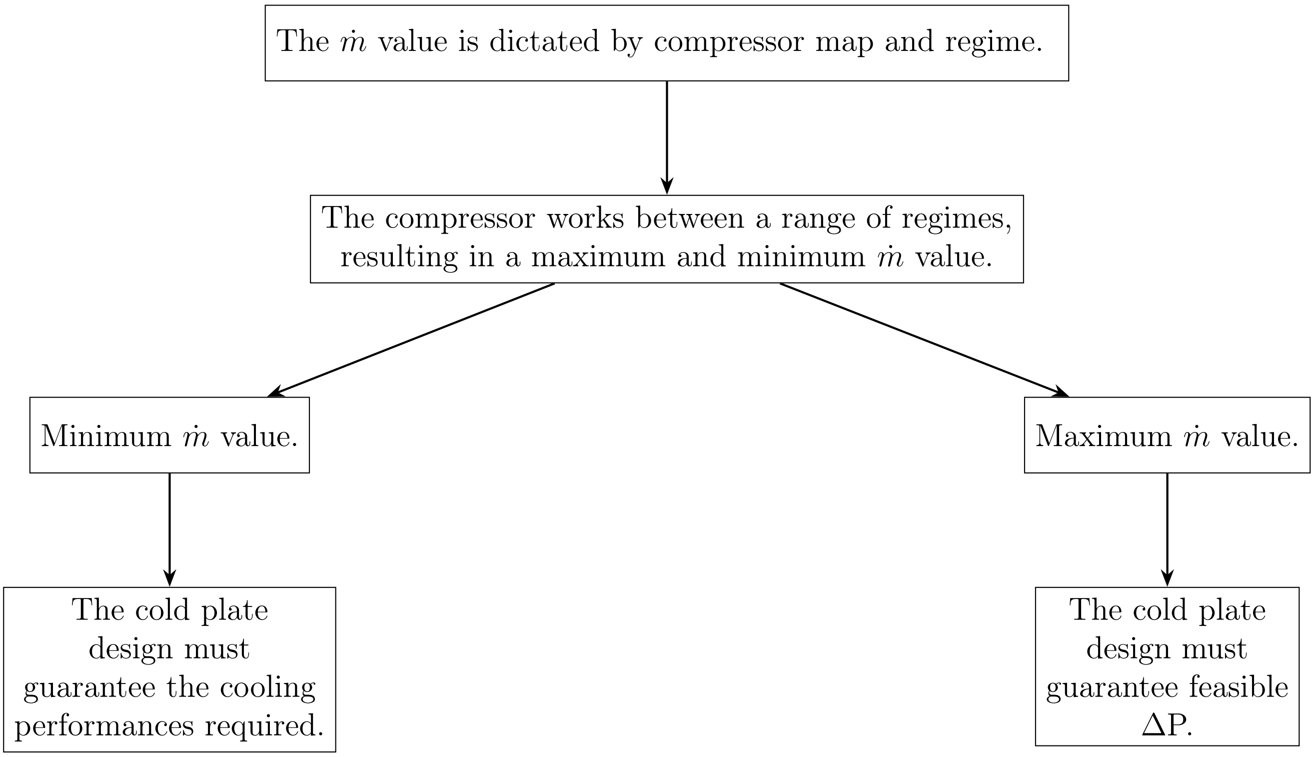

The customer set the following working conditions.

Refrigerant	**Minimum $\dot{m}$**	**Maximum $\dot{m}$**
R-134a	0.075 Kg/s	0.135 Kg/s

Table 8.1: Mass flow rate $\dot{m}$ range for R-134a.

REMARK: The maximum $\dot{m}$ in the refrigerant cycle is extremely close to the mass flow rate obtained for water-glycol of $\approx 0.14\,\mathrm{kg/s}$.
To give the study a character as general as possible, a maximum $\dot{m}$ value of $0.14\,\mathrm{kg/s}$ will be adopted.

For this reason, the Table 8.1 was modified as follows.

Refrigerant	**Minimum $\dot{m}$**	**Maximum $\dot{m}$**
R-134a	0.075 Kg/s	0.140 Kg/s

Table 8.2: Modified mass flow rate $\dot{m}$ range for R-134a.

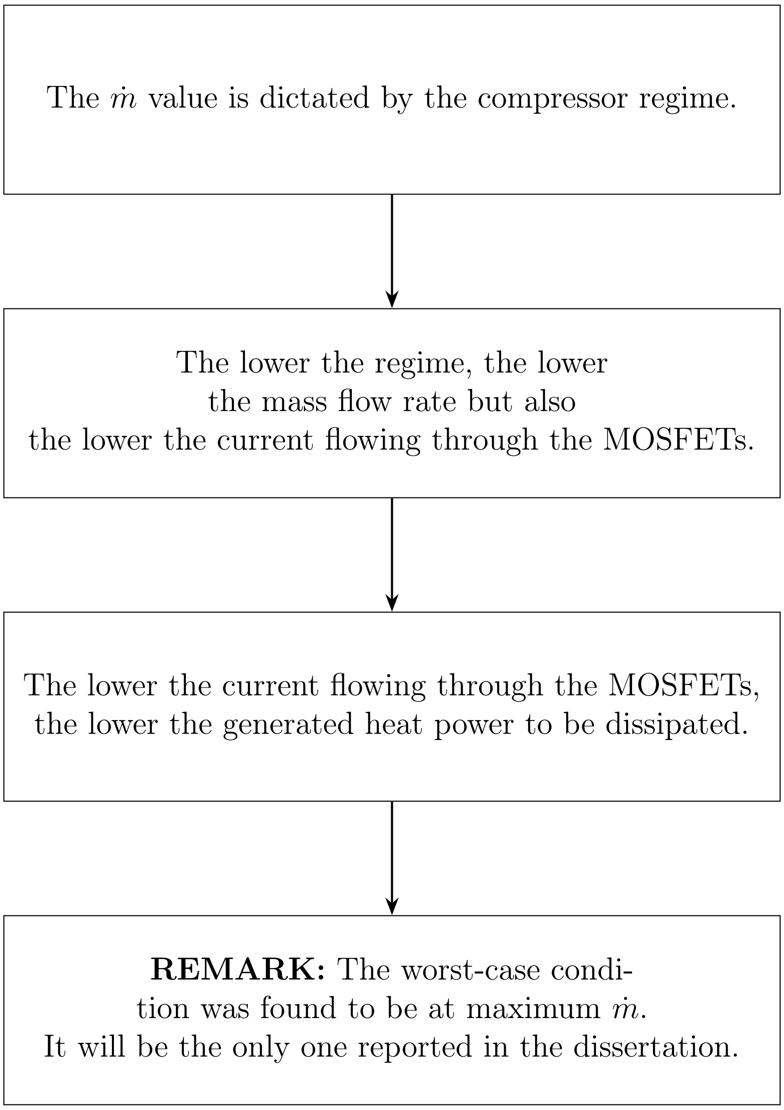

Refrigerant	**Studied case $\dot{m}$**	**Thermal power at regime**
R-134a	0.140 Kg/s	600W

Table 8.3: Studied scenario for R-134a cooling. Maximum $\dot{m}$ and thermal power Q.

b) INLET TEMPERATURE T_{in}

When shifting to refrigerant cooling the refrigeration cycle itself plays a major role too. Setting the working conditions of the refrigeration cycle becomes fundamental to assess the inlet temperature of the refrigerant T_{in}.

The conditions, set by the customer, are the following.

Parameter	**Value**
Condensation Temperature	50 °C
Evaporation Temperature	4 °C
Superheating	5 °C
Subcooling	5 °C
Compressor Efficiency	0.7

Table 8.4: Refrigeration cycle parameters.

The T_{in} could be stated directly from the previous Table by just adding to the evaporation temperature, the superheating. However, for sake of completeness, through online log p-h diagrams the inlet pressure is obtained. The "Tlk energy" website [37] provides this kind of information.

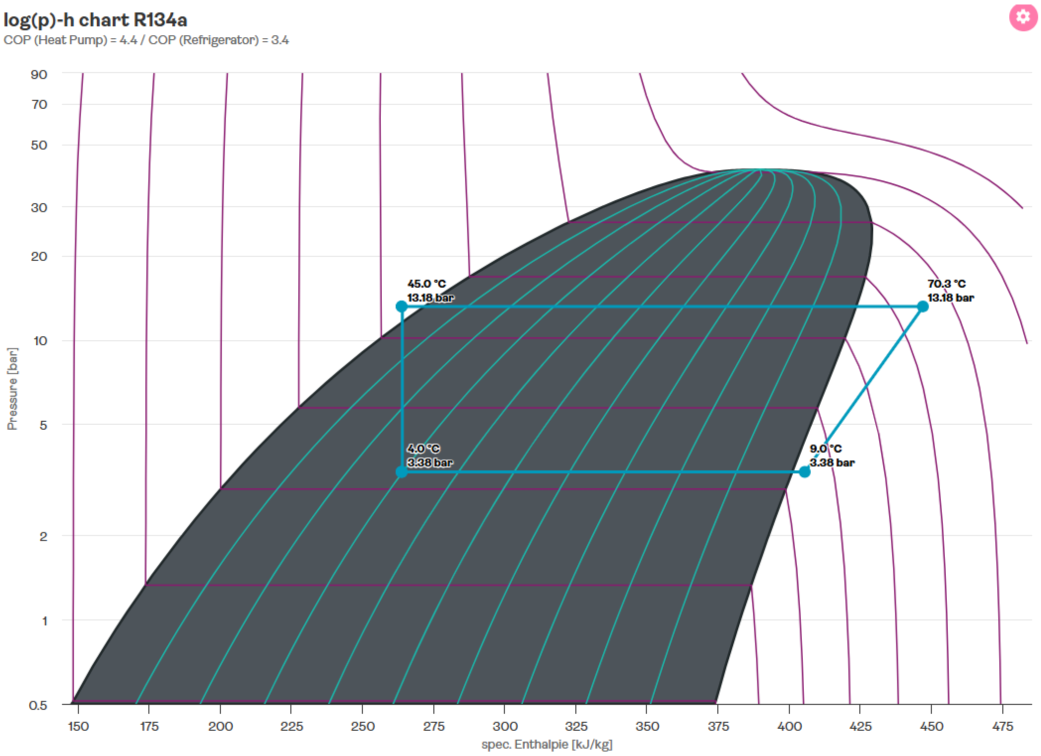

Figure 8.2: log ph chart, R134a refrigerant at cycle working conditions [37].

The results are the following.

Refrigerant	**Compression stage, Inlet absolute pressure**	**Compression stage, inlet T**
R-134a	3.38 bar	9.0 °C

Table 8.5: Compression stage, inlet constraints for R-134a refrigerant.

Now that both $\dot{m}$ and T_{in} are known, the inlet cold plate conditions are set.
The inlet pressure is an interesting parameter to keep in mind. If subtracting the pressure drop found through simulation, the cold plate outlet static pressure can be found. From it the influence of the ΔP on the COP refrigeration coefficient can be studied.

In the following Figure the main consequences on integrating the inverter cold plate and the electric motor cooling jacket inside the refrigerant circuit are shown. When passing through the two mentioned components the refrigerant partially loses its pressure and increases its temperature.

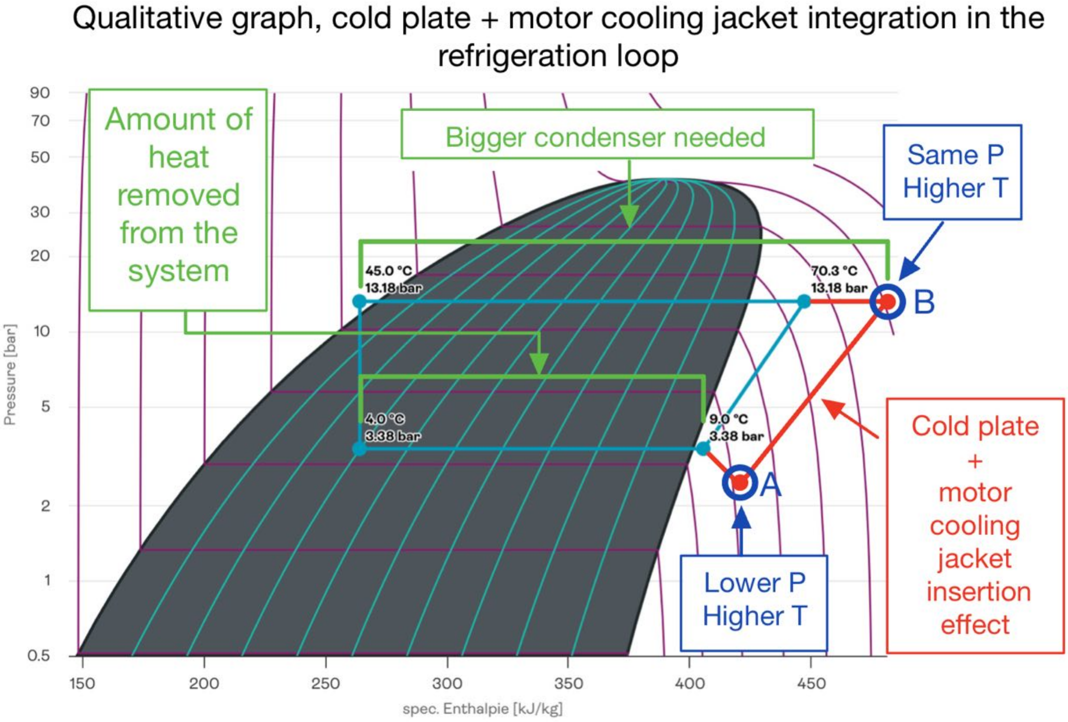

Figure 8.3: Qualitative graph, consequences on integrating the inverter cold plate and the motor cooling jacket inside the refrigerant circuit.

It results in a shift from the original refrigeration cycle equal to point A and B in Figure 8.3. When exiting the cooling jacket (point A), the refrigerant enters the compression stage and it's compressed until point B, shifted to the left w.r.t the original final compression point. The condenser size will have to be able to dissipate the additional amount of heat derived from cold plate cooling ⇒ **higher condenser size required**.

However the most undesired effect is the **decrease in compression efficiency**. Indeed a lower starting pressure, keeping constant the final compression pressure, leads to higher required work (W) to the compressor electric motor. However the amount of heat dissipated from the system remains the same.

$$\text{Given that } COP = \frac{Q}{W} \Rightarrow \text{Higher W value} \Rightarrow \text{Same dissipated Q} \Rightarrow \text{COP}\downarrow$$

Where Q represents the removed heat in Watt.
The aims of the discussion are both to give a general picture of the issues to face, but mainly to justify the concern for pressure drop limitation when approaching the new design. The topic will be further developed through a proper **sensitivity analysis**.

Another take away concept resulting from the previous discussion is that **for refrigerant cooling one design degree of freedom is lost.**
When dealing with water-glycol cooling, the development degrees of freedom are three: channel geometry, materials and input boundary conditions. While in case of refrigerant cooling, the input boundary conditions are set by the refrigeration cycle specifications indicated by the customer.

	Degrees of freedom		
Cooling fluid	Inlet boundary conditions	Channel geometry	Materials
Water glycol (50-50%in volume)	✓	✓	✓
R-134a (gaseous)	X	✓	✓

Table 8.6: Design degrees of freedom comparison.

Now the technical data of R-134a are reported and compared to the one of water-glycol.

8.2 Shifting to refrigerant cooling, theoretical approach

Parameter	R-134a (at 3.38 bar and at 9°C)	Water glycol 50-50% in volume (at 40°C)	Comment
ρ (Kg/m^3)	16,160 [38]	1075,4 [33]	Density values are much lower for the refrigerant.
μ (Pa·s)	$1{,}108 \cdot 10^{-5}$ [38]	$2{,}495 \cdot 10^{-3}$ [33]	A much lower dynamic viscosity results in higher Reynolds number for the refrigerant at equal conditions.
c_p (J/(Kg·K))	907,510 [38]	3404,6 [33]	Lower specific heat means gas heats up more quickly per unit of absorbed energy.
K (W/m·K)	$1{,}230 \cdot 10^{-2}$ [38]	0,404 [33]	Much lower thermal conductivity for R-134a, higher difficulty in heat transfer through the gas.
ν (m^2/s)	$6{,}863 \cdot 10^{-7}$ [38]	$2{,}320 \cdot 10^{-6}$ [33]	Lower kinematic viscosity affects flow and heat transfer characteristics.

Table 8.7: R-134a and water glycol (50-50%) comparison table. Water-glycol properties refer to 40°C.

Based on data reported in Table 8.7 general considerations can be made on refrigerant behaviour. The new cold plate geometry, if necessary, will be modified according to this initial considerations.

The R-134a, being in gaseous form, presents a much lower density values compared to water-glycol. In terms of heat dissipation this doesn't represents the only obstacle.

- Lower ρ values $\Rightarrow$ fewer molecules per unit volume to absorb and carry heat away.
- Lower ρ values $\Rightarrow$ to maintain a comparable mass flow rate $\dot{m}$ the volume flow rate has to be extremely higher $\Rightarrow$ great increase in pressure drop.
- Lower c_p $\Rightarrow$ refrigerant heats up more quickly per unit of absorbed energy $\Rightarrow$ ΔT between inlet and outlet port.
- Lower thermal conduct. K $\Rightarrow$ low K makes it harder for heat to move through the gas.

However not all the refrigerant characteristics work against heat convection.

- Much lower μ $\Rightarrow$ coupled with the much higher velocity values $\Rightarrow$ higher Re number.

The step that naturally follows is understanding how the different fluid parameters influence the cold plate design development. The aim would be to provide actual ratio values in terms of contact surface area change, pin placement and shape.
However, as will further be highlighted, the different parameters are so related/linked between each other that detailed considerations are difficult to be made. Just considerations of general character can be done.

Now a starting analysis is developed leveraging the parameters introduces in **Section 7**.

Parameter	**Formula**	**Units**	**Description**
Heat transfer coefficient h	$h = \frac{Nu \cdot K}{D_h}$	$\frac{W}{K \cdot m^2}$	Convective heat transfer coefficient
Nusselt number Nu	$Nu = 0.664 \cdot Re^{0.5} \cdot Pr^{1/3}$	Dimensionless	Valid for laminar flow.
Nusselt number Nu	$Nu = 0.037 \cdot Re^{0.8} \cdot Pr^{1/3}$	Dimensionless	Valid for turbulent flow.
Reynolds number Re	$Re = \frac{\rho \cdot v \cdot D_h}{\mu}$	Dimensionless	Measures flow turbulence
Hydraulic diameter D_h	$D_h = \frac{4 \cdot A}{P}$	m	Equivalent diameter for non-circular channels
Prandtl number Pr	$Pr = \frac{c_p \cdot \mu}{k}$	Dimensionless	Ratio of momentum to thermal diffusivity

Table 8.8: Summary of key heat transfer and fluid flow parameters [34].

In the following scheme shows the steps that the upcoming reasoning will follow.

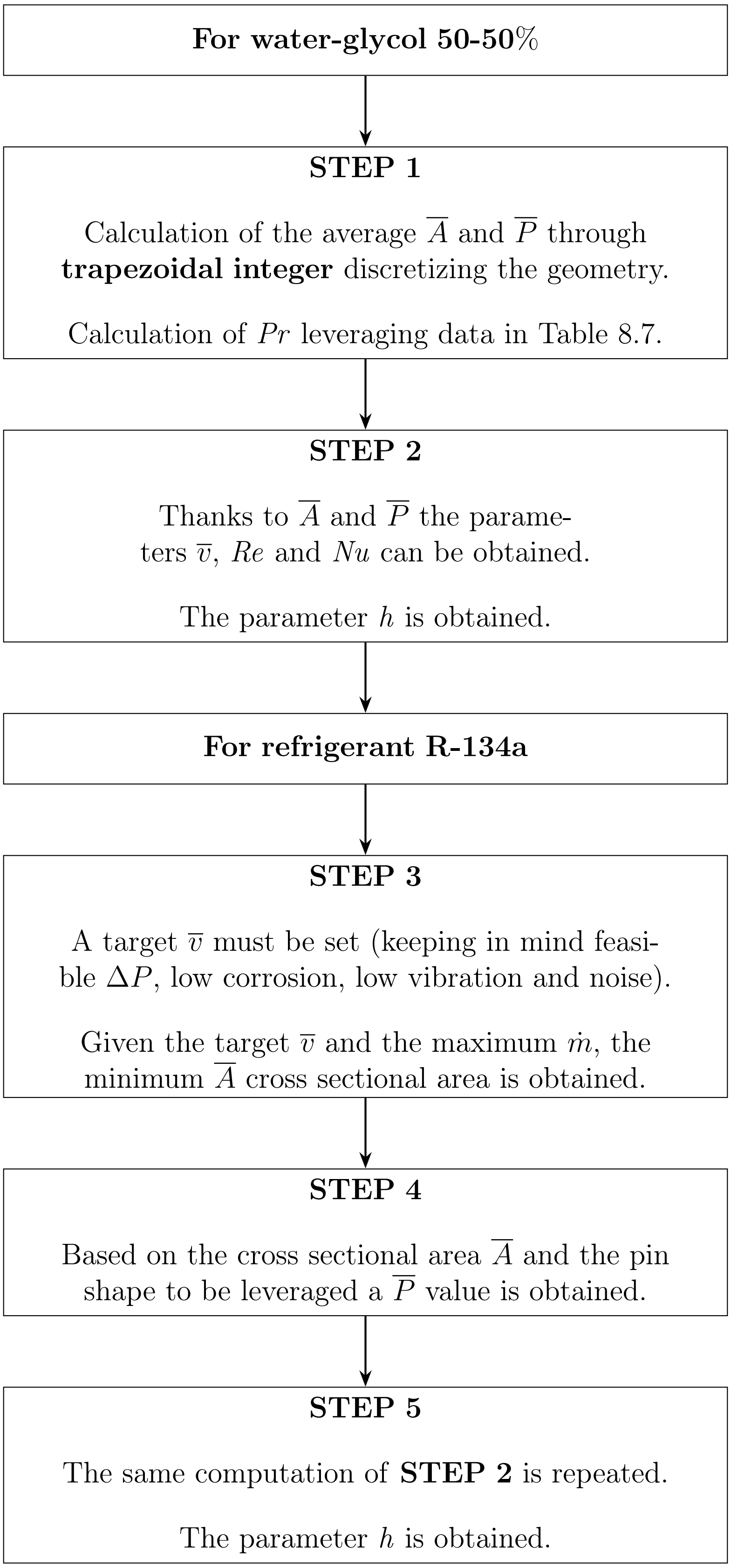

Figure 8.4: Workflow for determining convective heat transfer coefficient h for both water-glycol 50-50% and refrigerant R-134a.

Comparison between water-glycol 50-50% and R-134a

STEP 6

From thermofluid dynamics laws the heat transfer between cold plate and fluid is governed by the law:

$$Q = h \cdot A_{contact} \cdot (T_{cold\ plate} - T_{fluid})$$

Where $A_{contact}$ is the cold plate surface contact area.

STEP 7

The amount of thermal power Q to be carried away is the same for both cooling approaches.

Assigning 1 to water-glycol and 2 to refrigerant:

$$Q_1 = Q_2$$

STEP 8

In the comparison, ΔT is considered the same for both applications for two reasons:

The aim is to uncouple the equation from ΔT and make it dependent only on fluid properties and cold plate geometry.

STEP 9

Since $\Delta T_1 = \Delta T_2$ and both cooling targets must be met, the following must hold:

$$\frac{h_1 \cdot A_{contact\ 1}}{h_2 \cdot A_{contact\ 2}} = 1$$

REMARK!!

The inlet T for R-134a is much lower compared to water-glycol (9°C vs 40°C).

Therefore, it is expected that: $\Delta T_2 \quad > \quad \Delta T_1$.

STEP 10

CONCLUSION

A reference maximum ratio between contact surface areas is obtained from STEP 9:

$$\frac{A_{contact\ 1}}{A_{contact\ 2}} \leq X \quad \text{(specific value)}$$

Figure 8.5: Comparison of heat transfer principles between water-glycol 50-50% and refrigerant R-134a, with derivation of area ratio conditions under equivalent thermal power transfer.

Let's proceed to actual calculation to obtain some tangible values as reference.

The obtained values will then be compared to what found through simulation. **In this way it can be stated if the theoretical approach is close enough to reality or it can be just used as general guidance tool**.
The first step is determining the D_h of the last water-glycol optimized geometry (see Figure 7.27).
To do so the subsequent steps were carried out:

- From the entire channel length a single pin area was isolated.

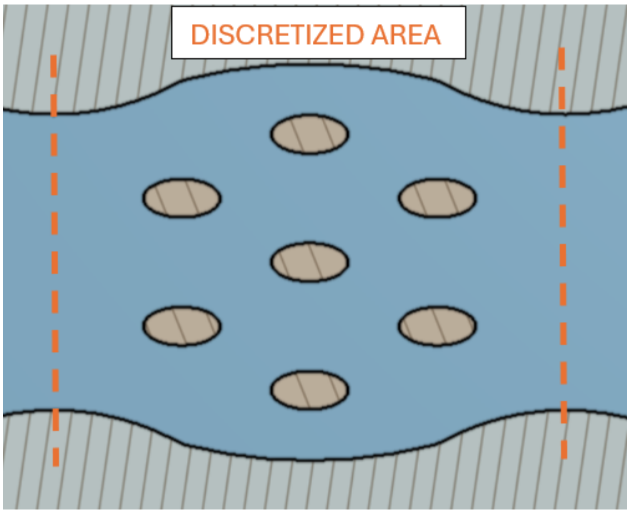

Figure 8.6: Discretized pin area, water-glycol cooling final design 7.30.

  The reason is that the heat convection is mainly dependent on the interaction between the fluid and those area. Moreover the pattern is the same in correspondence of all the pins.

- The geometry was discretized through its length with intervals of 0.1 mm in length.

- To pass from discretization to an average value $\overline{A}$ and $\overline{P}$ integrals are used.
  For example, in case of area application:

$$\overline{A} = \frac{1}{L}\int_0^L A(x)\,dx$$

  Leveraging trapezoidal integral law, the $\overline{A}$ and $\overline{P}$ were found. The mathematical relationship is expressed as follows

$$\int_a^b f(x)\,dx \approx \sum_{k=1}^{N} \frac{f(x_{k-1}) + f(x_k)}{2}\,\Delta x_k \tag{8.1}$$

  Once this two parameters were present, the calculation of $\overline{D_{h1}}$ was possible.

The results are summarized in the Table down below.

Fluid	Study case $\dot{m}$	Thermal power at regime	$\overline{A}$	$\overline{P}$	$\overline{D_h}$
Water-glycol 50-50%	0.140 kg/s	100 W	$187{,}9 \cdot 10^{-6}\ m^2$	$87{,}2 \cdot 10^{-3}\ m$	$8{,}61 \cdot 10^{-3}\ m$

Table 8.9: Water-glycol 50-50% geometry parameters calculation. The channel design is the one depicted in Figure 7.27.

Substituting the parameters inside the formulas in Table 8.8 the following values were obtained.

Fluid	$\overline{v}$	Pr	Re	h	Flow type
Water-glycol 50-50%	0.71 (m/s)	21	$2,63 \times 10^3$	$4,37 \times 10^3\ \frac{W}{m^2 \cdot K}$	TRANSITIONAL FLOW

Table 8.10: Water-glycol 50-50% geometry parameters calculation.

To carry on with the comparison it's now time to pass to the calculation of R-134a parameters. However to accomplish the task some parameters of reference must be previously set.

Target fluid $\overline{v}$	**Maximum fluid v**	**Comment**
15 m/s	25 m/s	The reasons are the following: • Vibration and noise limitation. • Cold plate erosion avoidance.

Table 8.11: R-134a velocities magnitudes.

Once the target $\overline{v}$ is set, given the volume flow rate it's possible to obtain a target $\overline{A}$ cross section area.

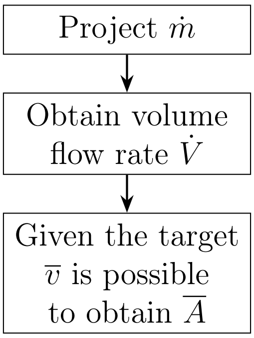

Once the $\overline{A}$ value is found, it's possible to think of a possible $\overline{P}$ shape that satisfies the obtained value. The chosen pins are always elliptical in shape, 3 in correspondence of each MOSFET.

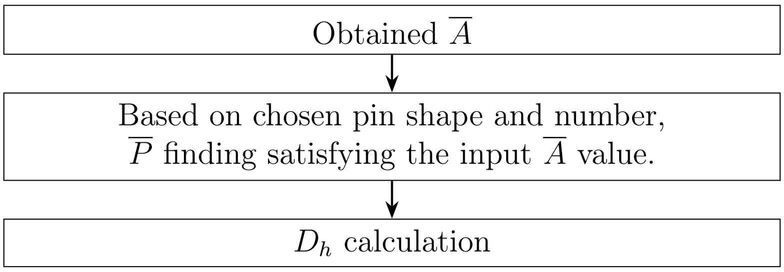

As already done for water-glycol application, all the needed parameters can now be found.

REMARK: between the pins the cross section is lower and the risk to exceed 25 m/s is possible. A little higher $\overline{A}$ than the calculated one is leveraged.

Fluid	Study case $\dot{m}$	Calculated $\overline{A}$	Actual $\overline{A}$	$\overline{P}$	$\overline{D_h}$
R-134a	0.140 kg/s	577,56$\cdot 10^{-6}$	608 $\cdot 10^{-6}$ m^2	578 $\cdot 10^{-3}$ m	4,2 $\cdot 10^{-3}$ m

Table 8.12: R-134a geometry parameters calculation. The channel design is the one depicted in Figure 8.8.

Fluid	$\overline{v}$	Pr	Re	h	Flow type
R-134a	15 (m/s)	0,81	$9,21 \cdot 10^4$	947 $\frac{W}{m^2 \cdot K}$	TURBULENT

Table 8.13: R-134a geometry parameters calculation. Theoretical results.

Recalling the equation stated at **STEP 9**, the following relationship is imposed.

$$\frac{h_1 \cdot A_{contact\ 1}}{h_2 \cdot A_{contact\ 2}} = 1$$

As a consequence, for the specific case analysed, the contact surface area ratio when shifting from water-glycol to R-134a refrigerant:

$$\boxed{\frac{A_{\text{contact }2}}{A_{\text{contact }1}} \leq 4,56}$$

What was found is an upper limit in terms of contact surface area. The intrinsic meaning is giving a constraint in terms of maximum area ratio to guide the development of the new cold plate design. **Through simulation it will be stated if this value has a real application meaning too or it must be taken as a general guideline.**

The found ratio is specific of the chosen geometry, down below a more general formula is presented. In this way, by plugging in the specific case data, the ratio can be found.
Recalling that:

- 1 is assigned to water-glycol.
- 2 is assigned to R-134a.

$$Nu_2 = 0.037 \cdot \left(\frac{\rho_2 \cdot v_2 \cdot D_{h2}}{\mu_2}\right)^{0.8} \cdot \left(\frac{c_{p2} \cdot \mu_2}{k_2}\right)^{1/3}$$

$$Nu_2 = 0.037 \cdot \left(\frac{\rho_2}{\mu_2}\right)^{0.8} \cdot \left(\frac{c_{p2} \cdot \mu_2}{k_2}\right)^{1/3} \cdot (v_2 \cdot D_{h2})^{0.8}$$

Setting:

$$X_2 = 0.037 \cdot \left(\frac{\rho_2}{\mu_2}\right)^{0.8} \cdot \left(\frac{c_{p2} \cdot \mu_2}{k_2}\right)^{1/3}$$

The Nusselt number can be rewritten as:

$$Nu_2 = X_2 \cdot (\overline{v_2} \cdot D_{h2})^{0.8}$$

$$h_2 = \frac{Nu_2 \cdot k_2}{D_{h2}} = \frac{X_2 \cdot (\overline{v_2} \cdot D_{h2})^{0.8} \cdot k_2}{D_{h2}} = \frac{X_2 \cdot k_2 \cdot (\overline{v_2})^{0.8}}{(D_{h2})^{0.2}}$$

Recalling the ratio:

$$A_{contact2} \leq \frac{h_1 \cdot A_{contact1}}{X_2 \cdot k_2} \cdot \frac{(D_{h2})^{0.2}}{(\overline{v_2})^{0.8}}$$

Recalling that:

$$D_h = \frac{4 \cdot \overline{A}}{\overline{P}}$$

Where $\overline{A}$ is the average cross section and $\overline{P}$ the wetted perimeter.

$$A_{\text{contact2}} \leq \frac{h_1 \cdot A_{\text{contact1}}}{X_2 \cdot k_2} \cdot \frac{\left(\frac{4 \cdot \overline{A_2}}{\overline{P_2}}\right)^{0.2}}{(\overline{v_2})^{0.8}}$$

The average cross section $\overline{A}$ is related to volume flow rate $\dot{V}$ and target velocity $\overline{v}$.

$$A_{\text{contact2}} \leq \frac{1,32 \cdot h_1 \cdot A_{\text{contact1}}}{X_2 \cdot k_2} \cdot \frac{\left(\frac{\dot{V_2}}{\overline{v_2} \cdot \overline{P_2}}\right)^{0.2}}{(\overline{v_2})^{0.8}}$$

The final equation that can be found is:

$$A_{\text{contact2}} \leq \frac{1,32 \cdot h_1 \cdot A_{\text{contact1}}}{X_2 \cdot k_2} \cdot \frac{\left(\frac{\dot{V_2}}{\overline{P_2}}\right)^{0.2}}{(\overline{v_2})}$$

Where:

- $(h_1 \cdot A_{contact1})$ results from the water-glycol successful design (the one that provided the expected performances). The unit is W/K.
- $\overline{P_2}$ Cross section perimeter, refrigerant cooling design.
- $X_2 = 0.037 \cdot \left(\frac{\rho_2}{\mu_2}\right)^{0.8} \cdot \left(\frac{c_{p2} \cdot \mu_2}{k_2}\right)^{1/3}$
- k_2 thermal conductivity of the refrigerant (W/m/K).
- $\dot{V_2}$ refrigerant volume flow rate (m^3/s).
- $\overline{v_2}$ target average velocity (m/s).

In the next page, all the considerations made until now can be briefly summarized in a Flowchart.

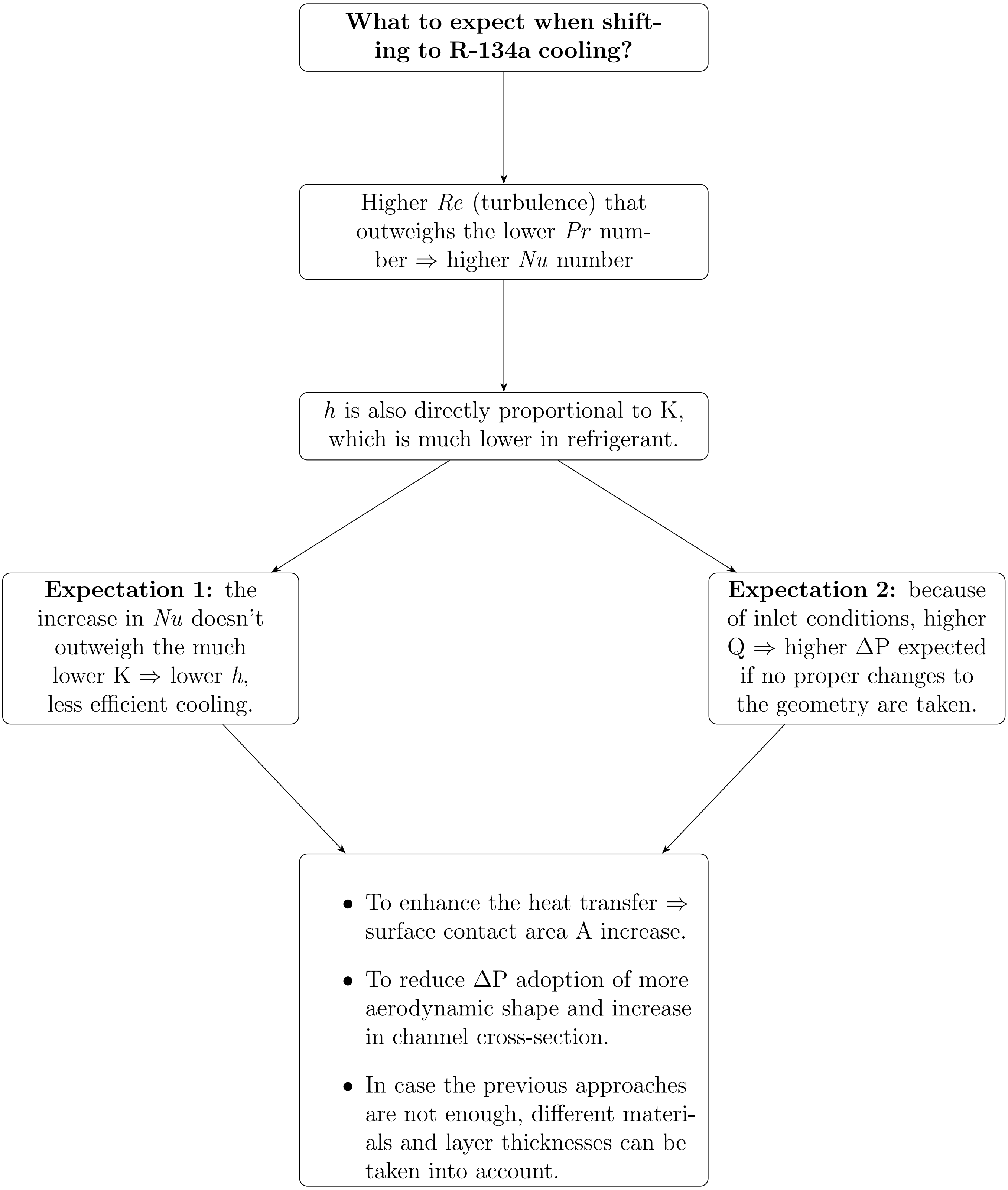

What to expect when shifting to R-134a cooling?

Higher *Re* (turbulence) that outweighs the lower *Pr* number ⇒ higher *Nu* number

h is also directly proportional to K, which is much lower in refrigerant.

Expectation 1: the increase in *Nu* doesn't outweigh the much lower K ⇒ lower *h*, less efficient cooling.

Expectation 2: because of inlet conditions, higher Q ⇒ higher ΔP expected if no proper changes to the geometry are taken.

- To enhance the heat transfer ⇒ surface contact area A increase.
- To reduce ΔP adoption of more aerodynamic shape and increase in channel cross-section.
- In case the previous approaches are not enough, different materials and layer thicknesses can be taken into account.

Figure 8.7: Flowchart summarizing thermal and hydraulic expectations when switching to R-134a cooling, with strategies to address potential challenges.

The new cooling channel design and cold plate geometry was developed in accordance with the above drawn conclusions.

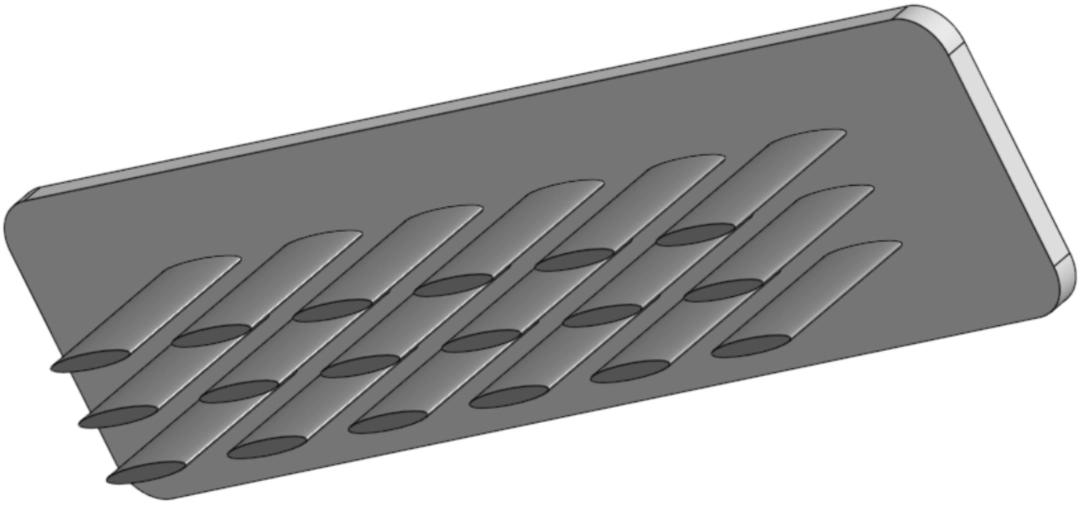

Figure 8.8: Refrigerant R-134a, first cold plate design.

The steps included the redefinition of pins number, geometry and displacement. As shown in Figure 8.8, the elliptical shape was kept. However the major axis length was remarkably increased both to make the shape more aerodynamic and to enhance the available contact surface area.
At this point, the contact surface area was still kept under the found value of 4,55 times the water-glycol contact surface area design.

Some initial conclusions were obtained.

Refrigerant (gaseous)	Contact surface area	Pressure drop ΔP	$T_{j\ max}$
R-134a (9 °C)	2,5 $\cdot A_{contact1}$	1044 Pa	204 °C

Table 8.14: First cold plate design (see Figure 8.8) fundamental parameter results.

First of all the pressure drop has a feasible value, meaning that the pin geometry doesn't impact too much on refrigerant leaving it too flow smoothly through the channel.
Second the increased surface area is not enough to properly cool down the MOSFETs, that shows still high temperature values (see Table 8.14).

8.3 Final design

Many tentative were done before obtaining the proper design allowing to meet the expected performances in terms of pressure drop ΔP and temperatures T_j.

The following design choices were taken:

- Increase of pins total height. Differently from water-glycol case the difference in temperature between cold plate and refrigerant is higher. So even though the height is increased, a ΔT between the tip of the pin and the refrigerant is still present. An increased channel height allows to obtain better inlet to channel cross section ratio (w.r.t increasing the channel width), reducing the pressure drop at both inlet and outlet.
- Increase in the pin number in order to maximize the contact surface area.
- The spacing between the pins results from a **trade-off** between proximity to central area where the thermal heat is concentrated and hydraulic resistance to the flow.
- Given that the spacing between pins was low, to obtain the average target velocity into the channel **two by-pass side channels** slightly wider than the central one were introduced. In this way a greater part of the flow can travel in those areas stabilizing the average refrigerant velocities between the pins where the cross-section is lower.

The design obtained is the following one. Both 3D images and then proper quotation of the model is reported.

Starting with the actual cold plate isolated from the rest of the channel.

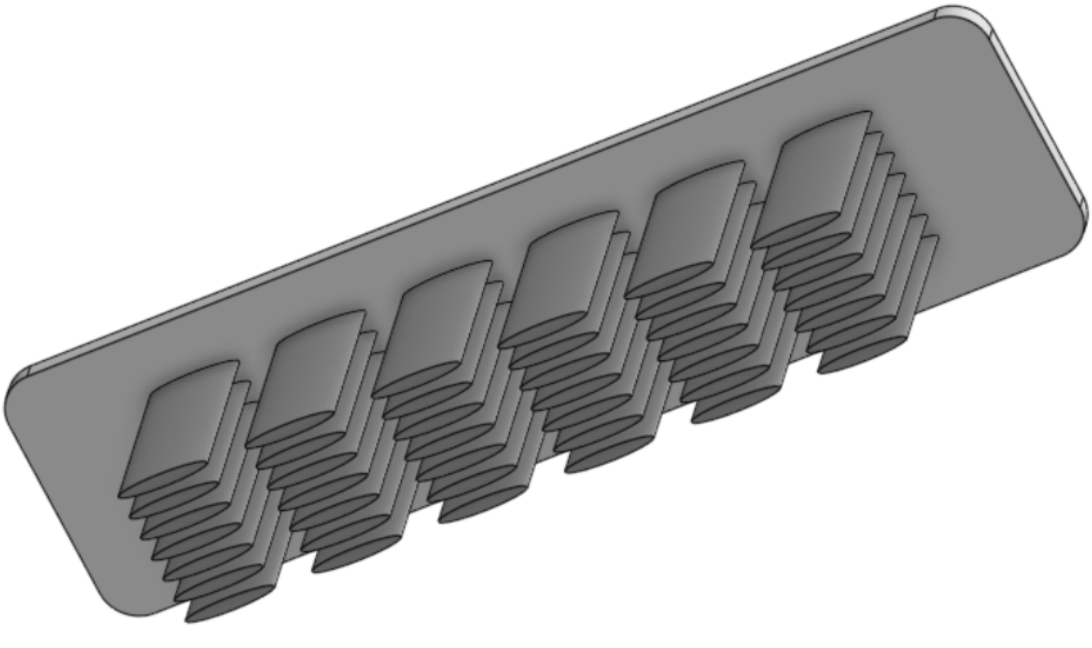

Figure 8.9: Final cold plate pin design. Seven elliptical pins in correspondence of every Mosfet.

Specifically, the new design data are the following.

Refrigerant (gaseous)	Expected maximum contact surface area	Actual contact surface area	$T_{j\ max}$
R-134a (9 °C)	$\leq 4{,}55 \ \cdot A_{contact1}$	$\approx 7 \ \cdot A_{contact1}$	156 °C

Table 8.15: Final cold plate design, fundamental parameter results.

IMPORTANT CONCLUSIONS

- The theoretical approach is valuable in defining a general path when shifting from one cooling approach to another.
- The results obtained through simulation, thought, don't reflect the expected values for h and max $A_{contact}$.
- From simulation, the refrigerant shows much lower h, so higher $A_{contact}$ is needed.

Table 8.16: Important conclusions in terms of theoretical approach validity and simulation results.

The massively increased contact surface area allowed to obtain maximum junction temperatures close enough to the target T_j of 150°C (Table 8.14). The result is considered to be satisfactory both in an optic of comparison with the other coolants design and from an actual working condition. The gap to reach the data-sheet maximum allowed T_j it's still far ($T_{jmax} = 175$°C).

On the next page the channel cross-section is displayed and commented.

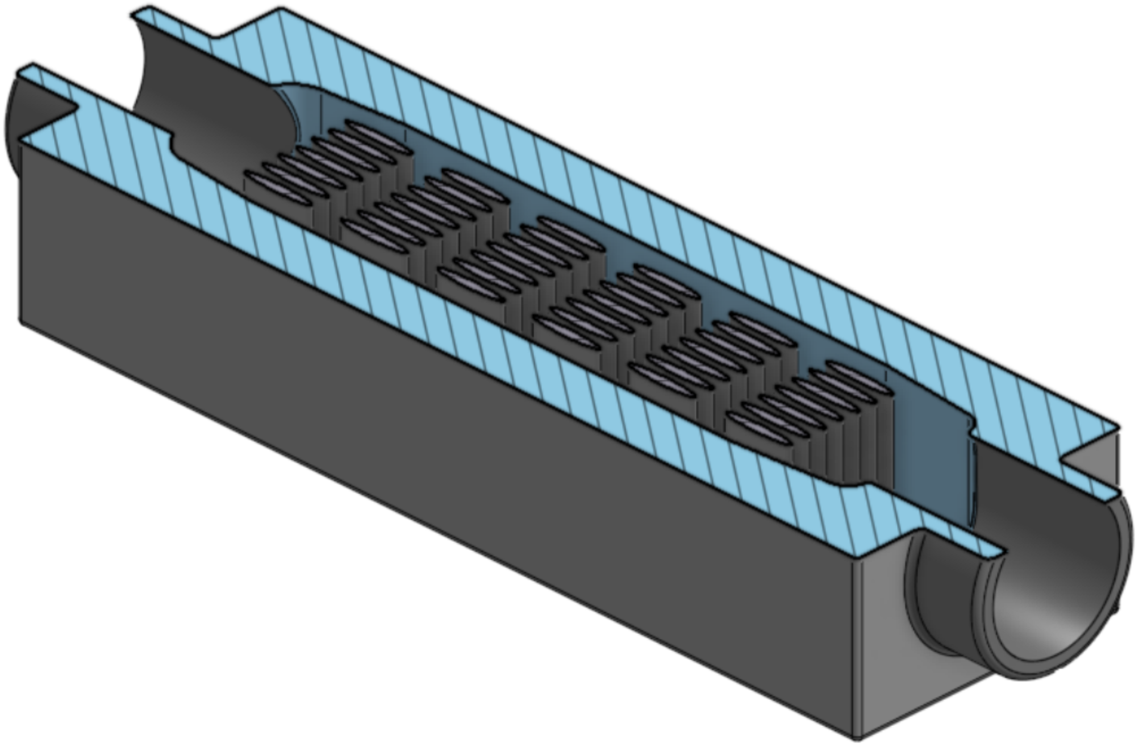

Figure 8.10: R-134a cooling channel cross section. Final design.

From a top side view, the pins arrangement is clearer. It's quite evident how two additional bypass side channels are present in the channel.

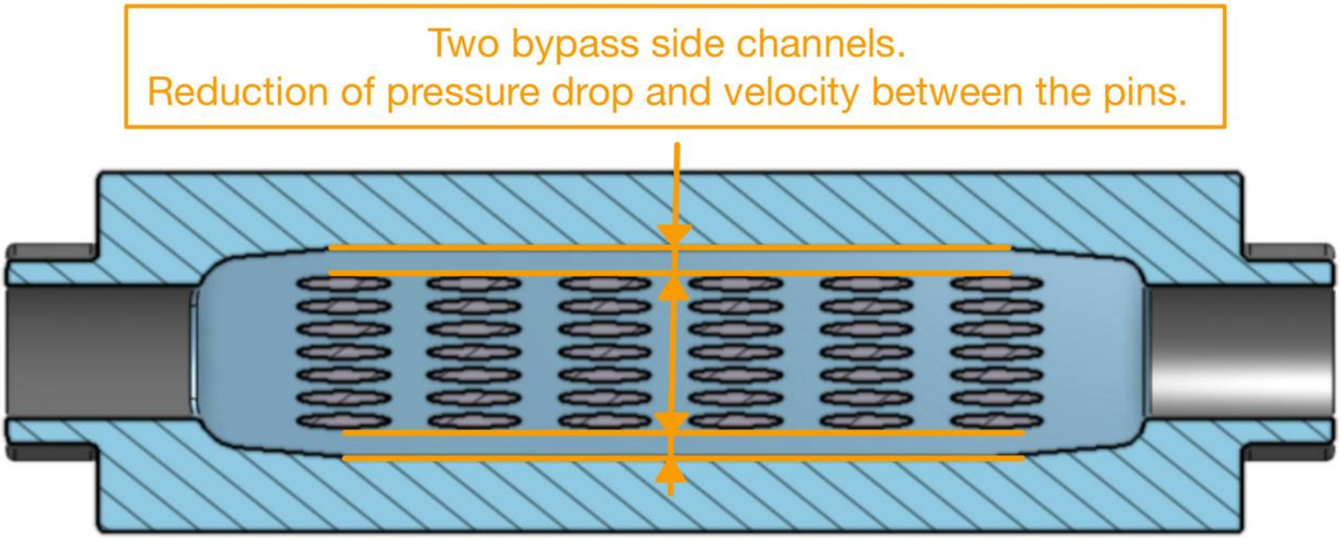

Figure 8.11: R-134a cooling channel cross section top view. Final design.

This choice was dictated by the following reasons:

- The goal is keeping the pins as close as possible to the heat source. As a consequence they were squeezed towards the centre, where the heat is concentrated.
- Lowering the available cross section between the pins increase the hydraulic resistance to the flow. In order to limit the pressure drop and keep the target $\overline{v}$, a bypass path for the refrigerant is introduced.

Obviously, even with the introduction of bypass channels, the velocity magnitude is not perfectly uniform everywhere.

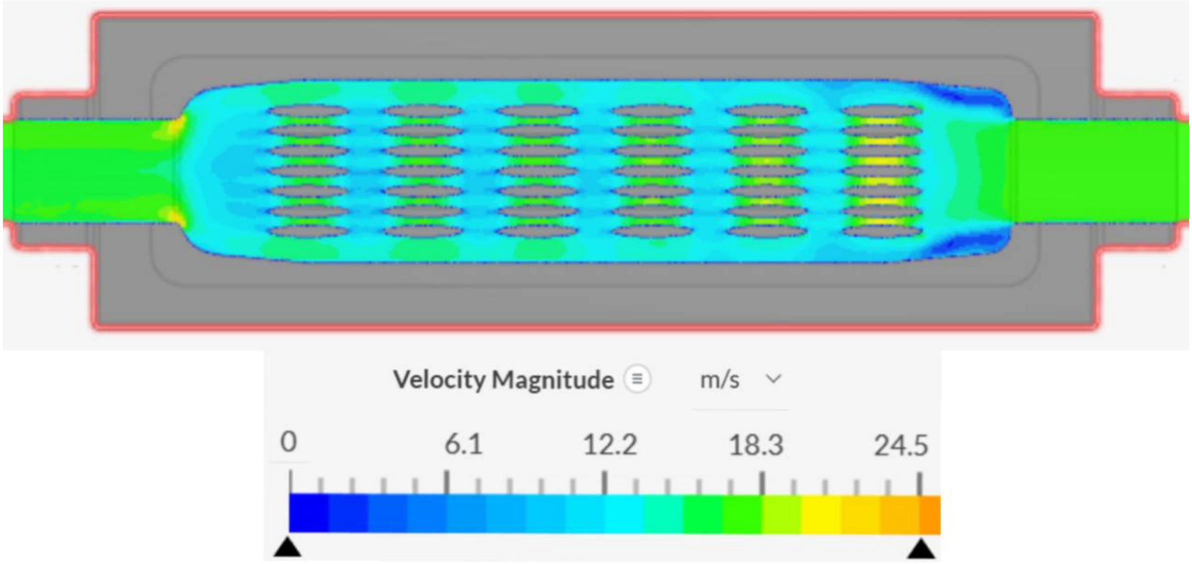

Figure 8.12: R-134a cooling channel velocity magnitudes. Final design.

Before stepping into the final results in terms of pressure drop and temperature performances, the quotation of the model is provided.

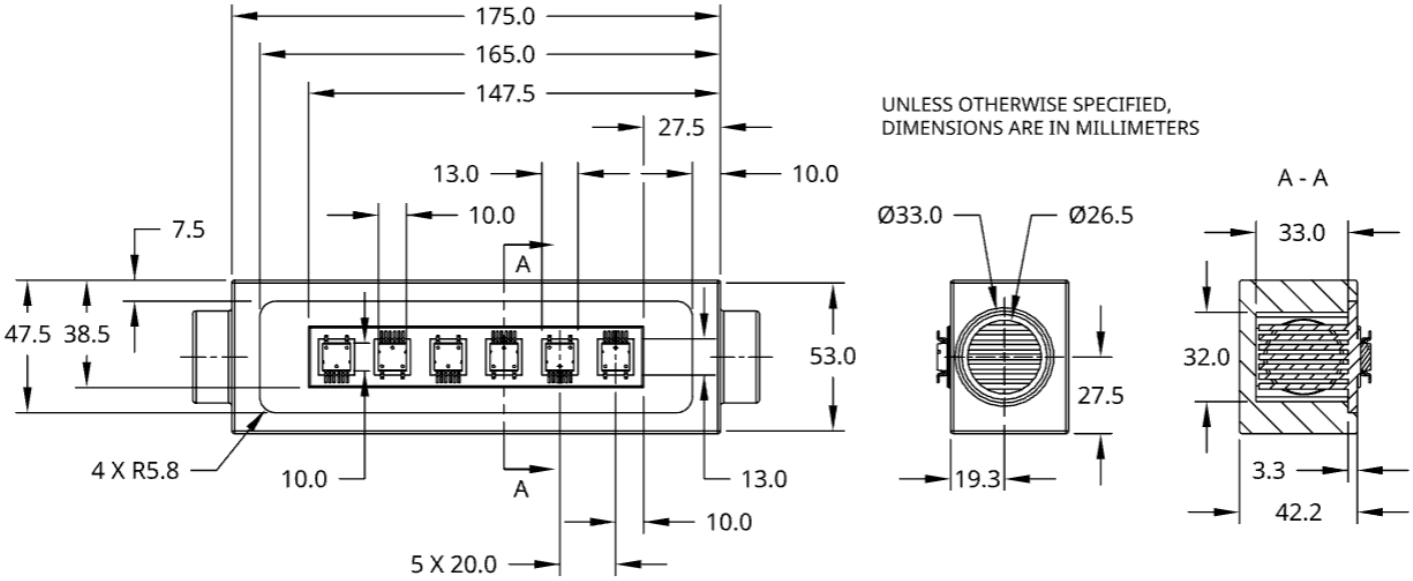

Figure 8.13: R-134a final design, quotation.

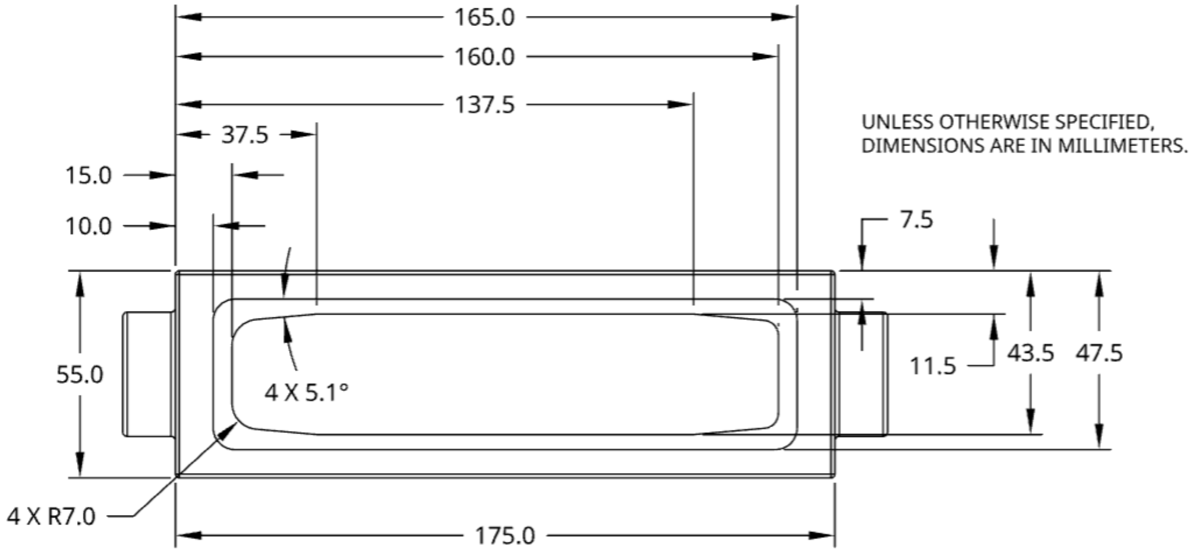

Figure 8.14: R-134a final cooling channel design, quotation.

Coming to the main part of the design, the dimensions of the cold plate pins are displayed.

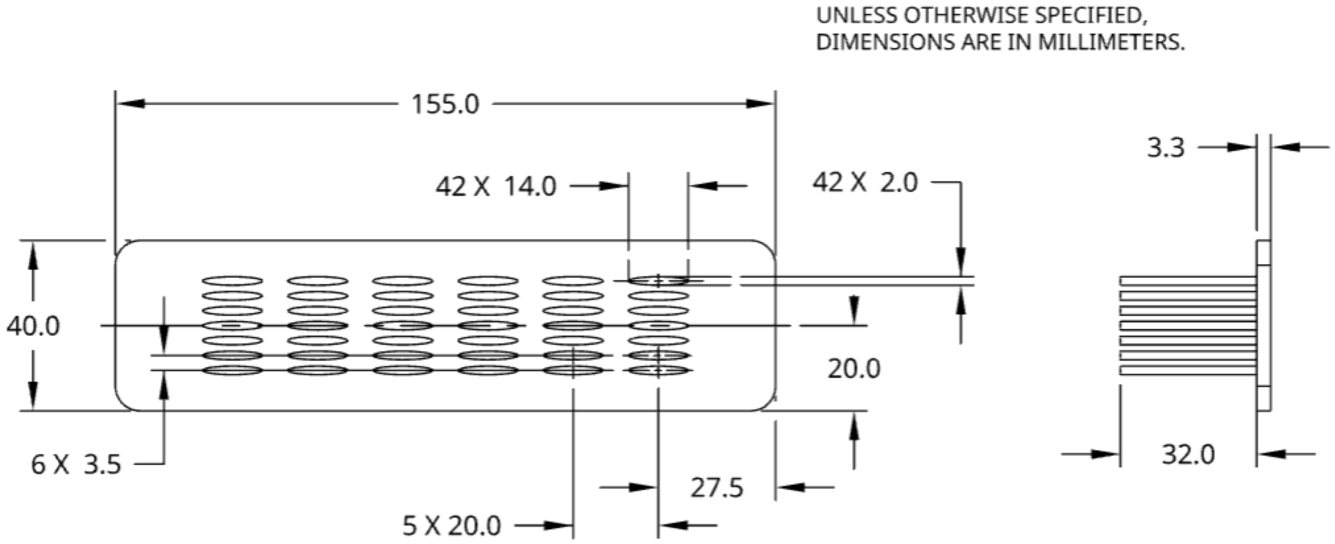

Figure 8.15: R-134a cold plate pins final design, quotation.

As visible in Figure 8.15, the adopted pins are much higher compared to the water-glycol 50-50% design, where the height was equal to 14 mm. This choice comes from the inlet refrigerant temperature set to 9°C. Travelling through the channel the temperature will slightly raise up, however a greater ΔT between cold plate and refrigerant will be kept compared to water-glycol case.

Increasing the pin height we exploit this delta, ensuring a better heat exchange to the refrigerant. As visible in Figure 8.16, the pins tips temperatures are all above 30 °C in value (this statement is confirmed from a more accurate analysis directly done on the simulation post-processor). Increasing the pin height we exploit this delta, ensuring a better heat exchange to the re- refrigerant. As visible in Figure 6.73, the pins tips temperatures are all above 30°C in value (this statement is confirmed from a more accurate analysis directly done on the simulation post-processor).

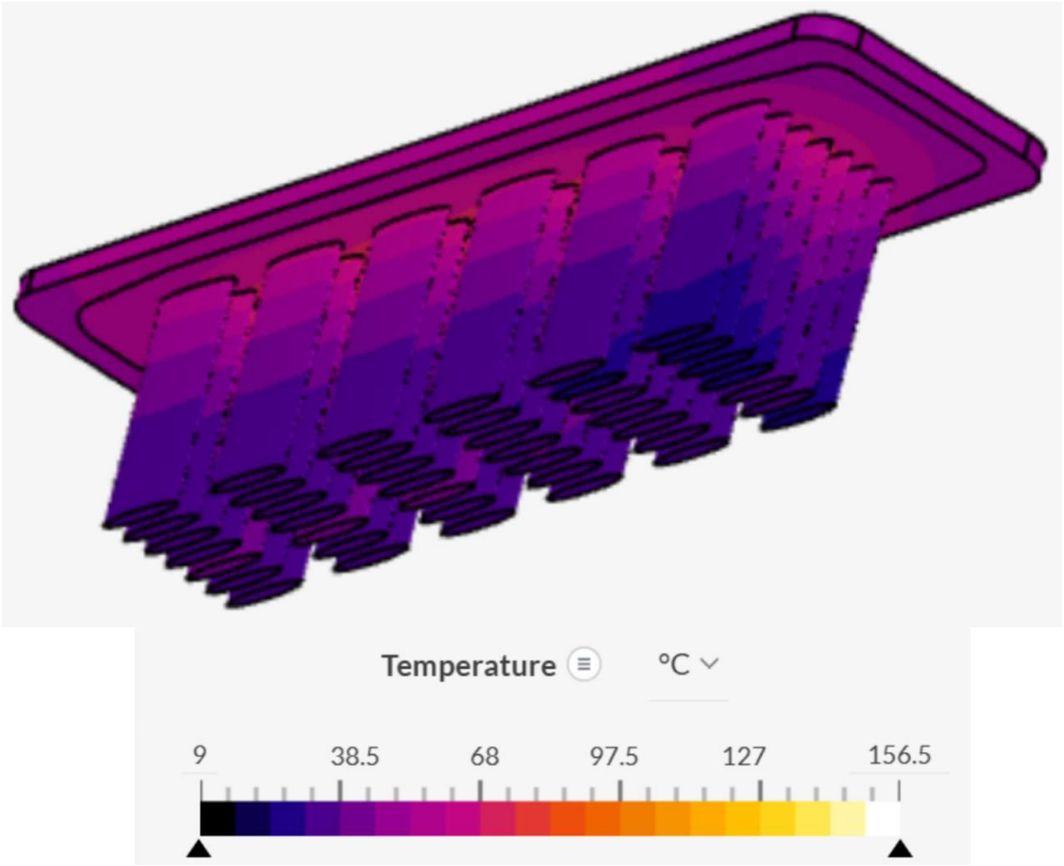

Figure 8.16: Cold plate temperature profile. R-134a refrigerant cooled final design.

Proceeding with the maximum Mosfet junction temperature, it's peak value was already displayed in Table 8.15. However a more detailed graphical result is reported on the next page.

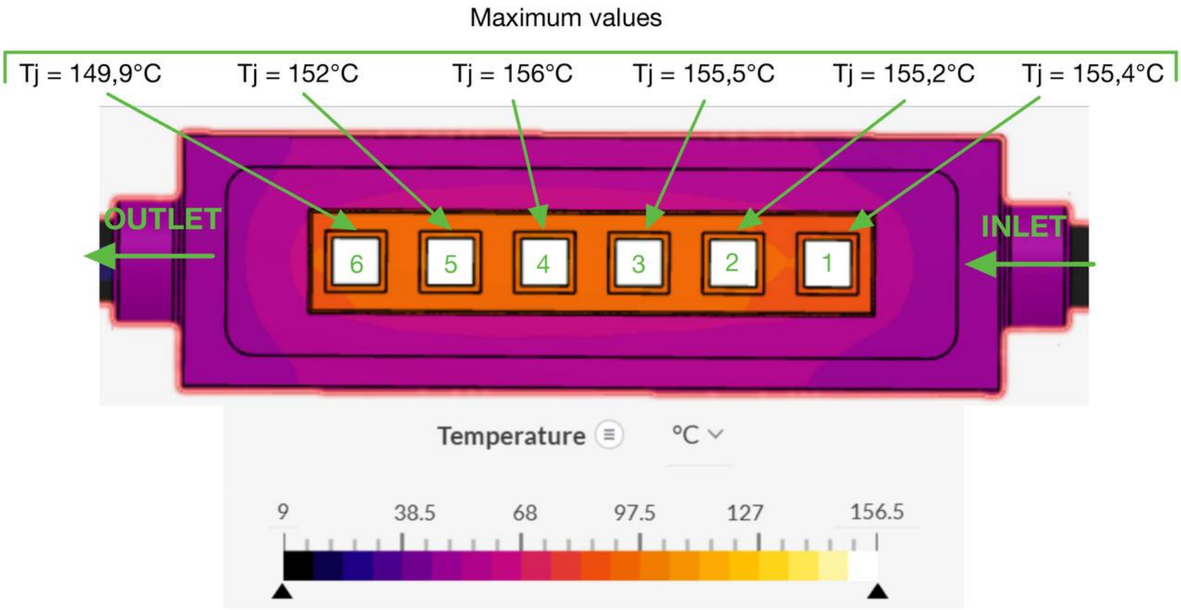

Figure 8.17: R-134a refrigerant cooling, maximum junction temperature.

While when it comes to pressure drop, hereafter the performances reached.

Inlet relative pressure	Outlet relative pressure	Final ΔP
1730,4 Pa	7,1 Pa	1723,3 Pa

It's clear how, in the face of a bigger channel and different pin design, the pressure drop is comparable to the one obtained in water-glycol case.

Water-glycol 50-50% final design ΔP	R-134a refrigerant final design ΔP	Comment
1790,3 Pa	1723,3 Pa	Read the text below the Table, a proper consideration is done.

However, in R-134a case, the peak T_{jmax} reached is higher compared to water-glycol case (146,6 °C for water-glycol vs 156 °C for R-134a). While this temperature is acceptable for the project's requirements, from a comparative standpoint it suggests that a more aggressive pin design could have been considered. This would likely have resulted in a slightly higher pressure drop but potentially lower maximum temperatures.

Once the simulation results are obtained, leveraging **SimScale post processor** it's possible to obtain important parameters.

In particular h parameter is estimated based on cold plate surface contact area and ΔT between cold plate and fluid.

Refrigerant	$T_{\text{fluid average}}$	$T_{\text{cold plate average (integral)}}$	$T_{\text{cold plate min}}$	$T_{\text{cold plate max}}$
R-134a	11,36°C	47,38°C	27,29°C	90,8°C

Table 8.17: R-134a simulation parameter results.

Thanks to data in Table 8.17, the following comparison can be done.

Refrigerant	Cold plate contact surface area	h theoretical	h simulation
R-134a	$\approx$ 0,043 m^2	947 $\frac{W}{m^2 \cdot K}$	387,4 $\frac{W}{m^2 \cdot K}$

Table 8.18: R-134a simulation vs theoretical parameter comparison.

As clearly visible in the above table, the theory remarkably overestimated the convection heat coefficient h. This is the reason why a way bigger cold plate surface area than expected is needed.

FINAL REMARK: The inverter cold plate is mounted radially with respect to the motor cooling jacket, which results in a 90° bend at the outlet of the channel. This bend serves to redirect the coolant flow toward the electric motor's cooling jacket. Since the bend design would be very similar to that shown in Figure 7.34, aside from the different cold plate configuration, these additional figures are not reported. This decision also aligns with the non-disclosure considerations previously discussed.

8.4 Sensitivity analysis

Sensitivity analysis is a powerful methodological tool used in engineering and scientific modelling to determine how changes in input parameters influence the outputs of a given system or model. Its primary objective is to identify which variables have the greatest impact on the results and to quantify the extent of that impact. By systematically varying input values within defined ranges, sensitivity analysis allows to prioritize design choices.

When applied to the specific application discussed in the dissertation, it enables to evaluate how changes in pressure drops, heat power to be dissipated or flow configurations affect the COP and overall refrigeration system performance. To recall the concepts already discussed in the previous section, the following qualitative image is proposed.

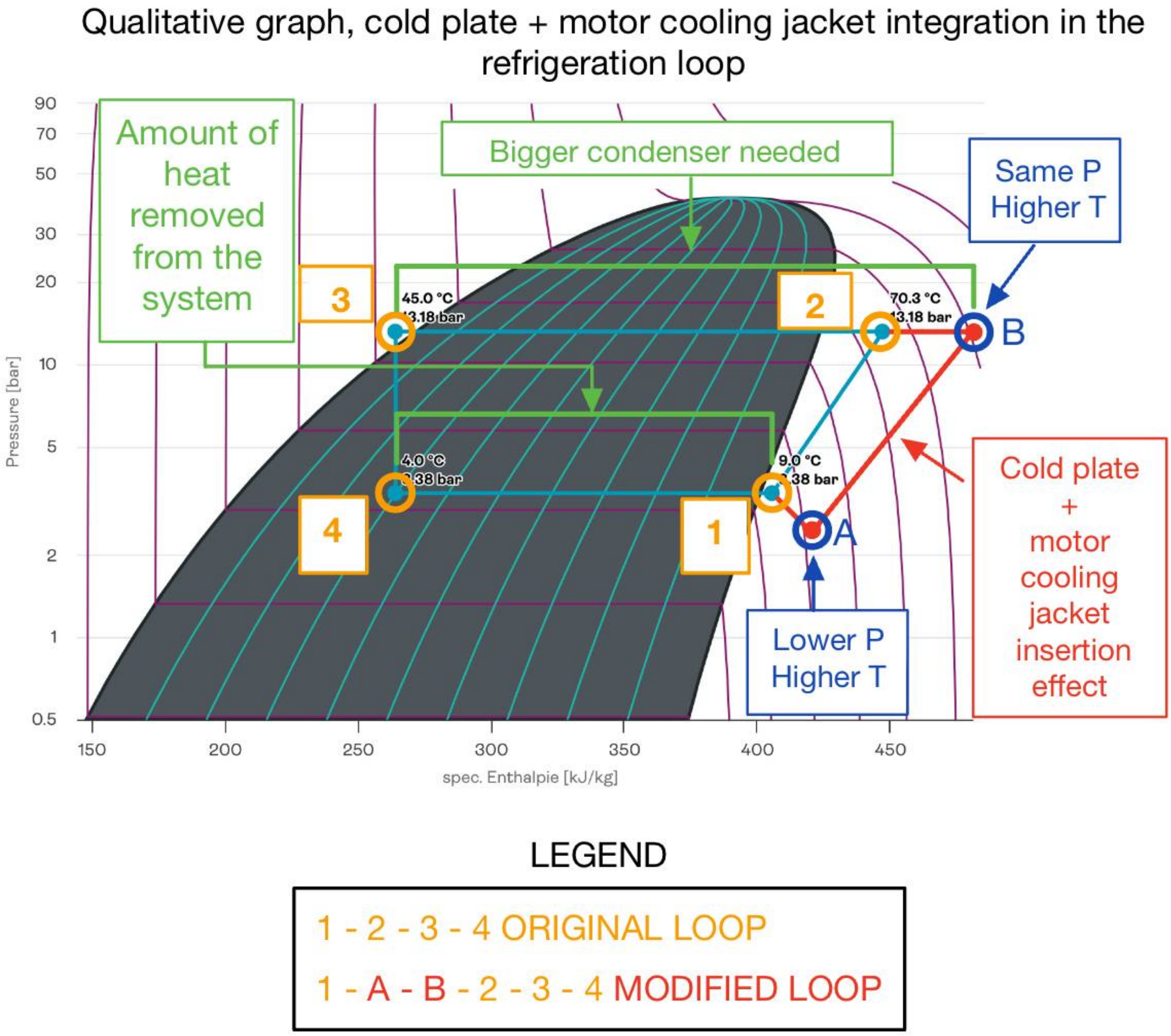

Figure 8.18: Inverter cold plate + electric motor cooling jacket integration in the refrigeration cycle effect.

Ultimately, sensitivity analysis can help quantifying the trade-offs between thermal performance improvements and potential penalties in hydraulic or thermodynamic efficiency, guiding the development of more effective and integrated thermal systems.

As highlighted in Figure 8.18, the two parameters affecting COP performances are: **pressure drop and thermal power to be dissipated**(because it determines the temperature increase of the fluid before the compression stage).

When both inverter and motor are refrigerant cooled, the system has the scheme pictured in Figure 5.6. As a consequence, to implement a sensitivity analysis the following simulation data at different compressor regimes are needed:

- Mass flow rate
- Electric motor cooling jacket pressure drop.
- Inverter cold plate pressure drop.
- Motor thermal power to be dissipated.
- Inverter thermal power to be dissipated.

Given that the data are strongly related to the compressor regime and consequently the compressor map and inverter working efficiencies, they are considered to be highly confidential. For this reason different working points (from the official one) in the compressor map were chosen. The related working conditions were found leveraging **PCHIP (Piecewise Cubic Hermite Interpolating Polynomial).**
It is a method of interpolation that constructs a smooth curve through a set of data points using piecewise cubic polynomials, while ensuring that the shape of the data is preserved; in particular its monotonicity and local behaviour.
Unlike standard cubic spline interpolation, which may overshoot or introduce unwanted oscillations between points (especially in non-smooth or monotonic data), PCHIP avoids such artifacts by adjusting the slopes of the cubic polynomials to match the trends in the data.

At Table 8.20, the respective data are reported for a 25kW compressor application at different regimes with R-134a refrigerant cooling.

Electric motor velocity (RPM)	**Mass Flow Rate (kg/s)**	**Interpolated motor pressure Drop (kPa)**	**Interpolated motor thermal power to be dissipated (kW)**	**Average inverter thermal power to be dissipated (W)**	**Total Thermal Power (W)**
122524	0,075	4,664	2,242	450	2692,3
123134	0,086	5,467	2,553	450	3003,4
123510	0,097	6,267	2,805	450	3254,9
123706	0,108	7,163	2,980	450	3430,2
123772	0,119	8,255	3,063	450	3512,6
120000	0,13	9,800	2,996	450	3446,6
116987	0,141	10,28	3,045	450	3495

Table 8.19: Compressor + inverter parameters at different working points in the map. Inverter integrated in the circuit, cooled down as the electric motor by 100% of the R-134a $\dot{m}$ circulating in the HVAC circuit. Data obtained through PCHIP interpolation of actual simulation data.

From the previous Table important average data values can be extrapolated. In addition, average ΔT of the refrigerant and inlet compression stage temperature can be found.

Average mass flow rate (kg/s)	**Average motor pressure drop (kPa)**	**Average motor thermal power to be dissipated (kW)**	**Average inverter thermal power to be dissipated (W)**	**Average total thermal power to be dissipated (W)**	**Average ΔT (°C)**	**Refrigerant T_{in} (°C)**	**Compression stage inlet T (°C)**
0.108	7,413	2.812	450	3262	33,28	9	42,28

Table 8.20: Average parameters, R-134a refrigerant cooled cold plate and electric motor jacket.

To keep the analysis as general as possible, many values of feasible inverter cold plate pressure drops were taken into account.

Here is the Table.

Inverter cold plate pressure drop ΔP [Pa]							
1500	1700	1900	2100	2500	2900	3300	3500

Table 8.21: Inverter cold plate pressure drop ΔP [Pa].

Without inserting cold plate and cooling jacket into the refrigeration loop, the R-134a conditions at the compressor inlet would be the following.

Point 1 in Figure 8.18 reference values.			
Pressure	Temperature	Q, enthalpy energy extrapolated through refrigeration	COP
3,38 bar	9 °C	141,6 KJ/Kg	3,4

Table 8.22: R-134a conditions at compressor inlet if cold plate and cooling jacket weren't inserted into the refrigeration loop.

Now, a look at the average pressure drop value in the cooling jacket at Table 8.20 and the possible inverter pressure drops values at Table 8.21 must be taken.
Starting from the "unperturbed" compressor inlet pressure (of 3,38 bar), the sum between average pressure drop in the cooling jacket and inverter pressure drop is subtracted. The new set of values of compressor inlet pressure is found. This set correspond to the possible compressor inlet pressure values when both cold plate and cooling jacket are integrated in the refrigeration loop.

The same is done with the temperature. Considering that the heat generated by both the inverter and the electric motor alters the refrigerant temperature before reaching the compression stage, a new working temperature is set. The value is already contained in Table 8.20. Once the new temperature and pressure values set are found, a new set of compressor inlet working conditions is defined.

To every single compressor inlet working condition an enthalpy value is associated. Considering the loop in Figure 8.2 (with a final outlet pressure of 13,18 bar), isentropic compression final enthalpy values are obtained. Considering a compression with efficiency equal to 0,7 non isentropic enthalpy values are calculated.

All the different steps are summarised in the following workflow scheme.

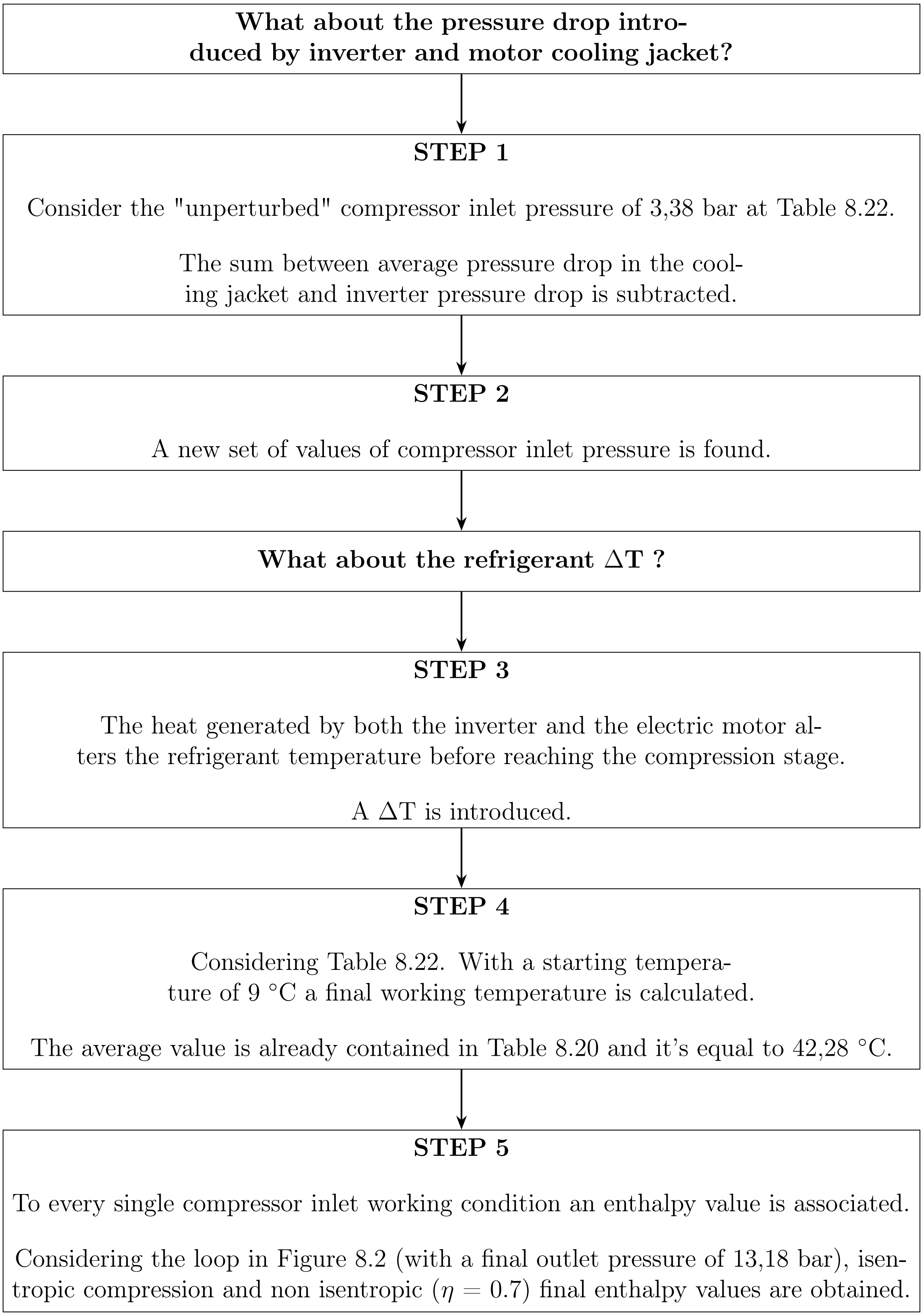

What about the pressure drop introduced by inverter and motor cooling jacket?

STEP 1

Consider the "unperturbed" compressor inlet pressure of 3,38 bar at Table 8.22.

The sum between average pressure drop in the cooling jacket and inverter pressure drop is subtracted.

STEP 2

A new set of values of compressor inlet pressure is found.

What about the refrigerant ΔT ?

STEP 3

The heat generated by both the inverter and the electric motor alters the refrigerant temperature before reaching the compression stage.

A ΔT is introduced.

STEP 4

Considering Table 8.22. With a starting temperature of 9 °C a final working temperature is calculated.

The average value is already contained in Table 8.20 and it's equal to 42,28 °C.

STEP 5

To every single compressor inlet working condition an enthalpy value is associated.

Considering the loop in Figure 8.2 (with a final outlet pressure of 13,18 bar), isentropic compression and non isentropic ($\eta = 0.7$) final enthalpy values are obtained.

Figure 8.19: Initial steps workflow for refrigerant cooled inverter sensitivity analysis.

Given the pressure value set and the inlet compression stage, enthalpies for every (P,T) coordinate can be found on the p-h diagram.

To obtain proper data **GT-SUITE software** was used. "GT-SUITE is a simulation tool with capabilities and libraries aimed at a wide variety of applications and industries. It offers engineers functionalities ranging from fast concept design to detailed system or sub-system/component analyses, design optimization, and root cause investigation" [38].
The data were provided by inserting two blocks (one dedicated to the starting point of the compression and one to the ending point), simulating both for isentropic and non-isentropic compression ($\eta = 0.7$).
The results are organised in the Table that follows.

R-134a enthalpy values for different pressure operating points at constant temperature of 42,28 °C.				
Final Inlet pressure (electric motor + inverter pressure drop)	3,291 bar	3,289 bar	3,287 bar	3,285 bar
h_A **before compression (kJ/kg)**	435,8	435,8	435,8	435,8
h_{Bis} **after compression (kJ/kg)**	470,6	470,6	470,7	470,7
h_{Breal} **after compression (kJ/kg)**	485,5	485,6	485,6	485,6
Final Inlet pressure (electric motor + inverter pressure drop)	3,281 bar	3,277 bar	3,273 bar	3,271 bar
h_A **before compression (kJ/kg)**	435,8	435,8	435,8	435,8
h_{Bis} **after compression (kJ/kg)**	470,7	470,8	470,8	470,8
h_{Breal} **after compression (kJ/kg)**	485,7	485,7	485,8	485,8

Table 8.23: Inlet and outlet enthalpy values for both isentropic and non-isentropic compression (η = 0,7). Compressor outlet pressure value equal to 13,18 bar.

Once the enthalpy values are known, recalling that:

$$COP = \frac{Q}{h_{2real} - h_1}$$

The COP is calculated in correspondence of every single case.

COP values for different inlet pressures at constant temperature of 42,28 °C				
Inlet Pressure [Bar]	3,291	3,289	3,287	3,285
COP	2,8452	2,8438	2,8423	2,8409
Inlet Pressure [Bar]	3,281	3,277	3,273	3,271
COP	2,8380	2,8351	2,8323	2,8308

Table 8.24: COP values for varying inlet pressure at constant temperature (42,28 °C).

Recalling the reference values where the unperturbed compressor inlet conditions are contained, the pressure and consequent COP percentage variation can be calculated. For sake of simplicity the Table is reported again.

Point A in Figure 8.18 reference values.			
Pressure	Temperature	Q, enthalpy energy extrapolated through refrigeration	COP
3,38 bar	9 °C	141,6 KJ/Kg	3,4

Table 8.25: R-134a conditions at compressor inlet if cold plate and cooling jacket weren't inserted into the refrigeration loop.

The sensitivity values (how much a modification of a parameter in input affects a parameter in output) is obtained through the following relationship.

$$\text{Sensitivity (\%)} = \left(\frac{\text{Percentage variation of the output}}{\text{Percentage variation of the input}} \right) \cdot 100$$

Leveraging this formula it's possible, keeping in mind the reference values in Table 8.25, the following sensitivity values.

COP and sensitivity values for decreasing inlet pressure				
Variation of the Inlet Pressure [%]	-2,637%	-2,696%	-2,755%	-2,815%
COP variation	-16,32%	-16,36%	-16,40%	-16,44%
Sensitivity (%) w.r.t pressure	618,8%	606,8%	595,3%	584,3%
Variation of the Inlet Pressure [%]	-2,933%	-3,051%	-3,170%	-3,229%
COP variation	-16,53%	-16,61%	-16,70%	-16,74%
Sensitivity (%) w.r.t pressure	563,6%	544,5%	526,8%	518,5%

Table 8.26: COP and sensitivity for decreasing inlet pressure.

As highlighted from the Table, the percentage values vary around the same values more or less. It would be more useful to have a unique picture by calculating the average of such percentages.

Average values of Table 8.26	
Variation of the Inlet Pressure [%]	-2,911%
COP variation	-16,51%
Resulting sensitivity (%) w.r.t pressure	567,3%

Table 8.27: Average sensitivity value for decreasing inlet pressure values.

What if instead of varying the pressure, an average pressure value is assumed and the varying parameter becomes the compressor inlet temperature?

The average of pressure values contained in Table 8.23 is equal to: **3,271 bar**.
Keeping the pressure constant and varying the temperature between 24°C and 42,28°C the following data are obtained.

R-134a enthalpy values for different temperatures at constant inlet pressure of 3,271 Bar				
Reference temperature before compression (°C)	24	27	29	30
h1 before compression (kJ/kg)	419,2	421,9	423,7	424,6
h2is after compression (kJ/kg)	451,5	454,6	456,7	457,8
h2real after compression (kJ/kg)	465,3	468,6	470,9	472,0
Reference temperature before compression (°C)	34	37	40	42,28
h1 before compression (kJ/kg)	428,3	431,0	433,7	435,8
h2is after compression (kJ/kg)	462,0	465,1	468,3	470,7
h2real after compression (kJ/kg)	476,4	479,8	483,1	485,7

Table 8.28: Reference temperatures and enthalpy values for R290 (excluding 33 °C).

Exactly as before the COP values are found.

COP values for different inlet temperatures at constant pressure of 3,271 Bar				
Inlet Temperature [°C]	24	27	29	30
COP	3,0750	3,0322	3,0046	2,9911
Inlet Temperature [°C]	34	37	40	42,28
COP	2,9386	2,9008	2,8642	2,8380

Table 8.29: COP values for varying inlet temperature at constant pressure (3,271 Bar).

Recalling the reference values in Table 8.25, the sensitivity analysis is developed...

COP and sensitivity values for different inlet temperature variations at constant pressure of 3,271 Bar				
Variation of the Inlet Temperature [%]	166,7%	200,0%	222,2%	233,3%
COP variation	- 9,560%	- 10,82%	- 11,63%	- 12,03%
Sensitivity (%) w.r.t temperature	- 5,736%	- 5,409%	- 5,233%	- 5,154%
Variation of the Inlet Temperature [%]	277,8%	311,1%	344,4%	369,8%
COP variation	- 13,57%	- 14,68%	- 15,76%	- 16,53%
Sensitivity (%) w.r.t temperature	- 4,886%	- 4,720%	- 4,575%	- 4,470%

Table 8.30: COP and sensitivity for increasing inlet temperature (without 266,7%).

The following average values results from the analysis.

Average values of Table 8.26	
Variation of the inlet temperature [%]	265,8%
COP variation	- 13,08%
Resulting sensitivity (%) w.r.t temperature	- 4,923%

Table 8.31: Average sensitivity value for decreasing inlet pressure values.

To better highlight the analysis conclusion:

- A graphical visualization of results is proposed.
- Calculation of COP reduction based on average cooling jacket pressure drop and final cold plate R-134a ΔP is proposed.

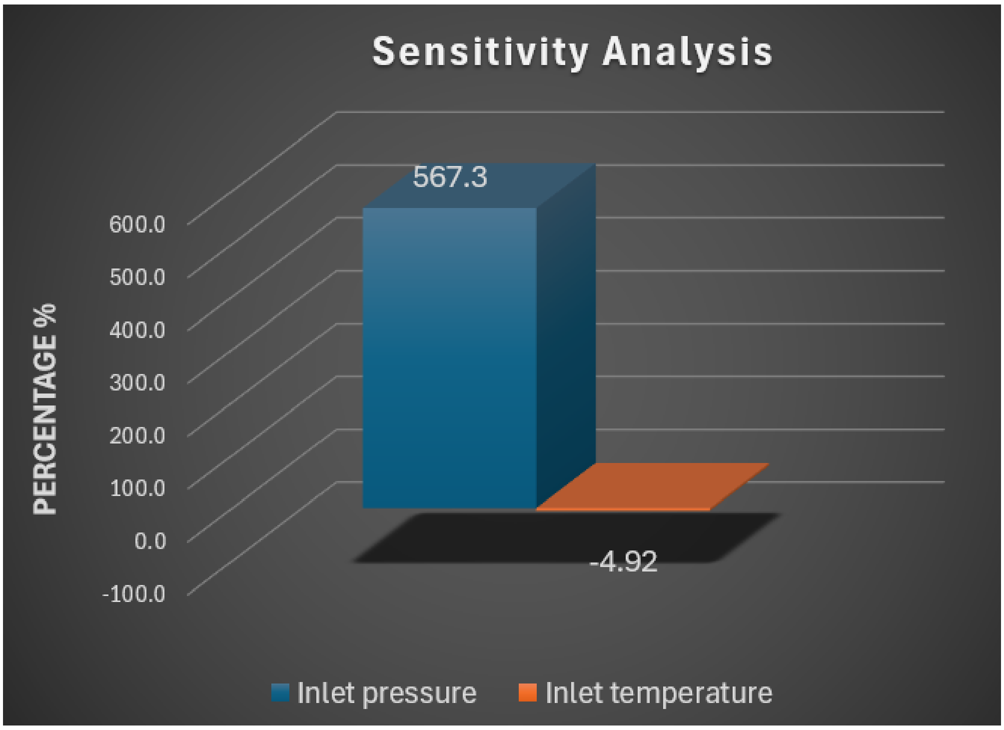

Figure 8.20: Pressure vs temperature sensitivity comparison.

When compared with temperature sensitivity value, it immediately stands out how **pressure has the main influence on COP variation**. As a consequence, when defining project constraints, particular care must be taken to limit the maximum allowable pressure drop. This is especially critical in the Garrett Motion product, where only the compression system is supplied to the final customer. It's essential to minimize its impact on the overall system performance.

Based on the data used for the analysis and the cold plate performance, the COP reduction of the R-134a cooling system due to the pressure drop is estimated.

Refrigerant	**Average motor cooling jacket ΔP**	**Final cold plate design (Figure 8.13) ΔP**	**Hypothesised ΔP due to the 90° bend**	**Total ΔP**
R-134a	7413 Pa	1723,3 Pa	1000 Pa	10136,3 Pa

Table 8.32: Total pressure drop due to the cold plate integration within refrigeration cycle calculation.

Recalling that the inlet cold plate pressure is equal to 3,38 bar.

Total ΔP (calculated in % w.r.t inlet 3,38 bar)	**COP variation**
- 2,99 %	- 17%

Table 8.33: Refrigeration cycle efficiency drop due to additional ΔP.

A 17% drop in refrigeration efficiency cycle would be expected.

9 R290 (Propane) refrigerant cooling

9.1 Introduction

The rapid evolution of new energy vehicles (NEVs) has introduced a unique set of challenges and opportunities in the design and operation of automotive HVAC systems. As environmental regulations tighten up and consumer demand for sustainable technologies grows, the choice of refrigerants has become a critical factor in the development of efficient and eco-friendly thermal management solutions. Traditional refrigerants such as R134a, while widely used, are increasingly put under analysis due to their global warming potential (GWP) and environmental impact [39].

In response, new refrigerants solutions have emerged as promising alternatives. These substances offer varying advantages in terms of environmental sustainability, raising up thought new technical challenges. New aspects must be taken into account and new precautions must be adopted. Among the available options, R290 (commonly known as propane) emerges as a particularly promising choice, as confirmed by the customer's interest in it.
The following tables present a comparison of key parameters between R-290 and the previously analyzed refrigerant R-134a.

Refrigerant type	**Environmental (GWP)**	**Flammability**	**Toxicity**
R-134a	1430 (High)	Non-flammable (ASHRAE A1).	Despite low toxicity, asphyxiation hazard if leaked into vehicle cabin.
R290	3 (Ultra low)	Flammable (ASHRAE A3). Requires explosion-proof design.	Despite low toxicity, asphyxiation hazard if leaked into vehicle cabin.

Table 9.1: Comparison of R-134a and R290 in terms of environmental impact, flammability, and toxicity [39].

Refrigerant type	**Thermal performances**	**Rubber seal requirements**	**Cost**
R-134a	Proper cooling performances	Normal high pressure resistance sealing.	Low system cost.
R290	Superior cooling efficiency (higher c_p)	R290's hydrocarbon nature necessitates oil-resistant seals to prevent swelling.	Low refrigerant cost. High safety system cost.

Table 9.2: Comparison of R-134a and R290 in terms of thermal performance, material compatibility, and cost implications [39].

Keeping in mind the just above shown concepts the following remarks can be done.

REMARKS		
Refrigerant	**Regulatory info**	**Technical notes**
R290	Environmentally preferred. Max charge limit: 150g (ISO 13043)	Cost-effective refrigerant but requires purer grades ($\geq$99.5%) and explosion-proof infrastructure.
R-134a	Going to be banned in EU from 2030. GWP exceeds EU F-Gas Regulation limits.	Mature supply chain but facing phase-down due to high GWP.

Table 9.3: Comparison between R290 and R-134a in terms of regulatory and technical aspects [39].

In light of a potential EU ban on R-134a, propane emerges as a promising alternative worth investigating. Refrigerant parameters depend on the operating point in the refrigerant cycle (P and T).

9.2 Project constraints

To keep the comparison as fair as possible, the same refrigeration cycle as before are taken into consideration.

Condensation Temp.	**Evaporation Temp.**	**Superheating**	**Subcooling**	**Comp. Efficiency**
50 °C	4 °C	5 °C	5 °C	0.7

Table 9.4: Refrigeration cycle parameters for R290.

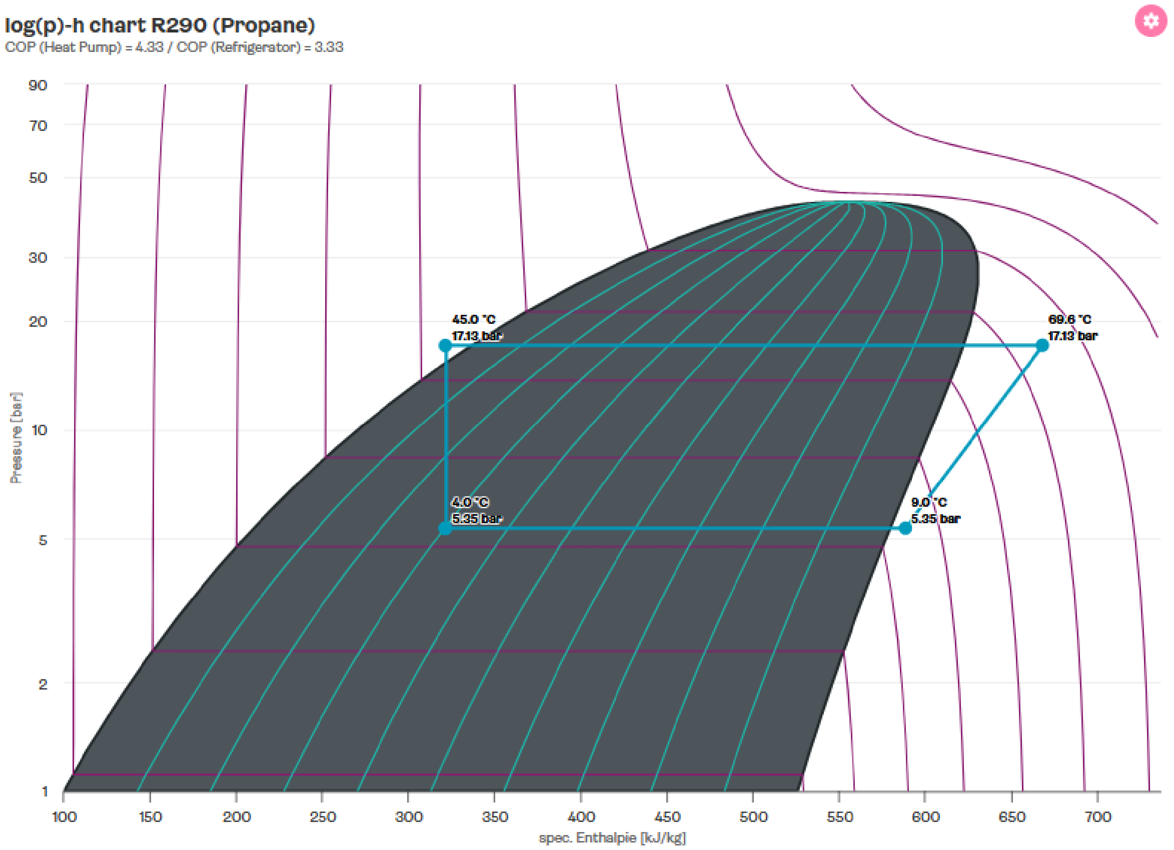

Figure 9.1: log ph chart, R290 refrigerant at cycle working conditions [37].

Refrigerant	**Compression stage, Inlet absolute pressure**	**Compression stage, inlet T**
R290	5.35 bar	9.0 °C

Table 9.5: Compression stage, inlet constraints for R290 refrigerant.

IMPORTANT REMARK

Differences in compressor inlet and outlet pressures have a direct impact on compressor design. Therefore, while this dissertation focuses on comparing different cooling approaches, it is important to highlight that the compressor design for R290 and R-134a refrigerants is not the same. Varying operating pressures and pressure ratios, influence the shape of the compression wheel. It results in differences in compressor efficiency (η), affecting the overall system analysis. However, for consistency, the same constraints are applied, and compressor efficiency is assumed to be equal in both cases.

9.3 Theoretical approach

At the operating point in Table 9.5, the R290 displays the following characteristics.

Parameter at 9°C	R290 (At 5,35 bar)	R-134a (At 3,38 bar)	Comment
ρ (Kg/m^3)	11,33 [38]	16,160 [38]	Lower density values for R290.
μ (Pa·s)	$7{,}71 \cdot 10^{-6}$ [38]	$1{,}108 \cdot 10^{-5}$ [38]	A one order of magnitude lower dynamic viscosity results in a higher Reynolds number for R290.
c_p (J/(Kg·K))	1779,3 [38]	907,510 [38]	R290 higher specific heat means it's equal to a higher quantity of heat absorbed per unit mass.
K (W/m·K)	$1{,}77 \cdot 10^{-2}$ [38]	$1{,}230 \cdot 10^{-2}$ [38]	R290 higher thermal conductivity translates in a slightly lower difficulty in heat transfer through the gas.
ν (m^2/s)	$6{,}81 \cdot 10^{-7}$ [38]	$6{,}863 \cdot 10^{-7}$ [38]	Comparable kinematic viscosity between the two.

Table 9.6: Comparison between R290 and R-134a at 9°C.

As developed for R-134a refrigerant, the same numerical approach can be applied to R290 analysis.

The data were found as follows:

- Leveraging the equations in Table 8.8.
- The target $\overline{v}$ is always equal to 15m/s.

- The chosen geometry type takes reference from Figure 8.10 and 8.11.
  As R-134a design, it is characterized by 7 elliptical pins under every Mosfet.

Right below the parameters found.

Fluid	Study case $\dot{m}$	Calculated $\overline{A}$	Actual $\overline{A}$	$\overline{P}$	$\overline{D_h}$
R290	0.140 kg/s	824,5 $\cdot 10^{-6}$	837,2 $\cdot 10^{-6}\ m^2$	591,6 $\cdot 10^{-3}\ m$	5,66 $\cdot 10^{-3}\ m$

Table 9.7: R290 geometry parameters calculation. The channel design reference is the one depicted in Figure 8.10 and 8.11.

Fluid	$\overline{v}$	Pr	Re	h	Flow type
R290	15 (m/s)	1,18	$1,25 \cdot 10^5$	1431 $\frac{W}{m^2 \cdot K}$	TURBULENT

Table 9.8: R290 geometry parameters calculation. Theoretical results.

Recalling equation number 8.2 the area ratio when shifting from water-glycol cooling to R290 refrigerant cooling should be the following.

$$\boxed{\frac{A_{\text{contact 2}}}{A_{\text{contact 1}}} \leq 3,12}$$

Where $A_{contact2}$ is the R290 cold plate surface contact area.

It immediately stands out how R290 refrigerant is supposed to necessitate a lower surface contact area w.r.t R134a refrigerant. This, of course, is a reflection of the higher h value for R290.

Refrigerant	h coeff (theoretical).	$A_{contact2}$
R290	1431 $\frac{W}{m^2 \cdot K}$	$\leq$ 3,12 $A_{contact1}$
R-134a	947 $\frac{W}{m^2 \cdot K}$	$\leq$ 4,56 $A_{contact1}$

Table 9.9: R290 vs R-134a theoretical parameters comparison.

As in the case of R-134a, the theoretical upper limit of R-290's contact surface will not be validated when coming to actual simulation. It's useful though to trace the path to be followed and base the design development on proper theoretical foundations.

9.4 Final design

When developing the new cold plate design the following two choices were taken:

- **1)** The contact surface area was kept the same as the final cold plate design of R-134a refrigerant cooling (see Figure 8.15).
- **2)** The distance between the pins was increased, positioning them further from the center of the heat source. This less optimal pin placement was compensated by a higher heat transfer coefficient h and by adopting choice "1", which maintained the contact surface area.

The final channel shape doesn't have evident changes, if not in terms of increased cross section area (because of the higher volume flow rate) and increased pin spacing.

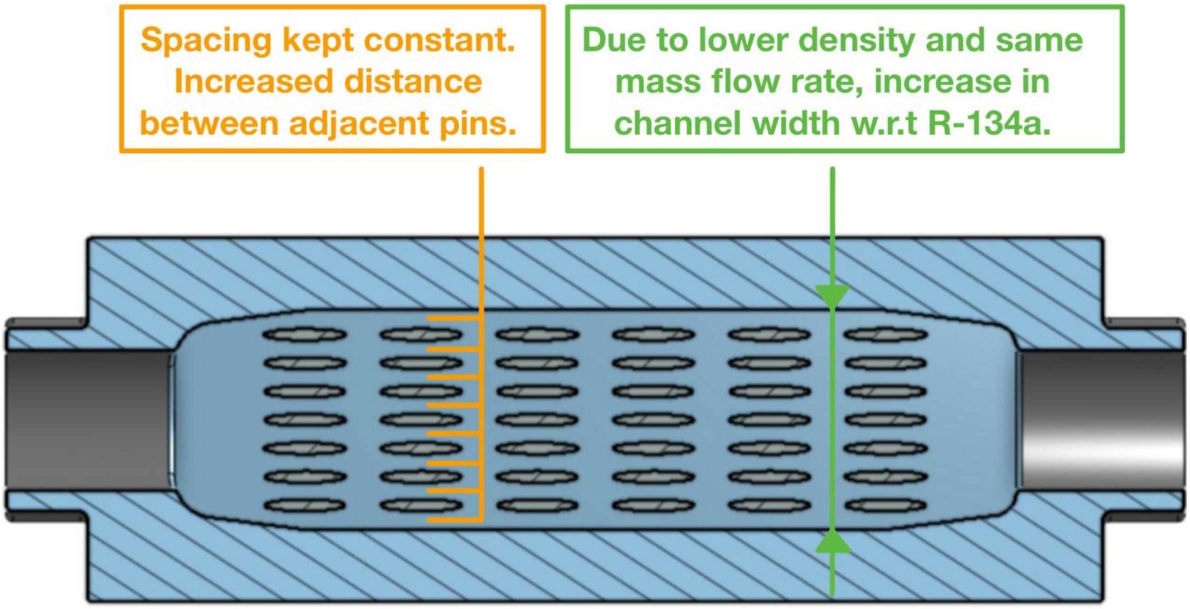

Figure 9.2: Final design. R290 cooling channel cross section top view.

Through simulation the additional spacing revealed to be beneficial from the pressure drop point of view, allowing anyway to hit the target T_{jmax} of 150 °C.

However, besides the slightly modified design, a lower pressure drop was already expected compared to R-134a case. The comparison Table on the next page summarizes the reasons behind the statement.

Refrigerant	R-134a	R290	**Comment**
Pressure drop ΔP	1723,3 Pa (actual)	Lower than R-134a (expected)	$\Delta P = f \cdot L \cdot \frac{8\rho Q^2}{\pi^2 D_h^5}$ • Q has a big impact on ΔP (quadratic), but D_h has a fifth power influence. • For higher Re, friction factor f is expected to be lower.
Density ρ	16,16 kg/m^3	11,33 kg/m^3	
Volume flow rate $\dot{V}$ (same $\dot{m} = 0.14$ kg/s)	519,80 L/min	742,05 L/min	
Re number (theoretical)	$8{,}92 \cdot 10^4$	$1{,}23 \cdot 10^5$	
Hydraulic diameter D_h	0,0040 m	0,0056 m	

Table 9.10: R290 vs R-134a comparison, lower R290 pressure drop expectation reasons.

The fluid when travelling through the channel displays the following behaviour.

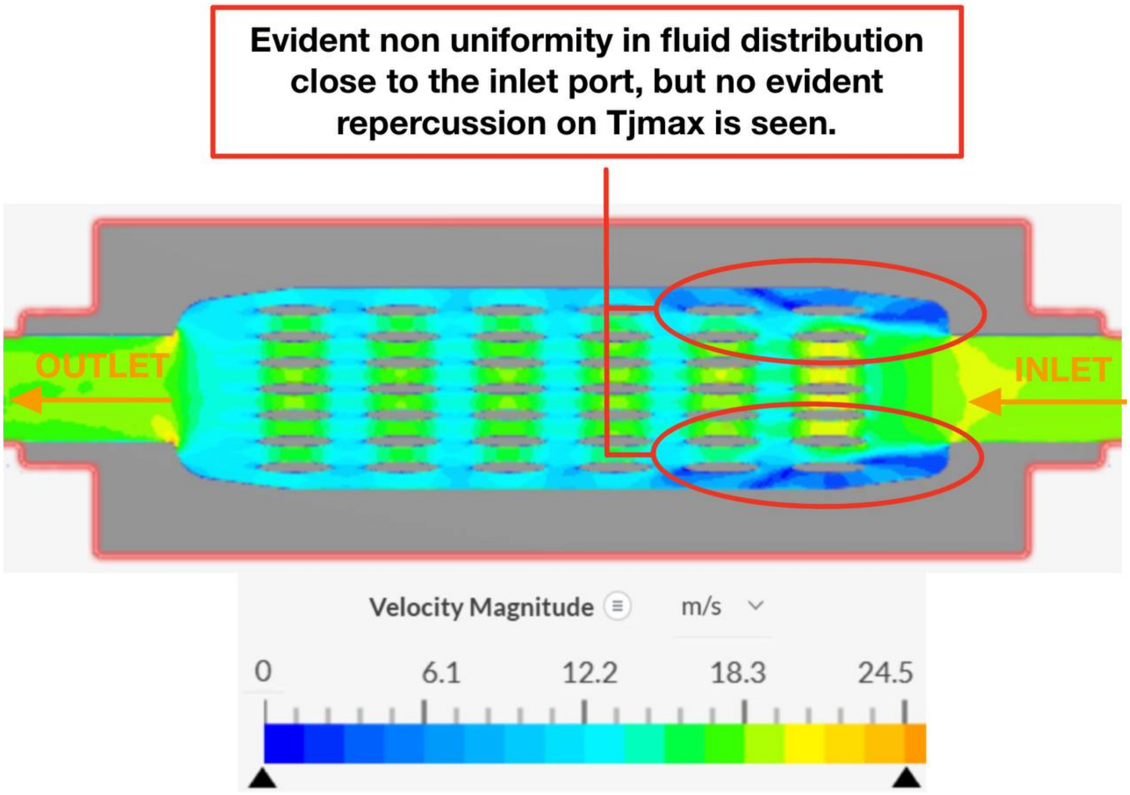

Evident non uniformity in fluid distribution close to the inlet port, but no evident repercussion on Tjmax is seen.

Figure 9.3: R290 cooling channel velocity magnitudes. Final design.

The design dimensions are displayed in the following images (next page).

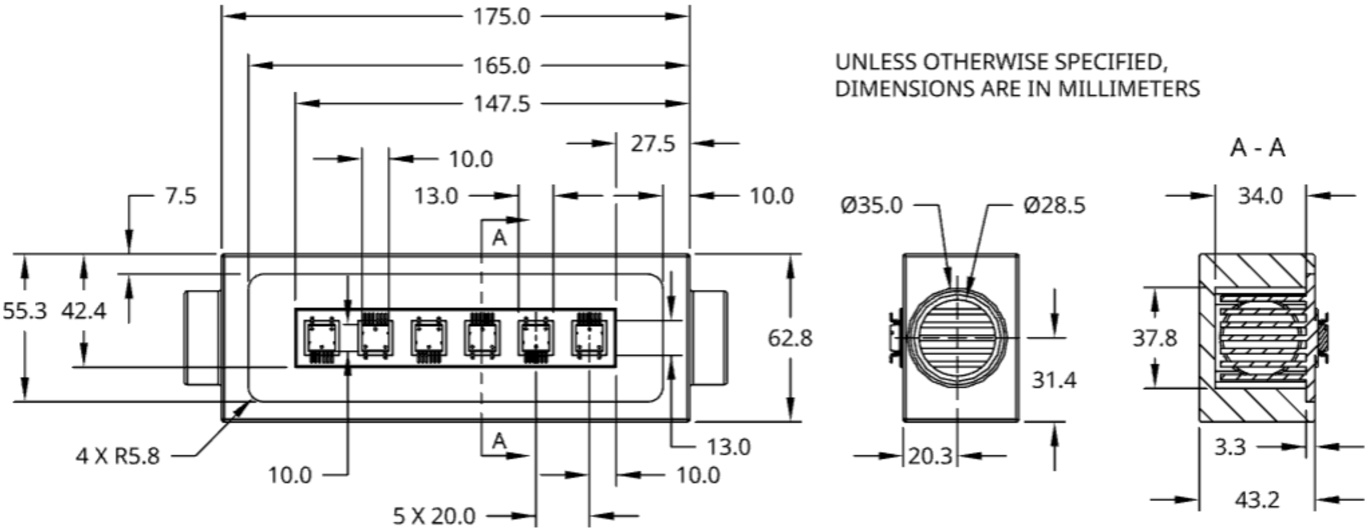

Figure 9.4: R290 final design, quotation.

Paying attention to the different projections, it's evident how it was necessary to increase the channel dimensions as well as the inlet/outlet one.

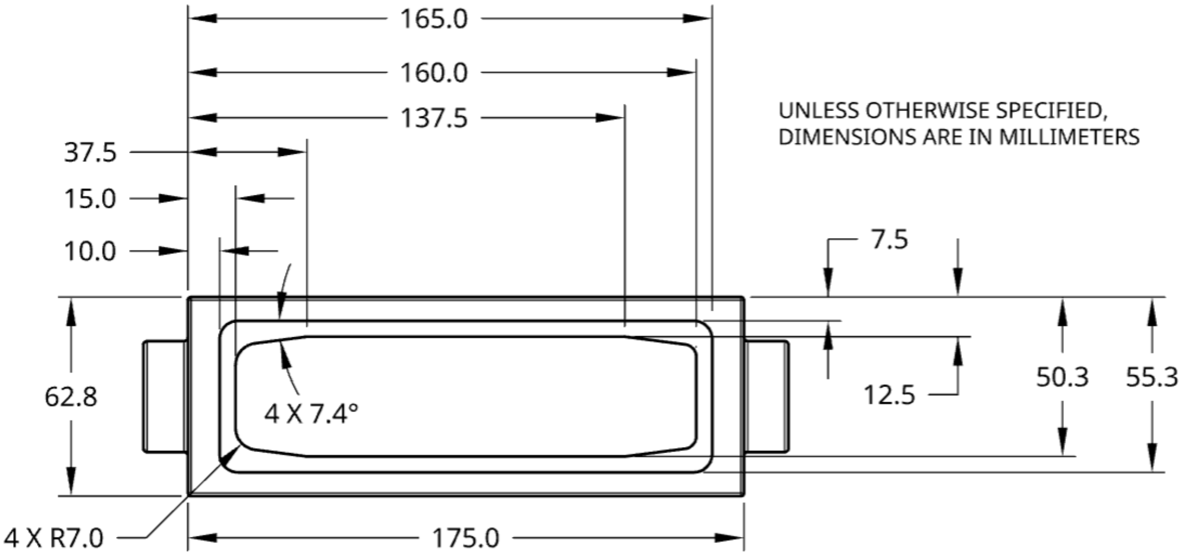

Figure 9.5: R290 final cooling channel design, quotation.

About the specific cold plate pins design.

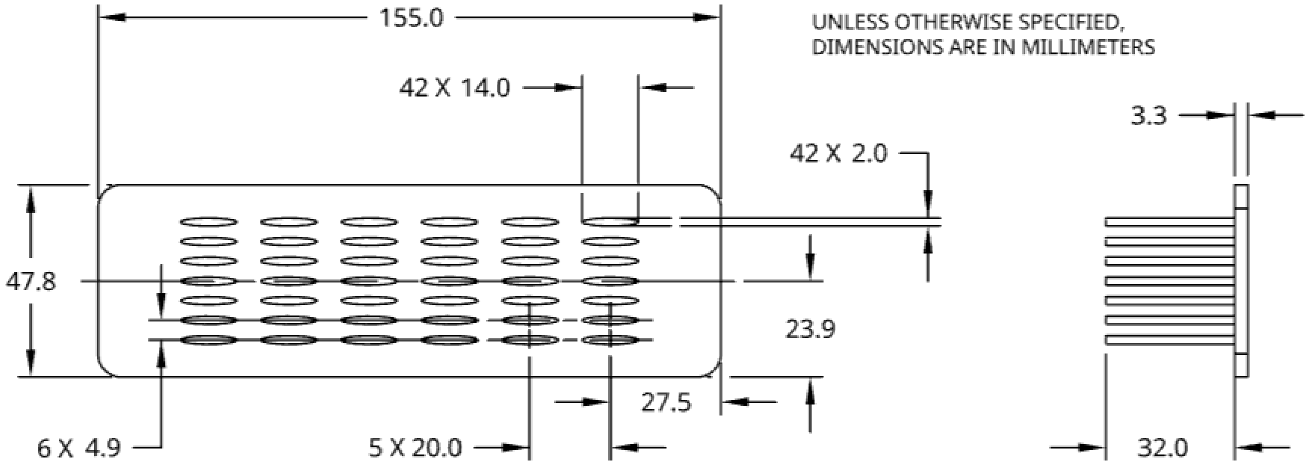

Figure 9.6: R290 cold plate pins final design, quotation.

An increased spacing between pins can be noticed w.r.t R-134a design (4,9 mm vs 3,5 mm). As previously mentioned this choice allowed to partially reduce the pressure drop for this application while meeting the required performances.

The pin height is the same of R-134a case. The choice is dictated by the design decisions taken and the common inlet refrigerant temperature set to 9°C.

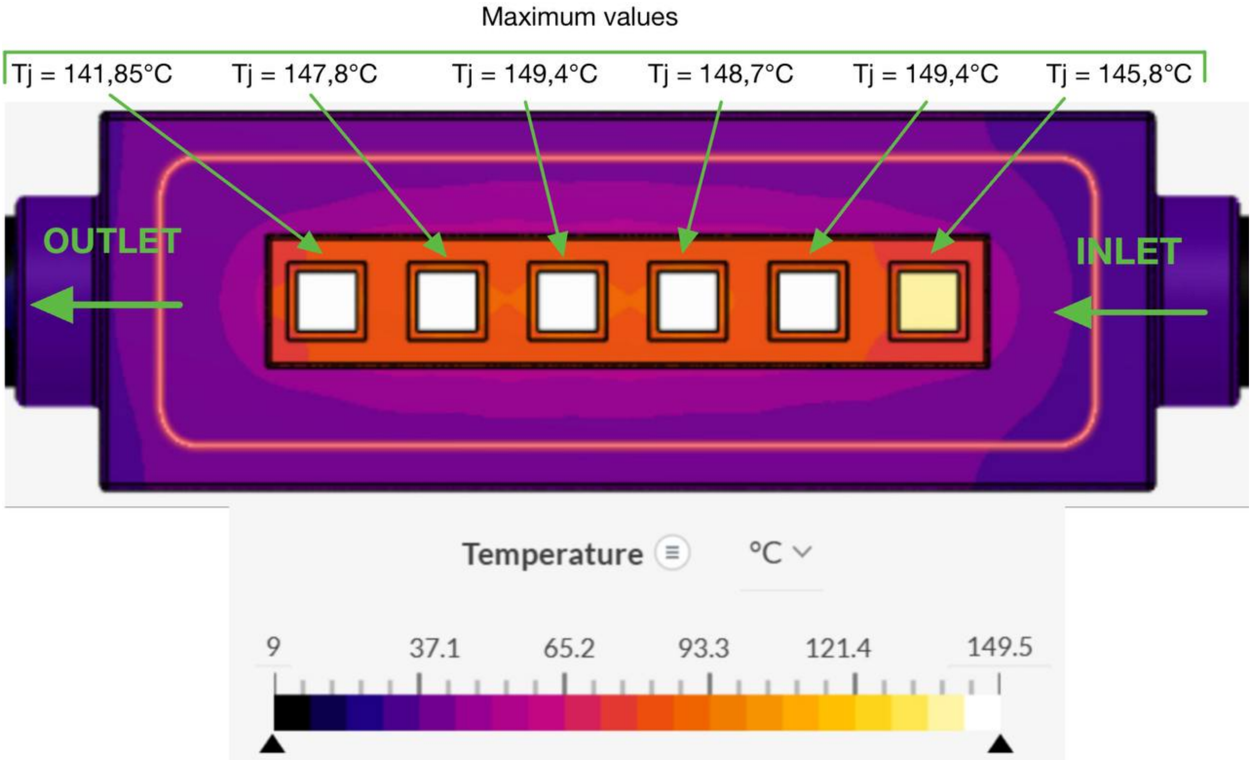

Figure 9.7: R290 refrigerant cooling, maximum junction temperature.

In Figure 9.7 the different Mosfet junction temperatures are reported. They are all comprised under the target T_j of 150 °C. Given that the cold plate design is really similar to the R-134a one, the much lower T_j confirm the higher R290 cooling efficiency.

When it comes to pressures, the following values are obtained.

Inlet relative pressure	Outlet relative pressure	Final ΔP
1305,8 Pa	5,1 Pa	1300,7 Pa

From the just above result it's clear how, in the face of a bigger channel and different pin placement, the pressure drop is remarkably decreased w.r.t both water-glycol and R-134a case.

Water-glycol 50-50% final design ΔP	R-134a refrigerant final design ΔP	R290 refrigerant final design ΔP	Comment
1790,3 Pa	1723,3 Pa	1300,7 Pa	The lower R290 ΔP was already justified at Table 9.10

As revealed by the sensitivity analysis in section 8.4, the pressure drop reveals to be a key parameter for refrigerant cooling. The COP of the refrigeration cycle is greatly affected by it.

The R290 lower pressure drop can be considered extremely valuable, even at the expense of a slightly bigger cold-plate (and cooling jacket) because of the higher volume flow rate.

Once the simulation results are obtained, leveraging **SimScale post processor** it's possible to obtain important parameters. In particular h parameter is estimated based on cold plate surface contact area and ΔT between cold plate and fluid.

Refrigerant	$T_{\text{fluid average}}$	$T_{\text{cold plate average (integral)}}$	$T_{\text{cold plate min}}$	$T_{\text{cold plate max}}$
R290	10,20°C	35,84°C	18,38°C	82,49°C

Table 9.11: R290 simulation parameter results.

Refrigerant	Cold plate contact surface area	h theoretical	h simulation
R290	$\approx$ 0,044 m^2	1431 $\frac{W}{m^2 \cdot K}$	531,2 $\frac{W}{m^2 \cdot K}$

Table 9.12: R290 simulation vs theoretical parameter comparison.

As clearly visible in the above table, the theory remarkably overestimated the convection heat coefficient h. This is the reason why a way bigger cold plate surface area than expected is needed.

FINAL REMARK: The inverter cold plate is mounted radially with respect to the motor cooling jacket, which results in a 90° bend at the outlet of the channel. This bend serves to redirect the coolant flow toward the electric motor's cooling jacket. Since the bend design would be very similar to that shown in Figure 7.34, aside from the different cold plate configuration, these additional figures are not reported. This decision also aligns with the non-disclosure considerations previously discussed.

10 Conclusion

10.1 Technology comparison

With the analysis coming to an end, proper comparison between technologies is done. The comparative features are those recurring throughout the various sections:

- Pressure drop ΔP.
- Junction temperature T_j.
- Occupied volume.

Based on the collected data, the following comparative table was compiled.

Fluid	**Water-Glycol 50-50%**	**R-134a**	**R290**	**Comment**
Pressure drop ΔP	1790,3 Pa	1723,3 Pa	1300,7 Pa	R290 shows the lowest pressure drop, indicating better flow characteristics.
Max. $\mathrm{T_j}$ reached	146,6 °C	156 °C	149,4 °C	R-134a shows to be less efficient in cooling between the three.
Channel occupied volume	0,171 L	0,406 L	0,475 L	Water-Glycol is the most space-efficient.
Pin shape	Elliptical, 2:1 ratio	Elliptical, 7:1 ratio	Elliptical, 7:1 ratio	Sharper pins (7:1) for refrigerants, higher aerodynamical shape.

Table 10.1: Final design comparison, three different cooling approaches.

IMPORTANT REMARK

The reported volume values in Table 10.1 refer solely to the cold plate itself. In the case of water-glycol cooling, the total system volume would be significantly larger due to the need for an external circuit and its associated components.

In light of the previous remark, the water-glycol technology proves to be of limited interest. Besides the larger space requirement, it offers similar T_j performance with a higher pressure drop.

At this point the comparison can be limited to the refrigerant cooling technology. In terms of cooling performances and pressure drop, the R290 cooling proves to be the best option. The occupied volume is just above the R-134a technology, however it comes with a cost too.

Fluid	**Water-Glycol 50-50%**	**R-134a**	**R290**
Fluid inlet absolute P	1,03 bar	3,38 bar	5,35 bar

Table 10.2: Comparison of fluid inlet absolute pressure.

Refrigerants operate under significantly higher pressures. Stricter mechanical constraints and attention to leakage problems must be tackled. This factors can have great impact on both product shape, manufacturing cost and raise safety concerns.

The remaining evaluations are summarized in the following Table.

Fluid	**Water-Glycol 50-50%**	**R-134a**	**R290**	**Comment**
Contact surface area	6,28 $\cdot 10^{-3}$ m^2	43,25 $\cdot 10^{-3}$ m^2	44,06 $\cdot 10^{-3}$ m^2	Much higher surface area for refrigerants, aiding heat transfer.
Relative contact surface	A_1	$\approx\ 7 \cdot A_1$	$\approx\ 7 \cdot A_1$	Order of magnitude comparison.
Fluid inlet T	40 °C	9 °C	9 °C	Lower inlet T for refrigerants favours heat absorption.
h theoretical	4370 W/(m^2·K)	947 W/(m^2·K)	1431 W/(m^2·K)	Water-Glycol has highest theoretical h.
h simulation	/	387,4 W/(m^2·K)	531,2 W/(m^2·K)	R290 outperforms R-134a in real-case simulation.
Fluid ΔT (between cold plate inlet and outlet)	1,26 °C	4,72 °C	2,40 °C	The higher the c_p the lower the ΔT between inlet and outlet.

Table 10.3: Final design comparison, three different cooling approaches.

10.2 Underlying detail

A final step in the reasoning process must be undertaken. Until now the analysis focused on comparing the three different cooling approaches based on the same mass flow rate circulating inside the system. The decision is justified by the fact that both the design and the heat transfer capability through convection, are highly affected by the $\dot{m}$ value.

However when comparing the two refrigerant cooling approaches, comparing them just based on the same $\dot{m}$ is equal to telling half of the story.
R290 refrigerant differentiates itself from R-134a also because of it's way higher c_p.

R290	R-134a	Comment
c_p = 1779,3 J/(Kg·K)	c_p = 907,5 J/(Kg·K)	Their ratio is almost 2:1, which affects the required mass flow rate ($\dot{m}$) in the system, as the same mass can absorb a greater amount of heat.

Table 10.4: R290 vs R-134a, c_p value comparison.

Based on the data reported in Table 10.4, refrigeration systems using R290 typically operate with approximately 30% reduced mass flow rate $\dot{m}$ (industry benchmark value) compared to those employing R-134a.
Considering the inlet conditions detailed in Tables 8.5 and 9.5, this reduction in $\dot{m}$ leads to the following implications.

Parameter	R290	R-134a	Comment
$\dot{m}$	0,098 Kg/s	0,14 Kg/s	$\dot{m}_{\mathrm{R290}} = 0,7 \cdot \dot{m}_{\mathrm{R134a}}$
ρ	11,33 Kg/m^3	16,16 Kg/m^3	ρ_{R290} lower than ρ_{R134a}
$\dot{V}$	8,66 L/s	8,65 L/s	Lowering the mass flow rate, the $\dot{V}$ between the two is comparable.

Table 10.5: Comparison between R290 and R-134a (with R290 $\dot{m}$ lowered of 30% w.r.t R-134a one).

The $\dot{V}$ between the two refrigerants at this point is basically the same. As a consequence the same cold plate design can be leveraged. To clear out every doubt, the design is the R-134a final design whose quotations are reported in Figure 8.13, 8.14, 8.15.
The performance characteristics of the system employing R-134a as the cooling fluid have been previously documented. The following results refer to the same cold plate configuration simulated with R-290.

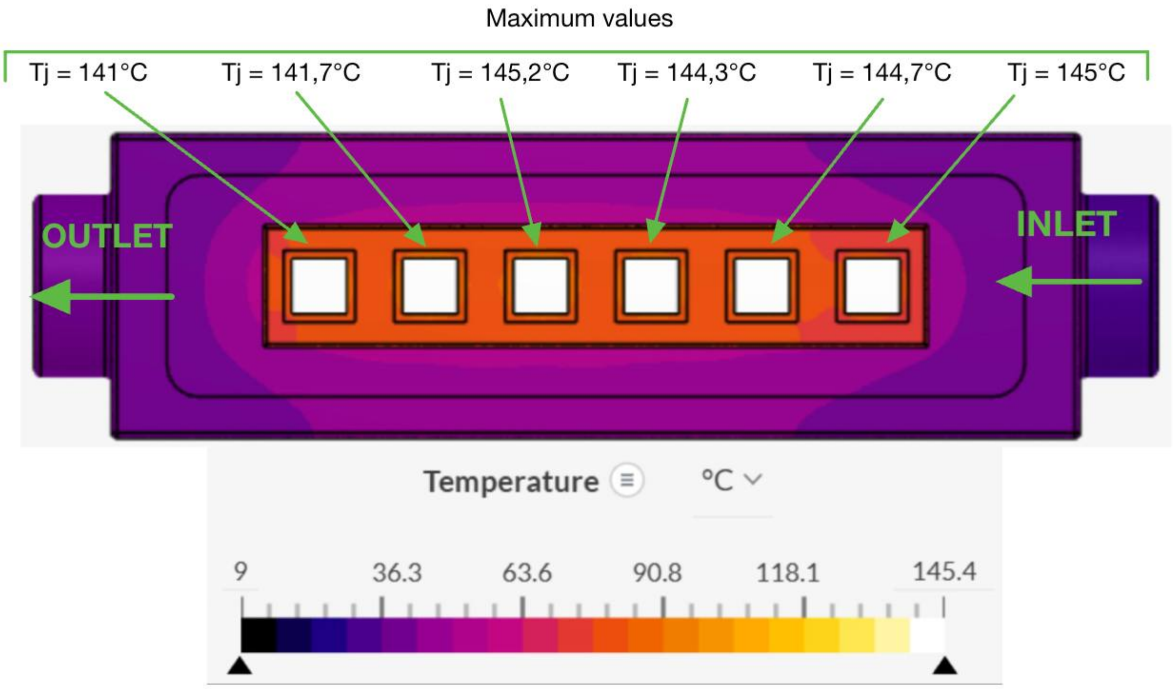

Figure 10.1: Mosfet T_j. R290 refrigerant cooled solution, R-134a cold plate design (Figure 8.13, 8.14, 8.15).

Inlet relative gauge pressure	Outlet relative gauge pressure	Final ΔP
1208,6 Pa	5,1 Pa	1203,5 Pa

Comparing the obtained values with the one exploiting R-134a refrigerant as refrigerant...

Parameter	R-134a	R290	Comment
Channel occupied volume	0,406L	0,406L	Same cold plate design.
Pressure drop ΔP	1723,3 Pa	1208,5 Pa	Much lower ΔP with R290 cooling.
Maximum T_j reached	156 °C	145,2 °C	Not only lower ΔP, but even better cooling performances.

Table 10.6: Comparison between R290 and R-134a (same cold plate design and $\dot{V}$).

Consequently, when comparing the performances of the different cooling options, R-290 emerges as the most promising refrigerant. Its main drawbacks, however, are the challenges associated with managing its flammability, potential leakage issues, and relatively high operating pressures.

R290 refrigerant ensures lower MOSFET and, as a consequence, cold plate temperatures.

Refrigerant	$T_{\text{fluid average}}$	$T_{\text{cold plate average (integral)}}$	$T_{\text{cold plate min}}$	$T_{\text{cold plate max}}$
R290	10,26°C	36,96°C	19,56°C	78,94°C

Table 10.7: R290 simulation with R-134a cold plate design parameter results .

When compared to R-134a cooling, it stands out how the R290 refrigerant better cooling performances ensure lower maximum and average cold plate temperatures.

Refrigerant	$T_{\text{fluid average}}$	$T_{\text{cold plate average (integral)}}$	$T_{\text{cold plate min}}$	$T_{\text{cold plate max}}$
R290	10,26°C	36,96°C	19,56°C	78,94°C
R-134a	11,36°C	47,38°C	27,29°C	90,8°C

Table 10.8: Same cold plate design, R290 vs R-134a refrigerant cooling.

A lower $T_{\text{cold plate max}}$ indicates a reduced presence of localized hot spots and a more uniform thermal interaction between the cold plate and the fluid.

As previous cases, the theory remarkably overestimated the convection heat coefficient h.

Refrigerant	Cold plate contact surface area	h theoretical	h simulation
R290	$\approx 0{,}043\ m^2$	$1519\ \frac{W}{m^2 \cdot K}$	$521{,}4\ \frac{W}{m^2 \cdot K}$

Table 10.9: R290 simulation with R-134a cold plate deisgn vs theoretical parameter comparison.

This is the reason why a way bigger cold plate surface area than expected is needed.

10.3 Final discussion

The thesis focused on the analysis, design, and comparison of different cooling technologies for power electronic devices employed in HVAC compressor applications. The objective was to assess alternative cooling strategies capable of meeting the required performances in terms of thermal dissipation, compactness, mechanical and electrical reliability.

The dissertation started with a general review of scientific literature, industrial benchmarks and state of the art solutions. Based on this preliminary step, three distinct approaches were selected and investigated:

- Water–glycol (50–50% in volume) cooling.
- R-134a refrigerant cooling.
- R290 (Propane) refrigerant cooling.

Under equivalent $\dot{m}$ boundary conditions, the different approaches were analysed.
The outcome of the study is a quantitative comparison in terms of pressure drop, MOSFET junction temperatures, occupied volume and cold plate to fluid interaction.

Water–Glycol cooling.

Water-Glycol fluid, because of its intrinsic properties, demonstrated an effective heat removal capability. The elevated heat transfer coefficient h, allows for a compact design of the cold plate. However this approach requires a dedicated secondary loop with pump, pipes and heat exchangers; causing the benefit of cold plate compactness to be totally outweighed by the additional components cost and occupied volume.
Leveraging a constant flow cross-sectional area design as in Figure 7.27, it was demonstrated to be possible to obtain excellent performances in terms of T_j with limited pressure drop.

Water–glycol cooling is a mature and well-established technology, remaining a feasible option in scenarios where a water–glycol circuit is already implemented for other purposes, or where space and cost constraints are not critical.

R-134a refrigerant cooling.

Leveraging the same refrigerant circulating within the HVAC system represents an innovative approach that, despite implementation challenges, offers several significant advantages. Chief among these is the creation of a fully coupled configuration, enabling the development of a fully integrated and all-in-one system for the customer.

Nevertheless, R-134a refrigerant exhibits lower heat transfer performance compared to the water-glycol mixture. This limitation raises the need of a larger heat exchange surface area to achieve comparable thermal performance. In addition, due to the significantly lower density of gaseous R-134a w.r.t water-glycol (that's in liquid form), a higher channel cross-sectional area is required under equivalent $\dot{m}$ conditions. As a result, a larger overall cold plate volume becomes necessary. This increase in volume, though, is offset by the absence of an external cooling circuit and its relative components.

Furthermore, the reduced heat transfer efficiency of R-134a results in a higher junction temperature T_j, slightly exceeding the design target of 150°C. Overall, the intrinsic properties of R-134a make this solution less effective in dissipating concentrated thermal loads, despite offering significant advantages in terms of system integration and simplification.

However, the considerably lower viscosity of R-134a contributes to a slightly reduced pressure drop ΔP. This reduction is particularly beneficial, as demonstrated in the sensitivity analysis, since ΔP directly influences the refrigeration cycle COP.

R290 refrigerant cooling.

Among the analysed solutions, the R-290 refrigerant emerged as the most promising solution. First of all its extremely low GWP (equal to 3) makes it suitable for the upcoming generation of sustainable HVAC solutions. It combines effective heat removal capability with a much lower pressure drop (compared to both water-glycol and R-134a) and improved temperature uniformity across the cold plate. Simulations verified that MOSFETs T_j stay within the target limit of 150°C.

Furthermore, because of its higher specific heat capacity equal to nearly twice that of R-134a, R-290 enables the HVAC system to operate at approximately 30% lower mass flow rate $\dot{m}$. This enables the reuse of the same cold plate design originally developed for R-134a, while achieving excellent T_j values and a significantly lower pressure drop compared to R-134a cooling.

However, these advantages are accompanied by significant safety and design challenges.
The flammability of R-290, together with its higher operating pressures, imposes strict mechanical and sealing constraints. Therefore, if not well addressed its implementation could be present some risks.

Future developments

Possible directions for future work include:

- Experimental validation of the numerical models presented in this thesis.
- Optimization of the cold plates geometries for further reduction of pressure drop.
- Investigation of alternative refrigerants with similar thermophysical properties that of R290, but reduced safety constraints.

Final remarks

In conclusion, the research confirmed that inverter refrigerant cooling can offer a significant advancement towards more compact, fully integrated HVAC systems.
Using its superior thermal properties while addressing safety concerns, R290 can pave the way for next-generation sustainable HVAC solutions.

Bibliography

[1] Manish Jindgar EDN community Nitin Gupta and Ravinder Dasila. URL: `https://www.edn.com/fundamentals-of-the-automotive-cabin-climate-control-system/` (cit. on p. 2).

[2] Gunt company. Thermodynamics of the refrigeration cycle. URL: `https://www.gunt.de/images/download/thermodynamics-of-refrigeration_english.pdf` (cit. on pp. 3–5).

[3] the free encyclopedia Wikipedia. URL: `https://en.wikipedia.org/wiki/Soft-switching_three-level_inverter?utm_source=chatgpt.com` (cit. on p. 6).

[4] S. M. Imrat Rahman, Ali Moghassemi, Ali Arsalan, Laxman Timilsina, Phani Kumar Chamarthi, Behnaz Papari, Gokhan Ozkan, and Christopher S. Edrington. “Emerging Trends and Challenges in Thermal Management of Power Electronic Converters: A State of the Art Review”. In: *IEEE Access* 12 (2024), pp. 50633–50672. DOI: `10.1109/ACCESS.2024.3385429` (cit. on pp. 7–9).

[5] Shaoyong Yang, Angus Bryant, Philip Mawby, Dawei Xiang, Li Ran, and Peter Tavner. “An Industry-Based Survey of Reliability in Power Electronic Converters”. In: *IEEE Transactions on Industry Applications* 47.3 (2011), pp. 1441–1451. DOI: `10.1109/TIA.2011.2124436` (cit. on p. 8).

[6] Radian Company. URL: `https://radianheatsinks.com/heatsink/` (cit. on pp. 11, 12).

[7] David J. Perreault John G. Kassakian. *Principle of Power Electronics*. Cambridge University Press, 2022. URL: `https://circuits.mit.edu/_static/F23/6s060/KPVS_ThermalModeling.pdf` (cit. on p. 13).

[8] RS components. URL: `https://uk.rs-online.com/web/content/discovery/ideas-and-advice/thermal-interface-materials-guide` (cit. on pp. 13–15).

[9] T Globlal Technology. URL: `https://www.tglobalcorp.com/faqs/thermal-interface-materials/thermal-paste-thermal-conductive-pad-difference/#:~:text=Thermal%20grease%20offers%20better%20thermal,larger%20gaps%20or%20uneven%20surfaces.` (cit. on p. 13).

[10] Aismalibar. URL: `https://www.aismalibar.com/product_family/thermal-grease/` (cit. on p. 14).

[11] Alpay Asma Haydar Kepekci. “Comparative Analysis Of Heat Sink Performance Using Different Materials”. In: *American Journal of Engineering Research (AJER)* (2020). URL: `https://ajer.org/papers/Vol-9-issue-4/W0904204210.pdf` (cit. on pp. 15, 17).

[12] Mohd Moinuddin Ansari Abdul Raheem Junaidi Raghavendra Rao. “Thermal Analysis of Splayed Pin Fin Heat Sink”. In: *International Journal of Modern Communication Technologies Research (IJMCTR)* (2014). URL: `https://www.erpublication.org/ijmctr/published_paper/IJMCTR021417.pdf` (cit. on p. 18).

[13] Advanced thermal solutions ATS. URL: `https://www.qats.com/Products/Liquid-Cooling/Cold-Plates` (cit. on p. 20).

[14] ABB company. URL: `https://search.abb.com/library/Download.aspx?DocumentID=3AUA0000115037&LanguageCode=en&DocumentPartId=&Action=Launch&_gl=1*yp6qo3*_gcl_au*ODgwOTk4NzU3LjE3NDQyODkxOTg.*_ga*MjA1OTgwNDI3OS4xNzQ0Mjg5MTk3*_ga_46ZFBRSZNM*MTc0NTQ5MzM4NC4xNC4wLjE3NDU0OTMzODkuNTUuMC4w` (cit. on pp. 24, 25).

[15] Zinsight tech company. URL: `http://www.zinsight-tech.com/hs3050` (cit. on pp. 30–32).

[16] Cascadia Motion company. URL: `https://www.cascadiamotion.com/inverters---snapshot.html` (cit. on pp. 30–32).

[17] Danfoss company. URL: `https://www.danfoss.com/en/products/dps/electric-converters-motors-and-systems/electric-converters/high-voltage-electric-inverters/#tab-documents` (cit. on pp. 30–32).

[18] John Reimers, Lea Dorn-Gomba, Christopher Mak, and Ali Emadi. "Automotive Traction Inverters: Current Status and Future Trends". In: *IEEE Transactions on Vehicular Technology* 68.4 (2019), pp. 3337–3350. DOI: `10.1109/TVT.2019.2897899` (cit. on pp. 35, 36).

[19] Wataru Saito. "A Future Outlook of Power Devices From the Viewpoint of Power Electronics Trends". In: *IEEE Transactions on Electron Devices* 71.3 (2024), pp. 1356–1364. DOI: `10.1109/TED.2023.3332611` (cit. on p. 36).

[20] J. Y. Tsao et al. URL: `https://advanced.onlinelibrary.wiley.com/doi/10.1002/aelm.201600501` (cit. on pp. 37, 38).

[21] Analogue Design Journal. URL: `https://www.ti.com/lit/an/slyt801/slyt801.pdf?ts=1756888423271ref` (cit. on p. 39).

[22] Turbocor Broshure Danfoss. URL: `https://assets.danfoss.com/documents/latest/97807/AD304757423527en-000103.pdf` (cit. on p. 41).

[23] Wolfspeed website. URL: `https://www.wolfspeed.com/products/power/sic-mosfets/1200v-silicon-carbide-mosfets/c3m0021120u2/` (cit. on p. 47).

[24] RichardSon RFPD. URL: `https://www.richardsonrfpd.com/ep-technical-articles/wolfspeed-top-side-cooled-sic-mosfet/#:~:text=Improved%20thermal%20management%2C%20design%20flexibility%20and%20simplified%20assembly,Wolfspeed%E2%80%99s%20portfolio%20of%20silicon%20carbide%20top-side%20cooled%20MOSFETs.` (cit. on pp. 47, 48).

[25] Wolfspeed website. URL: `https://www.wolfspeed.com/knowledge-center/article/designing-with-top-side-cooled-tsc-silicon-carbide-power-devices/` (cit. on p. 47).

[26] Richardson RFPD. URL: `https://www.youtube.com/watch?v=aPPUsDxsNJ4` (cit. on p. 48).

[27] Hong Kong Polytechnic University. URL: `https://www.polyu.edu.hk/edc/tdg/userfiles/file/490Q_ABCT/ICBPT_Cht6Heat.pdf` (cit. on p. 49).

[28] Indira Gandhi National Open University(IGNOU). *GOVERNING EQUATIONS OF HEAT Heat Conduction CONDUCTION*. IGNOU. URL: `https://egyankosh.ac.in/bitstream/123456789/31667/1/Unit-4.pdf` (cit. on pp. 49, 50).

[29] Wolfspeed. URL: `https://www.wolfspeed.com/products/power/sic-mosfets/1200v-silicon-carbide-mosfets/c3m0021120u2/` (cit. on pp. 52, 55).

[30] Parker Hannifin Corporation. URL: `https://www.parker.com/content/dam/Parker-com/Literature/Assembly---Protection-Solutions-Division/Technical-Datasheets-(TDS)/Datasheet---CoolThermSC-1600_DS4450.pdf` (cit. on pp. 53–55).

[31] ceramic thermal pads Innovacera. URL: `https://www.innovacera.com/admin/uploads/2024/01/Aluminum-Nitride-Ceramic-Thermal-Pads.pdf` (cit. on pp. 53–55).

[32] engineering materials Matweb. URL: `https://www.matweb.com/search/datasheet.aspx?matguid=b8d536e0b9b54bd7b69e4124d8f1d20a` (cit. on pp. 53–55).

[33] The data are store in internal Garrett Motion libraries no links are available (cit. on pp. 57, 93).

[34] University of Waterloo (Ontario). *Lecture Notes - Chapter 6*. n.d. URL: `http://www.mhtl.uwaterloo.ca/courses/ece309_mechatronics/lectures/pdffiles/chapter6.pdf` (cit. on pp. 57, 94).

[35] Simscale site. URL: `https://www.simscale.com/docs/simulation-setup/advanced-concepts/thermal-resistance-networks/` (cit. on p. 62).

[36] Wikipedia.org. URL: `https://en.wikipedia.org/wiki/Compressor_map` (cit. on p. 87).

[37] Tlk energy company. URL: `https://tlk-energy.de/en/phase-diagrams/pressure-enthalpy` (cit. on pp. 90, 125).

[38] GT-SUITE software. URL: `https://www.gtisoft.com/gt-suite/` (cit. on pp. 93, 117, 126).

[39] OBT Custom rubber parts. URL: `https://rubberproducer.com/2025/04/23/comparation-of-next-generation-refrigerants-for-new-energy-vehicle-ac-systems-and-rubber-seal-requirements/` (cit. on pp. 123, 124).